

Growth, timing, & trajectory of vortices behind a rotating plate

Présentée le 19 juillet 2022

Faculté des sciences et techniques de l'ingénieur
Laboratoire de diagnostic des écoulements instationnaires
Programme doctoral en mécanique

pour l'obtention du grade de Docteur ès Sciences

par

Diego FRANCESCANGELI

Acceptée sur proposition du jury

Prof. J. M. Kolinski, président du jury
Prof. K. A. J. Mulleners, directrice de thèse
Prof. D. E. Rival, rapporteur
Prof. T. Leweke, rapporteur
Dr M. Farhat, rapporteur

Acknowledgements

I would like to use this page to thank all the people that I met during this long path called Ph.D. First of all, I would like to thank my supervisor Karen Mulleners who gave me the opportunity to join this lab and do this incredible experience. We shared good and tough moments and I really grew up a lot under your guide. "Don't be scared of problems or frustrated from the lack of results, just enjoy the process of finding a solution". This is probably the best teaching you gave me and I will always bring with me.

I also want to reserve some words to the members of the jury that came here in Lausanne to listen and evaluate this work, providing a very constructive feedback that helped me to improve the quality of the manuscript.

I want to thank all the people from the UNFoLD lab. Every time I had a tough moment, simply knocking the door of your offices and speaking with you was a breath of fresh air. You are more than simple colleagues for me and I could not imagine spending this time in the lab without you. Nice UNFoLD people nice.

A big thanks goes to the old friends, to those that are in Italy and those living around the world. I am looking forwards to see you all soon. And I cannot forget to mention the new friends that I have made during these last four years, with a special thank to Lorenzo. I met you at the very beginning of the Ph.D, when we both had to attend the safety training. From that moment, we shared all the joys and frustrations of doing a Ph.D abroad. They say that the safety training is not useful, but after all it's where we met and we became Friends, with the capital letter.

And thanks to all my family, in particular to my brother Filippo, my mom Maria Grazia and my dad Oriano. If I arrived here is mainly thanks to your sacrifices, advices and teachings. I know that I can call you at every hour of the day, and night if necessary. You are kilometres away from here, but I feel like you are always close to me.

And last but not least, I really want to reserve these last words to Elisabetta. I met you when I was about to submit my thesis, one of the toughest period I've ever experienced. You sweetened those days in a way that you could not imagine, reminding me that I was doing a cool job and I should have been proud of that. A big kiss to you.

Lausanne, June 23, 2022

Abstract

The presence of aerodynamic vortices is widespread in nature. They can be found at small scales near the wing tip of flying insects or at bigger scale in the form of hurricanes, cyclones or even galaxies. They are identified as coherent regions of high vorticity where the flow is locally dominated by rotation over strain. A better comprehension of vortex dynamics has a great potential to increase aerodynamic performances of moving vehicles, such as drones or autonomous underwater vehicles. The vortical structures that form as a result of the interaction between an object and a flow stream are not all the same. An accelerated flat plate, a pitching airfoil or a jet flow ejected from a nozzle give rise to the formation of a primary vortex, followed by the shedding of smaller secondary vortices. The difference between primary and secondary vortices led us to experimentally study the growth, timing and trajectory of vortices generated from a rectangular flat plate that is rotated around its centre location in a quiescent fluid. We systematically vary the rotational speed of the plate to get a chord based Reynolds number Re that ranges from 800 to 12 000. We identify the critical Reynolds number for the occurrence of secondary vortices to be at 2500.

The timing of the formation of the primary vortex is Re independent but is affected by the plate's dimensions. The circulation of the primary vortex increases with the dimensionless convective time, which is the angular position α of the plate, until the angular position $\alpha_0 = 30^\circ$ is reached. Increasing the thickness and decreasing the chord lead to a longer growth of the primary vortex. As a consequence, the primary vortex reaches a higher dimensionless limit strength. We define a new dimensionless time T^* based on the thickness of the plate to scale the age of the primary vortex. The primary vortex stops growing when $T^* \approx 10$, regardless of the dimensions of the plate. We consider this value to be the vortex formation number \hat{T} of the primary vortex generated from a rectangular flat plate that rotates with a speed resulting in a Reynolds number in the range from 800 to 12 000. When $\alpha > \alpha_0$, the circulation released in the flow is entrained into the first secondary vortex for $Re > 2500$. The circulation of all secondary vortices is approximately 4 to 5 times smaller than the circulation of the primary vortex. The time interval between the release of successive vortices is not constant during the rotation but increases the more secondary vortices have been previously released. We present a modified version of the Kaden spiral that accurately predicts the shear layer evolution and the trajectory of primary and secondary vortices during the entire rotation of the plate. We model the timing dynamics of secondary vortices with a

power law equation that depends on two distinct parameter: χ and α_0 . The parameter χ indicates the relative increase in α between the convective timing of successive secondary vortices. The parameter α_0 indicates the angular position at which the primary vortex stops growing and pinches-off from the plate. We also observe that the total circulation released in the flow is proportional to $\alpha^{1/3}$, as predicted by the inviscid theory. The combination of the power law equation with the total circulation computed from inviscid theory predict the strength of primary and secondary vortices, based purely on the plate's geometry and kinematics. The strength prediction is confirmed by experimental measurements.

In this thesis we provided a valuable insight into the growth, timing and trajectory of primary and secondary vortices generated by a rotating flat plate. Future work should be directed towards more complex object geometries and kinematics, to confirm the validity of the modified Kaden spiral and explore the influence on the formation number.

Key words: Shear layer roll-up, primary vortex, vortex pinch-off, secondary vortices, vortex shedding, PIV

Sommario

La presenza dei vortici è ampiamente diffusa in natura. Si possono trovare piccoli vortici nelle estremità delle ali di insetti oppure si possono osservare vortici giganteschi nella forma di uragani o cicloni. Persino le enormi galassie dello spazio profondo possono essere viste come degli enormi vortici. Possiamo definire i vortici come regioni in cui la vorticità è estramente elevata e dove il flusso è prevalentemente rotatorio. Una migliore comprensione della dinamica dei vortici porterebbe a miglioramenti aerodinamici di veicoli come ad esempio droni o sottomarini a guida automatica. I vortici che si formano come risultato dell'interazione tra un oggetto e la corrente circostante non sono tutti uguali. Una piastra che accelera, un profilo alare che ruota o un getto di fluido espulso da un ugello formano un vortice primario che è seguito dal rilascio di vortici secondari più piccoli. La differenza tra vortici primari e secondari ci ha motivato a studiare sperimentalmente la crescita, le tempistiche e la traiettoria dei vortici generati da una piastra piatta rettangolare che viene ruotata intorno alla sua posizione centrale in un fluido quiescente. Abbiamo sistematicamente variato la velocità di rotazione della piastra per ottenere un numero di Reynolds Re che varia da 800 a 12 000. Abbiamo identificato il numero di Reynolds critico per la comparsa di vortici secondari a 2500. Il tempo di formazione del vortice primario è indipendente da Re ma è influenzato dalle dimensioni della piastra. La circuitazione del vortice primario aumenta con il tempo convettivo adimensionale, che corrisponde alla posizione angolare α della piastra, fino a quando la piastra non raggiunge la posizione angolare $\alpha_0 = 30^\circ$. Aumentando lo spessore e diminuendo la corda si ottiene una crescita più lunga del vortice primario. Di conseguenza, il vortice primario raggiunge una forza limite adimensionale più alta. Definiamo un nuovo tempo adimensionale T^* , basato sullo spessore della piastra, per scalare il tempo di formazione del vortice primario. Il vortice primario smette di crescere quando $T^* \approx 10$, indipendentemente dalle dimensioni della piastra. Consideriamo questo valore come il numero di formazione del vortice \hat{T} del vortice primario generato da una piastra piatta rettangolare che ruota con una velocità risultante in un numero di Reynolds che varia da 800 a 12 000. Quando $\alpha > \alpha_0$, la circuitazione rilasciata nel flusso viene trascinata nel primo vortice secondario per $Re > 2500$. La circuitazione di tutti i vortici secondari è approssimativamente da 4 a 5 volte più piccola della circuitazione del vortice primario. L'intervallo di tempo tra il rilascio di successivi vortici secondari non è costante durante la rotazione ma aumenta quanto più vortici secondari sono stati precedentemente rilasciati.

Presentiamo una versione modificata della spirale di Kaden che predice accuratamente l'evoluzione dello strato di taglio e la traiettoria dei vortici primari e secondari durante l'intera rotazione della piastra. Modelliamo la dinamica temporale dei vortici secondari con una legge di potenza che dipende da due parametri distinti: χ e α_0 . Il parametro χ indica l'aumento relativo di α tra i tempi di rilascio di successivi vortici secondari. Il parametro α_0 indica la posizione angolare in cui il vortice primario smette di crescere e si stacca dalla piastra. Osserviamo anche che la circuitazione totale rilasciata nel flusso è proporzionale a $\alpha^{1/3}$, come previsto dalla teoria inviscida. La combinazione della legge di potenza con la circuitazione totale calcolata dalla teoria inviscida predice la forza dei vortici primari e secondari, basandosi puramente sulla geometria e la cinematica della piastra. La previsione della forza dei vortici è confermata da misure sperimentali. In questa tesi abbiamo fornito un'importante comprensione della crescita, delle tempistiche e della traiettoria dei vortici primari e secondari generati da una piastra piatta in rotazione. Il lavoro futuro sarà diretto verso geometrie e cinematiche di oggetti più complessi, per confermare la validità della spirale di Kaden modificata ed esplorare l'influenza sul numero di formazione.

Parole chiave: Shear layer roll-up, primary vortex, vortex pinch-off, secondary vortices, vortex shedding, PIV

Contents

Acknowledgements

Abstract	i
----------	---

Sommario	iii
----------	-----

Contents	v
----------	---

List of Figures	vii
-----------------	-----

1 Introduction	1
----------------	---

1.1 Welcome to the world of vortex dynamics	1
1.2 Motivation of the present research	3
1.3 Thesis outline	4

2 Theoretical background	6
--------------------------	---

2.1 The roll-up of the shear layer	6
2.1.1 Vortex sheets	7
2.1.2 Self-induced velocity of vortex sheets	9
2.1.3 Mass and momentum entrainment in shear layers	10
2.2 Self-similar solutions of the Birkhoff-Rott equation	12
2.2.1 Logarithmic spirals	12
2.2.2 Semi-infinite vortex sheet	14
2.2.3 Extension of Kaden's spiral to a finite wing	18
2.2.4 Accelerated flow past a wedge	18
2.2.5 Zero wedge angle: flow past a flat plate	20
2.3 Growth of a primary coherent structure	23
2.3.1 Start-up vortex issuing from a flat plate	23
2.3.2 Vortex ring generated from a piston-cylinder apparatus	24
2.3.3 Leading edge vortex from a pitching wing	27
2.4 Limit process of the vortex formation	29
2.4.1 Mechanism of separation	29
2.4.2 Vortex formation number	31
2.5 Flow field after primary vortex separation	34
2.5.1 Kelvin-Helmholtz instability	34

2.5.2	Other examples of instability	37
2.5.3	Occurrence of secondary vortices	38
2.6	Three dimensional effects	40
2.7	Summary and objectives of the research	42
3	Experimental measurements and analysis	45
3.1	The rotation mechanism	45
3.1.1	Plate geometry and kinematics	47
3.1.2	Scaling parameters	48
3.2	Particle image velocimetry	49
3.2.1	Time-resolved measurements	51
3.2.2	Phase-averaged measurements	52
3.3	Velocity and vorticity fields from PIV data	52
3.3.1	Flow field evolution in time	53
3.3.2	Flow field with the plate at 90°	56
3.4	Identification of coherent structures	57
3.4.1	Eulerian methods	57
3.4.2	Lagrangian data analysis	60
3.5	Computation of the vortex circulation	61
3.6	Computation of radial velocity and vorticity distribution	64
3.6.1	Description of the fitting algorithm	65
3.6.2	Size and velocity profile for the primary vortex	66
3.6.3	Size and velocity profile for secondary vortices	69
3.7	Influence of the flow field resolution and three-dimensional effects . . .	71
3.8	Summary and conclusions	73
4	Discrete shedding of secondary vortices	75
4.1	Literature studies about the topic	75
4.2	Experimental methods	78
4.3	Results	80
4.3.1	Modelling the shear layer roll-up	80
4.3.2	Validation of the model	83
4.3.3	Timing of the secondary vortex shedding	85
4.4	Summary and conclusion	90
4.5	Appendices	91
4.5.1	Derivation of the modified Kaden spiral	91
4.5.2	Sensitivity analysis of the location and size of the average tip swirling strength probing region	92
5	Formation and scaling of primary and secondary vortices	95
5.1	Literature studies about the topic	95
5.2	Experimental methods	98
5.3	Results	100

5.3.1	Primary vortex growth and separation	101
5.3.2	Analogy with the piston-cylinder apparatus	106
5.3.3	Primary vortex formation number	107
5.3.4	Strength of secondary vortices	111
5.4	Summary and conclusions	113
6	Summary and conclusions	115
6.1	Future work and potential applications	117
	Bibliography	119
	Curriculum vitae	133

List of Figures

1.1	Example of vortices	2
2.1	Sketch of vortex sheet	6
2.2	Local and fa-field components on the boundary layer strength	8
2.3	Snapshot of Prandtl's flow visualization	12
2.4	Logarithmic spiral	14
2.5	Sketch of Kaden's problem	15
2.6	Sketch of flow past a wedge	19
2.7	Numerical and experimental spiral comparison	21
2.8	Sketch of vortex ring growth	25
2.9	Sketch of saddle points for LEV growth	28
2.10	Examples of Kelvin-Helmholtz instability	36
2.11	Crown instability from two airplane contrails	38
2.12	Secondary vortices from a rotating plate	41
3.1	Rotation mechanism	46
3.2	Kinematics of the plate	47
3.3	Rendering of PIV set-up	50
3.4	Velocity and vorticity fields in time	54
3.5	Single snapshot vs phase-averaged flow field	57
3.6	Velocity and vorticity fields at 90°	58
3.7	Identification of vortex contours	59
3.8	Sketch of FTLE ridges around a rotating plate	61
3.9	Comparison between Γ_2 and λ_{ci} contours	63
3.10	Circulation of secondary vortices shed at $Re = 8380$	64
3.11	Sketch and results of the algorithm used to compute the vorticity distribution	66
3.12	Circulation of the primary vortex as a function of the distance from the centre	68
3.13	Tangential velocity distribution and core radius in time	69
3.14	Vorticity and velocity distribution of secondary vortices	70
3.15	Circulation of secondary vortices computed from Lamb-Oseen	71
3.16	Influence of the field resolution into the vorticity distribution	73

4.1	Experimental set-up	79
4.2	Continuous shear layer	81
4.3	Spiral of different flow regimes	81
4.4	Kaden's constant as a function of the convective time	82
4.5	Comparison of negative FTLE	83
4.6	Beta as a function of convective time	84
4.7	Flow evolution in the discrete shedding regime	85
4.8	Swirling strength criterion at high Re	86
4.9	Swirling strength criterion at lower Re	87
4.10	Timing of secondary vortices	88
4.11	Power law coefficient as a function of Re	89
4.12	Coordinate system of the plate's reference of frame	91
4.13	Sensitivity analysis of the box location from the plate's tip	94
5.1	Example of primary and secondary vortices	97
5.2	Temporal evolution of vorticity and swirling strength in the discrete shedding regime	100
5.3	Saddle point corresponding to the primary vortex separation	102
5.4	Dimensional and dimensionless circulation as a function of the plate's angle of rotation	103
5.5	Limit strength and convective time of the primary vortex in the discrete shedding regime	104
5.6	Limit strength of the primary vortex at lower Re	106
5.7	Dimensionless velocity of the primary vortex for various Re	108
5.8	Primary vortex circulation as a function of \hat{T}	109
5.9	Total dimensionless circulation from longer and thicker plates	110
5.10	Strength prediction of secondary vortices	111
6.1	Overlap of the modified Kaden's spiral in the wake of a translating cone	117

Chapter 1

Introduction

1.1 Welcome to the world of vortex dynamics

The idea of a vortex is generally associated with a mass of fluid that rotates around an axis. The most intuitive example of a vortex is probably the whirlpool that forms when removing the cap from a bathtub filled with water. The same phenomenon can also be observed in tight sea channels when eddies interact with the surrounding land (Figure 1.1a) or when the river flow encounters the obstacle of a downstream dam. We can find many other examples of vortices at different scales. At small scales, the formation of vortices on the leading edge of a wing can explain how insects (Figure 1.1b), such as dragonflies or bumblebees, support their weight during hovering [127, 12]. A nectar feeding bat exploits leading-edge vortices to increase the lift during forward flight [99]. Aerodynamic and aeronautic engineering applications often require to study the formation of vortices at various scales. For instance, the study of wingtip vortices detaching from the wings of airplanes (Figure 1.1c) is fundamental to minimize the induced drag and reduce wake turbulence. At bigger scales, hurricanes and cyclones (Figure 1.1d) form in particular regions of the Earth devastating everything they meet on their path. This happened when Hurricane Dolly in 2008 made landfall in southern Texas, when the internal vortex dynamics strongly contributed to a rapid intensification of the hurricane strength [64]. We can also observe vortical structures outside the Earth. The Great Red Spot on Jupiter is an example of an extraterrestrial massive vortex that is bigger than the entire Earth (Figure 1.1e). Similar to its companion, Saturn exhibits every Saturn year, about 28 Earth years, a short-lived massive vortex called Great White Spot. Spiral galaxies, like the *NGC4622* that is located 111 million light-years away in the constellation Centaurus, looks like an axisymmetric circular vortex that rotates around its bright centre (Figure 1.1f). The peculiar thing among the previous examples is that the vortices have all a similar shape, which suggests that vortex dynamics can be applied in many different fields of research.

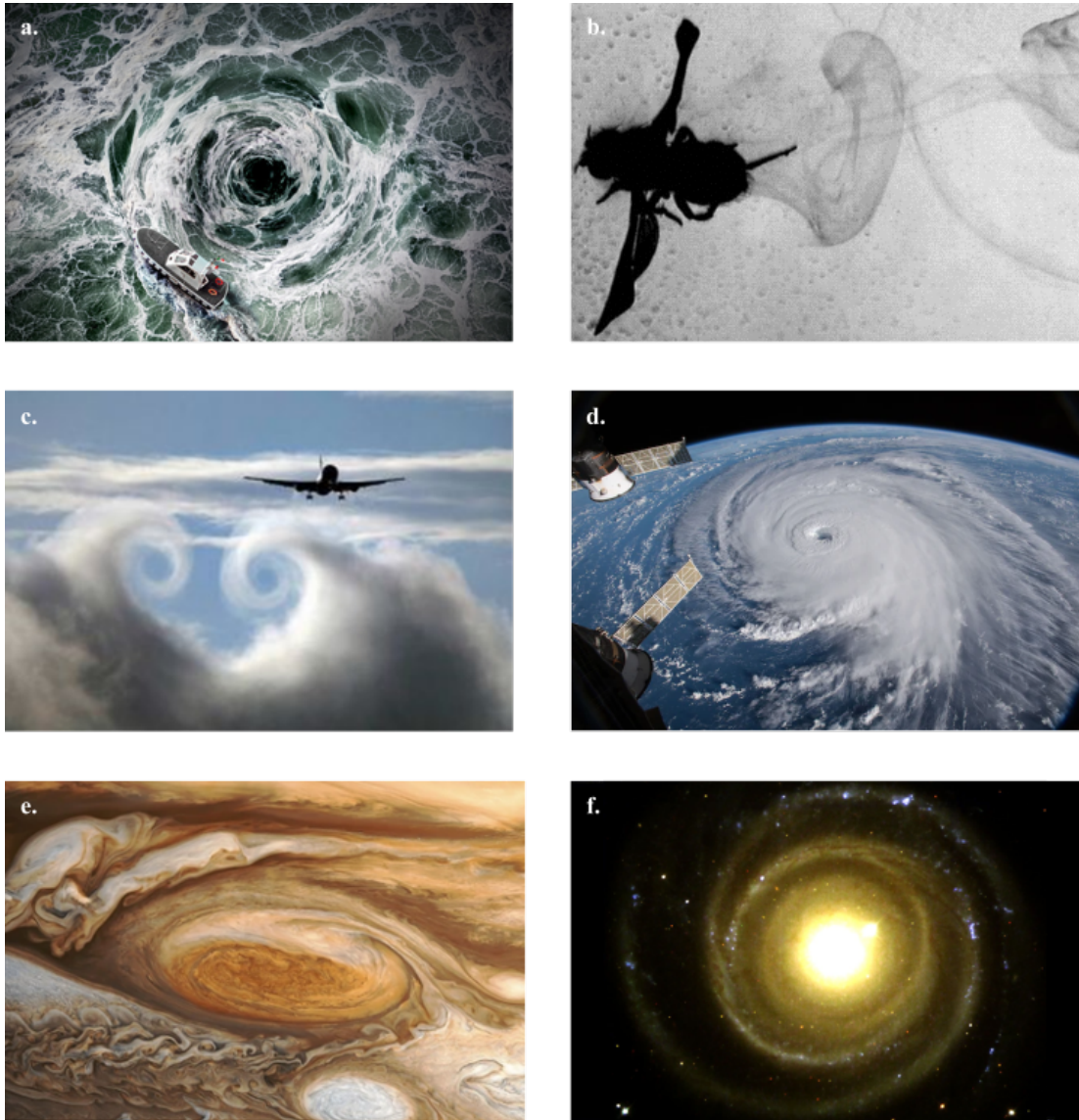


Figure 1.1: (a) Picture of a boat approaching a whirlpool in the Naruto Strait, a channel in Japan between Tokushima and Awaji Islands. (b) Vortices shed from a flying fruit fly. The flow visualization is realised with schlieren imaging by dispersing glycerol vapour in the air [18]. Credit: Irmgard Bischofberger, MIT, USA. (c) Wing tip vortices observed in the wake of an airplane. (d) Slow and lumbering Hurricane Florence churns across the Atlantic Ocean on the morning of September 12, 2018. Credit: courtesy of NASA. (e) A view of Jupiter and the Great Red Spot. The white oval storm directly below the Great Red Spot has the approximate diameter of Earth. Credit: courtesy of NASA. (f) Photograph of galaxy *NGC4622* taken in May 2001 with Hubble's Wide Field Planetary Camera 2. This galaxy is a rare example of a spiral galaxy with arms pointing in opposite directions. Credit: courtesy of NASA.

The first mathematical formulation of vortices dates from 1858, when Helmholtz [63] studied vortex filaments in inviscid flows and showed that the circulation of the vortex is preserved in absence of non-conservative forces. The study of vortex dynamics had not been considered of interest for many years, regardless of the potential application in many fields. Lamb [82] claimed that the motion of a solid in a liquid endowed with vorticity is a problem of considerable interest, but unfortunately not very tractable. The first big step forward in vortex dynamics and flow investigation was made by Prandtl [108], who designed and utilized flow visualization techniques in a water tunnel to study aspects of unsteady separated flows behind wings and other objects. In his experiments, Prandtl manually rotated a blade wheel to create flow and added seeding particles to visualize the flow field. At that time, no quantitative data about flow velocity or vorticity could be achieved. The definitive step was made in the last 30 years thanks to the scientific and technical progress achieved in optics, lasers, electronics, video and computer techniques. The combination of these many technical advances brought to develop techniques, such as Particle Image velocimetry [114], for qualitative flow visualization to such a stage that they can be employed for quantitative measurement of complex instantaneous velocity fields.

1.2 Motivation of the present research

The investigation into the field of vortex dynamics is attractive for several aspects. The formation of vortices in the wake of wings or airfoils is strongly correlated with the thrust and lift produced. The lift coefficient on a constantly pitching airfoil keeps increasing above the static stall angle due to the formation of a leading edge vortex (LEV) [100]. Milano and Gharib [93] identified a peak in the lift coefficient when the LEV reaches its maximum strength. When this vortex is no longer in the close proximity of the airfoil, the lift coefficient suddenly drops. This phenomenon is referred to as dynamic stall and is observed in helicopter rotor blades or in vertical axis wind turbines (VAWT). These wind turbines have the main rotor shaft transverse to the wind and they do not need to be pointed into the wind direction. They are also smaller and easier to implement and maintain than the more famous and used horizontal axis wind turbines. However, VAWTs are fatigue-prone due the wide range of experienced forces during each cycle and dynamic stall is a strong contributor to the fatigue. In this regard, the study of forming vortices is the key aspect to develop a control system that mitigates dynamic stall, with the aiming of reducing fatigue issues and making VAWTs more attractive for wind energy applications.

The prolonged attachment of a LEV on the suction side of a flapping wing results in a higher lift performance with respect to the steady fixed wing alternative [36]. The flapping motion is particularly effective at small scales and is used by insects to produce high lift to sustain their weight during flight. Bio-inspired applications try to mimic

and optimize the insect flapping motion with the aim of implementing it into the flight of autonomous small scales vehicles or micro air vehicles (MAVs). The study of growth and separation of the LEV from the flapping wing reveals how the wing kinematics influence LEV properties. For instance, Gehrke and Mulleners [48] delayed the growth of a leading-edge vortex generated from a flapping wing by adapting the pitch angle kinematics. The prolonged growth of the LEV reduces the required aerodynamic power and increases the hovering efficiency. In this framework, the relationship between LEV properties and wing kinematics is crucial to control the wing aerodynamic performance and develop more efficient small-scale vehicles.

The vortex formation is also the mechanism with which sea animals such as squids, scallops or jellyfishes propel themselves efficiently. These animals generate a jet flow that rolls-up into a vortex ring [89, 24] and the achieved thrust is strongly correlated with the strength of the vortex ring. For instance, the normalised time-averaged thrust per jet pulse is maximum when the vortex ring reaches the maximum strength and pinches-off from the trailing jet [79, 77]. The study of vortex ring can aid the development of alternative marine propulsion system.

The strong influence of the vortex formation in engineering and bio-inspired applications motivate us for an in-depth study of the vortex formation from a simple but yet fundamental flow configuration. We decide to study the growth, trajectory and timing of vortices shed in the wake of a pure rotating plate. The growth, timing and trajectory of vortices define the entire vortex formation. The full characterization of how a vortex grows, moves and separates from an aerodynamic object has a wide spectrum of potential applications. We choose to focus on the rotation motion because is a basic but yet fundamental two-dimensional motion. Every kind of two-dimensional motions can be decomposed into a pure rotation and translation. There is an extensive literature that discusses on vortex formation behind translating objects [26, 38, 120, 105]. The single rotation is less investigated because the rotation is often studied as a pitching motion, which consists of multiple back and forth rotations [102, 14, 145]. Here, the vortex formation from a single rotation cycle is investigated in detail, with the future perspective of generalizing these results in more complicated kinematics. Finally, the choice of a flat plate as the tested object is because the unsteady flows generated around wings and fins of flying and aquatic animals are often modelled as flows past a flat plate [14, 55, 12, 76].

1.3 Thesis outline

The work presented in this thesis is divided into six chapters. Each chapter has a first section that briefly introduces the topic, a core part in which the topic is extensively analysed and concluding remarks that summarize the main take home messages of the

chapter. The present chapter is the introduction chapter and gives a general overview about vortex dynamics. Particular attention is given to the influence that the formation of vortices has on engineering and bio-inspired applications. The relationship between force, thrust and lift with vortex formation gives us the motivation to study the growth, timing and trajectories of vortices behind a rotating plate.

Chapter 2 presents the theoretical background that is the framework inside which the work of this thesis is placed. We start from the mathematical and physical modelling of the shear layer roll-up that leads to the formation of a vortex. Experimental and numerical studies about the subsequent vortex growth and separation are addressed and discussed. Finally, we review the occurrence of secondary structures that follow the first generated vortex, we discuss the stability of the shear layer, and comment on the effect of wake three-dimensionality. The extensive literature survey allows us to focus on those aspects that are still unclear and to highlight the questions that are not yet solved. These unanswered questions lead us to formulate the objectives of the present thesis that are presented at the end of **chapter 2**.

Chapter 3 describes the rotation mechanism and the optical experimental set-up used to record particle image velocimetry (PIV) images of a rotating plate in quiescent water. These images represent the experimental database of the thesis and particular attention is given to the processing parameters used to extract qualitative and quantitative information from PIV images. We describe the evolution of the flow topology as the plate rotates in water and we discuss the methods and the techniques adopted to compute vortex quantities, such as vorticity and circulation. The methods and techniques described in this chapter are the starting point to reach the results showed in the following chapters.

Chapter 4 and **chapter 5** discuss the main results of this research. **Chapter 4** focuses on the trajectory and timing of vortices generated by a rotating rectangular plate in a quiescent fluid. We develop and validate a model that predicts the shear layer roll-up and the trajectory followed by all the generated vortices. We also develop a fast and easy to implement technique to compute the timing at which vortices are released from the tip of the plate. We find that the timing is not constant and decreases with increasing rotational speed of the plate. The results obtained in **chapter 4** are used in **chapter 5** to analyse the vortex growth and compute the strength of the generated vortices. We show an analogy between the primary vortex observed here and the vortex ring generated from a piston-cylinder apparatus, which leads us to define a vortex formation time above which the primary vortex does not grow anymore.

Finally, **chapter 6** summarizes the most important results of the thesis and discusses potential directions for towards future work. A final paragraph that shows the potential applications of this research is also included.

Chapter 2

Theoretical background

2.1 The roll-up of the shear layer

Experimental techniques that quantitatively measure flow fields allow to get a closer look at the formation of vortices. Although the idea of what a vortex is may seem clear, a universally accepted definition of a vortex is still lacking [68]. As suggested by Haller et al. [61], vortices are generally considered to be coherent structures of high vorticity. Among the huge variety of vortex dominated flows, we focus here on the coherent structures that are generated when an object interacts with a flow stream. The formation of such vortices often begin with a thin layer of fluid, referred as shear layer, that emerges at the edge of the body as a result of a relative motion between the fluid and the body [37, 98, 39, 67]. The shear layer is detected in proximity of plate tips, leading and trailing edges of airfoils or at the boundary of a trailing jet generated by a piston-cylinder apparatus. In the present thesis we focus on the life cycle of vortices and the occurrence and subsequent roll-up of the shear layer is the inception of the vortex formation. The definition of mathematical models that properly describe the time evolution of shear layers is fundamental to understand how a vortex forms and develops.

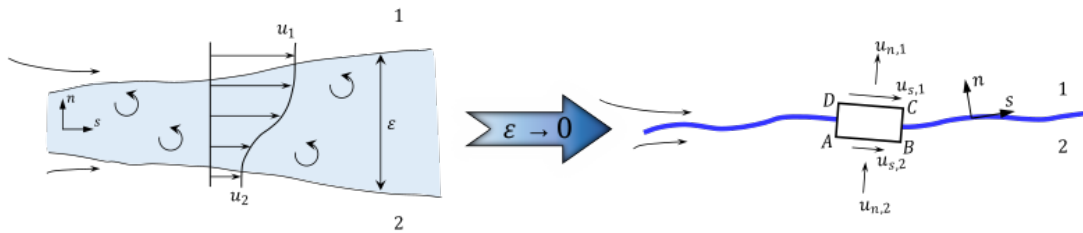


Figure 2.1: Sketch of local coordinates for a vortex sheet.

2.1.1 Vortex sheets

In moderate to high Reynolds number fluid problems, the shear layer thickness is thin compared to other length scales that characterize the flow. In the limit of zero thickness, the shear layer is described and represented as a vortex sheet. The vortex sheet is an inviscid approximation of viscous fluid layers and is governed by the Euler equation:

$$\rho \left(\frac{\partial \mathbf{u}}{\partial t} + \mathbf{u} \cdot \nabla \mathbf{u} \right) = -\nabla p \quad (2.1)$$

where ρ is the fluid density, p is the pressure and \mathbf{u} is the velocity field. The vortex sheet is a material surface in which the vorticity ω and vortex lines are enclosed in a thin surface of thickness ε . The vorticity in a vortex sheet can be expressed as:

$$\omega = \kappa \delta(n) \quad (2.2)$$

where $\delta(n)$ is the Dirac delta function and \mathbf{n} is the sheet normal coordinate. In the limit of $\varepsilon \rightarrow 0$ (Figure 2.1), the vorticity goes to infinity in a way that $\varepsilon \omega \rightarrow \kappa$. The parameter κ represent the strength of the sheet and is a finite value that is function of the position vector \mathbf{s} along the sheet. The sheet strength κ is a vector that has the same direction as the vorticity vector. The curves on the sheet parallel to κ are vortex filaments. If we consider a small rectangle in the $(\mathbf{s} - \mathbf{n})$ plane that intersects the sheet (Right side of Figure 2.1) and we integrate $\omega = \nabla \times \mathbf{u}$ around the boundaries of the rectangle, we obtain:

$$\Delta u = u_{s1} - u_{s2} = \kappa \quad (2.3)$$

where Δu is the difference of the tangential velocity between the two sides of the sheet. The previous expression can easily be generalized to give:

$$\kappa = \mathbf{n} \times \Delta \mathbf{u} . \quad (2.4)$$

In other words, a vortex sheet induces a discontinuity or a jump in the tangential velocity across the sheet.

From its definition, a vortex sheet of strength κ can represent the boundary layer that develops on the surfaces of any kind of objects. Following Eldredge [32], Graham et al. [52], the boundary vortex sheet has two constituent parts:

$$\kappa = \kappa^{nc} + \kappa^c \quad (2.5)$$

The first, κ^{nc} , is due to the body motion in an irrotational flow. The superscript nc stands for 'non-circulatory' and it has a zero-net circulation. This component is attributed to added mass and consists of a translating and rotating component. Using potential flow, Corkery et al. [19] derived the term κ^{nc} for a thin plate of chord c that translates at speed

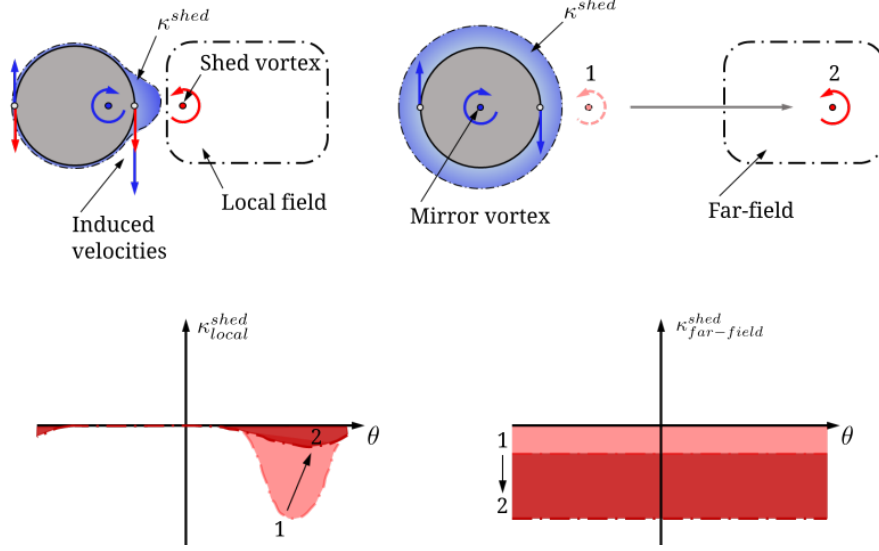


Figure 2.2: (Top) Effect of local and far-field vorticity into the boundary layer vortex sheet of a moving cylinder. (Bottom) Variation of local and far-field components of κ^{shed} as the shed vortex moves away from the cylinder. Drawings adapted from Gehlert [47].

U and rotates about the mid-chord at rotational speed Ω :

$$\kappa^{nc} = \kappa_r^{nc} + \kappa_t^{nc} = -2U \frac{x}{\sqrt{(c/2)^2 - x^2}} - \Omega \frac{2x^2 - (c/2)^2}{\sqrt{(c/2)^2 - x^2}} \quad (2.6)$$

where $-c/2 < x < c/2$ is the Cartesian component along the chord.

The second constituent part, κ^c , is associated with vorticity located away from the plate in the bulk flow field. The conservation of circulation in the flow field implies that vorticity of the opposite sign as that accumulated in the flow field needs to be located within the surface vortex sheet. As a consequence, κ^c can be seen as a 'mirror image' of vorticity present in the surrounding flow. The superscript c refers to as 'circulatory' because the associated net vorticity is not necessarily zero.

The term κ^c includes the vortex sheet contribution κ^{shed} due to vorticity that is shed away from the plate. The effects that vorticity induces on the boundary layer vortex sheet depends on how far from the surface of the object the vorticity is [47]. If we consider an external vortex shed from a moving cylinder (top of Figure 2.2), a mirror image of this vortex is placed inside the cylinder. Both the external and the mirror vortices generate induced velocity all along the cylinder surface. Immediately after the shedding, the external vortex is close to the cylinder and the corresponding mirror image vortex is closer to the cylinder surface than the cylinder centre. The induced velocities from both vortices add up in the portion of the cylinder surface close to the external vortex. On the opposite side, the induced velocities tend to cancel out. The resulting vortex sheet κ_{local}^{shed} is therefore confined to the proximity of the external vortex and almost vanishing elsewhere along the cylinder surface, as shown at the top left of Figure 2.2.

When this external vortex progressively drifts away, the associated mirror vortex moves towards the centre of the cylinder. In the limit of an infinitely far away external vortex, the associated mirror vortex is placed at the cylinder centre. The induced velocity from the vortex goes to zero because of the large distance and the mirror image at the cylinder centre induces an equal velocity all along the surface. The result is a vortex sheet of uniform strength $\kappa_{far-field}^{shed}$, as shown at the top right of [Figure 2.1](#).

These observations imply that any shed vortex contributes to either κ_{local}^{shed} or $\kappa_{far-field}^{shed}$, such that:

$$\kappa^{shed} = \kappa_{local}^{shed} + \kappa_{far-field}^{shed} \quad (2.7)$$

The distance from the cylinder determines the balance between the two terms. If the external vortex is close to the cylinder, κ_{local}^{shed} dominates. When the vortex moves away from the cylinder, κ_{local}^{shed} decreases whilst $\kappa_{far-field}^{shed}$ increases (bottom of [Figure 2.1](#)).

2.1.2 Self-induced velocity of vortex sheets

A vortex filament is characterized by a certain amount of vorticity that generates an induced velocity field in the surrounding space. The relationship between the vorticity and the induced velocity field is mathematically identical to the magnetic field generated by a current filament. In this case, the Maxwell equation:

$$\mu_0 \mathbf{j} = \nabla \times \mathbf{B} \quad (2.8)$$

is inverted to give the well-known Biot-Savart law [\[40\]](#):

$$\mathbf{B}(\mathbf{r}) = \frac{\mu_0}{4\pi} \int_C \frac{I d\mathbf{l} \times (\mathbf{r} - \mathbf{r}')}{|\mathbf{r} - \mathbf{r}'|^3} \quad (2.9)$$

Here, $d\mathbf{l}$ is an infinitesimal vector along the path C in which the electric current of density I flows and $(\mathbf{r} - \mathbf{r}')$ is the displacement vector from the wire element at point \mathbf{r}' to the point \mathbf{r} at which the field is being computed. By analogy, for a vortex filament of circulation Γ the induced velocity is:

$$\mathbf{u}(\mathbf{r}) = \frac{\Gamma}{4\pi} \int_C \frac{d\mathbf{l} \times (\mathbf{r} - \mathbf{r}')}{|\mathbf{r} - \mathbf{r}'|^3} \quad (2.10)$$

where $d\mathbf{l}$ is an element of length along the filament. Similarly, the velocity \mathbf{u}_v induced by a vortex sheet of strength κ that changes in time and along the sheet is:

$$\mathbf{u}_v(\mathbf{r}) = \frac{1}{4\pi} \int_{S_v} \kappa(\mathbf{s}, t) \frac{d\mathbf{s} \times (\mathbf{r} - \mathbf{s})}{|\mathbf{r} - \mathbf{s}|^3} \quad (2.11)$$

where dS is an infinitesimal element S_v of the sheet and \mathbf{s} is the position vector along the sheet. The integral above is finite when the point vector \mathbf{r} is outside the sheet. If we

want to evaluate the self-induced velocity of the sheet, additional considerations need to be done.

First, we describe the sheet through the complex coordinate $z = x + iy = Z(s, t)$ and we rewrite Equation (2.11) as follows:

$$u - iv = -\frac{i}{2\pi} \int \frac{\kappa(s', t) ds'}{z - Z(s', t)} \quad (2.12)$$

The evaluation of self-induced velocity of the vortex sheet requires to evaluate the integral of Equation (2.12) in the limit $z \rightarrow Z(s', t)$. This limit is finite but discontinuous because the vortex sheet induces a jump in the tangential velocity. The value of the limit depends on the side from which the sheet is approached and the sign is positive if z approaches $Z(s', t)$ from the direction in which the normal to the sheet \mathbf{n} points. If we define the averaged induced velocity on the sheet as the limit computed from the two sides of the sheet, we obtain:

$$\tilde{u} - i\tilde{v} = -\frac{i}{2\pi} \text{P.V.} \int \frac{\kappa(s', t) ds'}{z - Z(s', t)} \quad (2.13)$$

where P.V. \int is a principal value integral analogous to the Cauchy principal value. Saffman [125] showed that in absence of external forces on the sheet the circulation Γ between two points of the sheet is conserved. This statement is equivalent of saying that $d\Gamma/dt = 0$ and therefore that the circulation on the sheet is not time dependant. This result allows us to change variables and express the equation of the sheet and its strength in terms of the two independent variables Γ and t :

$$z = Z(\Gamma, t), \quad \kappa = |\partial Z / \partial \Gamma|^{-1} \quad (2.14)$$

In this way, we have $\kappa ds = \Gamma$ and we can express Equation (2.13) as:

$$\frac{\partial \bar{Z}}{\partial t}(\Gamma, t) = -\frac{i}{2\pi} \text{P.V.} \int \frac{d\Gamma'}{Z(\Gamma, t) - Z(\Gamma', t)} \quad (2.15)$$

This non-linear singular integro-differential equation is known as the Birkhoff-Rott equation [121, 10] and describes how the sheet evolves giving initial strength and shape of the sheet. This equation presents several mathematical difficulties that are discussed in the next section.

2.1.3 Mass and momentum entrainment in shear layers

The entrainment rate depends on the Reynolds number and is an inherently viscous process. The vortex sheet model is based on the inviscid assumption and does not take into account the entrainment of the surrounding fluid. However, mass and momentum are entrained into real boundary or shear layers and the inviscid vortex sheet model

should to be extended. DeVoria and Mohseni [28] proposed a dynamic inviscid model of a viscous layer, called vortex-entrainment sheet, in which the mass and momentum contained in the viscous layer are preserved. The vortex-entrainment sheet is not a streamline and replaces the viscous and rotational portion of the fluid.

We consider a sheet of velocity $\mathbf{u}(\mathbf{x}_s, t)$ that is immersed in an irrotational, incompressible fluid with density ρ and stream velocity $\mathbf{v}(\mathbf{x}, t)$, which may be discontinuous across the sheet. We assume that the external fluid may be entrained into the sheet and the resulting mass conservation is:

$$\frac{D\rho_s}{Dt} + \rho_s(\nabla \cdot \mathbf{u}) = -\llbracket \rho(\mathbf{v} - \mathbf{u}) \cdot \mathbf{n} \rrbracket \quad (2.16)$$

where $\llbracket \cdot \rrbracket$ brackets indicate the jump across the sheet and ρ_s is the sheet mass density. With this formulation, the right-hand side of mass equation is not zero and represents a source of ρ_s due to entrainment from the outer flow. For the conservation of momentum, we have the following equation:

$$\rho_s \frac{D\mathbf{u}}{Dt} - (\nabla \cdot \mathbf{T}_s + \rho_s \mathbf{f}_s) = -\llbracket \rho(\mathbf{v} - \mathbf{u})(\mathbf{v} - \mathbf{u}) \cdot \mathbf{n} \rrbracket - \llbracket p \rrbracket \mathbf{n} + \llbracket \boldsymbol{\tau} \rrbracket \quad (2.17)$$

where $\llbracket p \rrbracket$, $\llbracket \boldsymbol{\tau} \rrbracket$ are the pressure and the shear stress jumps across the sheet, \mathbf{T}_s is the stress tensor on the sheet and \mathbf{f}_s are 'body' forces acting on the sheet. As for the conservation of mass, the momentum conservation has additional source terms associated with the momentum flux and entrainment from the flow outside the sheet.

Similar to the definition of the vortex sheet strength given in Equation (2.4), the entrainment at a sheet location \mathbf{x}_s can be defined as:

$$q(\mathbf{x}_s, t) = - \int \nabla \cdot \mathbf{v}(\mathbf{x}_s, t) dn = -\mathbf{n} \cdot \llbracket \mathbf{v} \rrbracket \quad (2.18)$$

The negative sign is added such that $q > 0$ corresponds to entrainment into the sheet. On the contrary, this appears as a sink-like motion on the outer flow. From the definition of the entrainment sheet q , the induced velocity of the vortex-entrainment sheet modifies from Equation (2.11) to:

$$\mathbf{u}_v(\mathbf{x}, t) = \frac{1}{4\pi} \int_{S_v} \frac{\kappa(\mathbf{s}, t) \times (\mathbf{x} - \mathbf{x}_s) - q(\mathbf{x}_s, t)(\mathbf{x} - \mathbf{x}_s)}{|\mathbf{x} - \mathbf{x}_s|^3} dS_v \quad (2.19)$$

Following the analysis we showed in the previous section, we can express Equation (2.19) with complex variables by replacing \mathbf{x} with $z = x + iy$ and \mathbf{x}_s with $Z(s, t) = x_s(s, t) + iy_s(s, t)$, where s is the arc length coordinate. We obtain then:

$$\frac{\partial \bar{Z}}{\partial t} = \frac{1}{2\pi i} \int_{S_v} \frac{\kappa(s, t) - iq(s, t)}{z - Z(s, t)} ds \quad (2.20)$$

In the limit of $z \rightarrow Z$, Equation (2.20) represents a generalized Birkhoff-Rott equation



Figure 2.3: Flow visualization of vortices separating behind an airfoil. The snapshot is taken from the recording made by Prandtl [108].

for the vortex-entrainment sheet.

2.2 Self-similar solutions of the Birkhoff-Rott equation

Early experimental observations of vortex sheets, such as in the Klein's Kaffeelöffel experiment in which the formation of two coarse-grained vortices are observed [125], show that the roll-up develops in a self-similar way with a spiral geometry. For this purpose, we consider the following parametric equations of the sheet:

$$Z(\theta, t) = t^m f(\theta) e^{i\theta}, \quad \Gamma(\theta, t) = t^n g(\theta) \quad (2.21)$$

where f and g are real functions of the polar coordinate θ . If we substitute them into Equation (2.15), the existence of a solution requires first that the exponents are related through $n = 2m - 1$. Secondly, the functions f and g have to satisfy:

$$e^{-i\theta} \left[m f + (1 - 2m) \frac{g}{g'} (f' - i f) \right] = -\frac{i}{2\pi} \text{P.V.} \int \frac{\hat{g}' d\hat{\theta}}{f e^{i\theta} - \hat{f} e^{i\hat{\theta}}} \quad (2.22)$$

where the superscript $'$ denotes the time derivative. The above equation represents the starting point to find solutions to the Birkhoff-Rott equation that evolves as self-similar spirals.

2.2.1 Logarithmic spirals

Logarithmic spirals are often referred to as Prandtl spirals. They were first introduced by Prandtl [109] to model vortices detaching from tips of wings (Figure 2.3) and to study the influence that such vortices have on the lift of the wings. Prandtl's contribution to the study of the spirals, long time before an introduction of the notion of the Birkhoff-

Rott equation, were based on studying putative discontinuities of the velocity field, on dimensional analysis and on physical experiments.

The introduction of Birkhoff-Rott equation (Equation (2.15)) allows a more rigorous approach to Prandtl's or logarithmic spirals. We try the following ansatz:

$$Z(\theta, t) = t^m A e^{\alpha\theta} e^{i\theta}, \quad \Gamma(\theta, t) = t^n B e^{\varphi\theta}, \quad r(\theta, t) = |Z(\theta, t)| = t^m A e^{\alpha\theta} \quad (2.23)$$

where $\alpha > 0, \varphi > 0$ are real numbers and $-\infty < \theta < \infty$. The parameter $\Gamma(\theta, t)$ indicates the total circulation at radius $r(\theta, t)$, and $Z(\theta, t)$ denotes the parametrization of the spiral at time t with respect to θ (Figure 2.4).

If we substitute and reduce the above ansatz into Equation (2.22), we get:

$$e^{(2\alpha-\varphi)\theta} A^2 [m + \varphi(1-2m)(\alpha-i)] = -\frac{iB\varphi}{2\pi} \text{P.V.} \int_{-\infty}^{\infty} \frac{e^{\varphi\hat{\theta}} d\hat{\theta}}{1 - e^{(i+\alpha)\hat{\theta}}} \quad (2.24)$$

The integral in the right-hand side diverges unless α and φ have the same sign. Moreover, Equation (2.24) cannot be solved unless $\varphi = 2\alpha$. In this case, the integral can be defined by analytic continuation as follows:

$$\text{P.V.} \int_{-\infty}^{\infty} \frac{e^{\varphi\hat{\theta}} d\hat{\theta}}{1 - e^{(i+\alpha)\hat{\theta}}} = \frac{\pi i}{i + \alpha} \frac{1 + e^d}{1 - e^d}, \quad d = \frac{2\pi i \varphi}{i + \alpha} \quad (2.25)$$

If we substitute Equation (2.25) into Equation (2.24) and we eliminate A^2/B from both real and imaginary parts, we obtain:

$$\frac{1}{m} = \frac{2}{1 + \alpha^2} - \frac{2\alpha}{1 + \alpha^2} \frac{\sinh(4\pi\alpha/(1 + \alpha^2))}{\sin(4\pi\alpha^2/(1 + \alpha^2))} \quad (2.26)$$

from which it follows that for logarithmic spirals the exponent m is in the range $-\infty < m < 1/2$.

The logarithmic spiral solution defined by Prandtl [109] makes the velocity integral on the right-hand side of Equation (2.15) divergent at $\Gamma' \rightarrow \infty$ [34]. Alexander [2] overcomes this problem by considering the roll-up of several sheets around a joint centre. This leads to multi-branched configurations of N number of sheets with equations:

$$Z_p = t^m f(\theta) e^{i[\theta + 2\pi(p-1)/N]} \quad (2.27)$$

and a resulting Birkhoff-Rott equation:

$$\frac{\partial \bar{Z}_p}{\partial t}(\Gamma_p, t) = \frac{1}{2\pi i} \text{P.V.} \int \sum_{k=0}^{N-1} \frac{d\Gamma_k}{Z_p(\Gamma_p, t) - Z_k(\Gamma_k, t)} \quad (2.28)$$

where $p \in \{0, \dots, N-1\}$ indicates the number of sheets. The analysis is performed in the same way as for the above derivation, with the only difference in Equation (2.26),

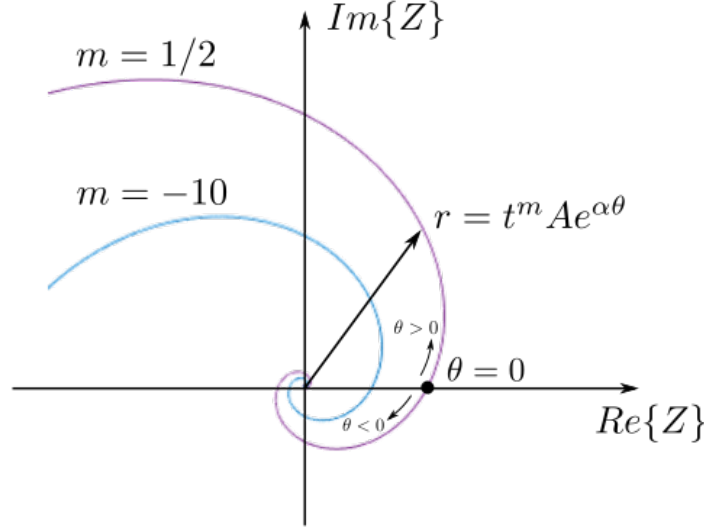


Figure 2.4: Sketch of logarithmic spirals in the complex plane for two values of the exponent m .

where the constant 4π is replaced by $4\pi/N$ in the last arguments of the right-hand side. The case of $N = 2$ corresponds to double-branched spirals that are appropriate to model the roll-up of an infinite vortex sheet [125]. Alexander [2] considered only symmetric multi-branched spirals. Elling and Gnann [35] numerically proved that the integral is not convergent at infinity for unsymmetrical solutions of the Birkhoff-Rott equation. They also argue that only spirals with $N > 3$ symmetric branches appear to make Equation (2.15) converge.

2.2.2 Semi-infinite vortex sheet

A peculiar solution of the Birkhoff-Rott equation that is not ascribed as a Prandtl's spiral is the Kaden's spiral. The Kaden's similarity solution [69] is determined for a semi-infinite vortex sheet that initially extends along the axis $0 < x < \infty$. Kaden considered the initial parametric equations of the vortex sheet to be:

$$Z = \frac{\Gamma^2}{4\gamma^2}, \quad \Gamma = 2\kappa x, \quad \kappa = \gamma x^{-1/2} \quad (2.29)$$

where the parameter $\kappa = d\Gamma/dx$ is the strength of the sheet and γ is a dimensional constant with unit measure $m^{3/2}/s$. The large intensity at the origin $x = 0$ leads the vortex sheet to roll-up into a spiral, whose self-similar geometry depends on the constant γ (Figure 2.5). When $t > 0$, the parametric equation Z is expressed in terms of Γ , κ and t . From the dimensional analysis:

$$Z(\Gamma, t, \gamma) = (\gamma t)^{2/3} \zeta(\tau) \quad (2.30)$$

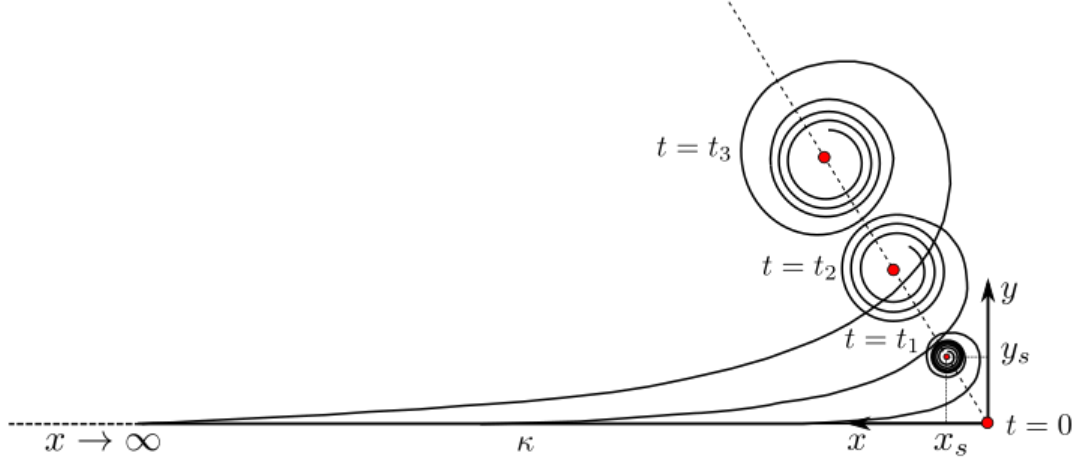


Figure 2.5: Sketch of a semi-infinite vortex sheet of strength $\kappa = \gamma x^{-1/2}$ that rolls up into a Kaden's spiral.

where $\tau = \Gamma/\gamma^{4/3}t^{1/3}$. Substituting $Z(\Gamma, t, \gamma)$ into the Birkhoff-Rott equation gives the following singular ordinary integro-differential equation for $\zeta(\tau)$:

$$2\bar{\zeta} - \tau \frac{d\bar{\zeta}}{d\tau} = -\frac{3i}{2\pi} \text{P.V.} \int_0^\infty \frac{d\tau'}{\zeta(\tau) - \zeta(\tau')}, \quad 0 \leq \tau < \infty \quad (2.31)$$

The existence of a unique solution of Equation (2.31) is an open question. A boundary condition can be defined for $\tau \rightarrow \infty$, but the problem does not provide a solution for $\tau = 0$. The failure is related to the leading edge suction on the sheet at $x = 0$, where a principal value cannot be taken [125].

Kaden made some geometrical assumptions to ensure that a solution exists. First he assumes that the end of the spiral in which the shear layer rolls-up is at $Z_0 = \zeta_0(\gamma t)^{2/3}$. Second, he considers that in the portion of the spiral closer to the centre the turns are almost circular. This last assumption is consistent with the numerical computation made by Moore [95]. It follows that the velocity field is approximately tangential to the radius r computed from the centre of the spiral. If we neglect viscous effects, the net vorticity inside concentric circles of the spiral remains constant because there is no radial motion. The circulation $\Gamma(r, t)$ must be therefore independent of t and we can write from dimensional considerations:

$$\Gamma(r) = 2\gamma(\lambda r)^{1/2} \quad (2.32)$$

where λ is an unknown constant whose estimation is discussed later. The tangential velocity v_θ at a radius r relative to the centre of the spiral is:

$$v_\theta = \frac{\Gamma}{2\pi r} = \frac{\gamma\lambda^{1/2}}{\pi r^{1/2}} \quad (2.33)$$

A fluid particle on the sheet that has a circulation Γ_P corresponds to a specific constituent

vortex line P of the sheet. The radial distance from the centre of this vortex line P is:

$$r_P = \frac{\Gamma_P^2}{4\gamma^2\lambda} \quad (2.34)$$

The vortex lines move together with the fluid and the angular coordinate θ_P of the vortex line P is given by:

$$\theta_P - \frac{\gamma\lambda^{1/2}}{\pi r_P^{3/2}}t = \text{const.} = \theta_\infty \quad (2.35)$$

For small values of r that corresponds to the portion of the spiral close to the centre and dropping the suffix P , Equation (2.35) results in the following asymptotic equation:

$$r = \left(\frac{\gamma^2\lambda}{\pi^2}\right)^{1/3} \left(\frac{t}{\theta - \theta_\infty}\right)^{2/3} \quad (2.36)$$

This is the equation of Kaden's spiral and the exponent m is equal to $2/3$. From Equation (2.36), as $\theta \rightarrow \infty$ the spiral consists of tightly circular turns, which verifies that the previously made assumptions is dynamically consistent. This simple but yet useful spiral equation is used in chapter 4 as a starting point to study the roll-up of the shear layer that is forming around a rotating plate.

Some interesting observations of Kaden's equation can be made. Firstly, Equation (2.36) works only for values of r corresponding to the central region of the spiral. Following dimensional considerations, Moore et al. [97] infers that the radius $r_0(t)$ of the central or rolled-up portion of the spiral is given by:

$$r_0(t) \sim (\gamma t)^{2/3} \quad (2.37)$$

Secondly, the length of the spiral is infinitely long. If we integrate an element ds of the spiral defined as:

$$ds = r d\theta \sqrt{a + \frac{1}{r^2} \left(\frac{dr}{d\theta}\right)^2} \sim \frac{d\theta}{\theta^{2/3}} \quad (2.38)$$

all along the semi-infinite sheet, the integral goes to infinity. Thirdly, we can also discuss about the strength of the sheet. Remembering that $\kappa = |dZ/d\Gamma|^{-1}$, we have:

$$\kappa \propto \frac{\tau^2}{t^{1/3}} \propto \frac{r}{t} \propto \frac{t^{1/3}}{\theta^{1/3}} \quad (2.39)$$

The sheet strength decreases as the spiral centre is approached. On the other side, the initial condition imposes that the sheet strength vanishes as $r \rightarrow \infty$. The consequence of these statements is that the sheet strength has a maximum along the sheet at a given time. Moore [95] showed that instability may first occur where the sheet strength is maximum.

The estimation of the unknown coefficient λ is not trivial. It cannot be determined by local considerations of the vortex sheet dynamics near the tip of the spiral, but is related

2.2. Self-similar solutions of the Birkhoff-Rott equation

to the entire solution of Equation (2.31). Betz [8] proposed a method to evaluate λ . He made the hypothesis that the vorticity inside a circle of core radius R has no torque about the centroid of the core. This hypothesis implies that:

$$2\pi \int_0^R r\omega dr = \int_0^X \gamma x^{-1/2} dx \quad (2.40)$$

where X is a length portion of the initial sheet. From the conservation of angular moment, we have:

$$-\pi \int_0^R r^3 \omega dr = \int_0^X \frac{\gamma}{x^{1/2}} (x - \bar{x})^2 dx \quad (2.41)$$

where $\bar{x} = \int_0^X \gamma x^{1/2} dx / \int_0^X \gamma x^{-1/2} dx$. If we compute the radial vorticity from Equation (2.33):

$$\omega(r) = \frac{1}{r} \frac{\partial}{\partial r} (rv_\theta) = \frac{1}{2} \frac{\gamma \lambda^{1/2}}{\pi r^{3/2}} \quad (2.42)$$

and we substitute it into Equations (2.40) and (2.41), we obtain:

$$X = \lambda R, \quad \lambda = \frac{3}{2} \quad (2.43)$$

The value of λ in Equation (2.36) can be interpreted as the degree of roll-up or tightening of the sheet. The vorticity that was initially confined in a length X of the sheet moves into a circle of radius X/λ . Pullin [111] numerically estimated λ to be approximately 2, slightly bigger than the value found by Betz [8].

Finally, the conservation of impulse allows us to estimate the location of the spiral centre $(x_s(t), y_s(t))$. The circulation that is originally in the portion between 0 and X is equal to $2\gamma X^{1/2}$. At a certain time t , this portion of the sheet is rolled up into a circle of radius $R = X\lambda$ with circulation $2\gamma(\lambda R)^{1/2}$. The conservation of impulse in the vertical direction gives:

$$2\gamma(\lambda R)^{1/2} x_s = \frac{2}{3} \gamma X^{3/2} \quad (2.44)$$

from which it follows that $x_s = X/3$. The second step is to write the equation for the vertical displacement of the spiral centre. Following Saffman [125]'s analysis, the time derivative of the impulse is $d\mathbf{I}/dt = -\pi\gamma^2/4\hat{\mathbf{i}}$. This expression is used to write the conservation of hydrodynamic impulse of the horizontal component as:

$$2\gamma(\lambda R)^{1/2} y_s = -\frac{1}{4} \pi \gamma^2 t \quad (2.45)$$

and reducing leads to $y_s X^{1/2} = -\pi\gamma t/8$. The last step is to equate the time derivative of X with the x-component of the velocity at X induced by the rolled up vortex:

$$\frac{dX}{dt} = -\frac{\gamma(\lambda R)^{1/2}}{\pi} \frac{y_s}{y_s^2 + (X - x_s)^2} \quad (2.46)$$

From Equations (2.44) to (2.46), Kaden obtained the following relations for the centre of

the spiral:

$$x_s(t) = \psi(\gamma t)^{2/3}, \quad y_s(t) = \eta(\gamma t)^{2/3} \quad (2.47)$$

where $\psi = 0.14$ and $\eta = 0.61$. These values are close to what Pullin numerically obtained in [111]. These equations show that the centre of Kaden's spiral moves along an oblique line with speed $\sim t^{2/3}$ (Figure 2.5).

2.2.3 Extension of Kaden's spiral to a finite wing

The derivation that is used to obtain Kaden's spiral equation in the above section can be extended to model vortices formed from a finite wing of span b [97]. It is assumed that the tip loading is:

$$\Gamma = 2\gamma x^{1-n_w} = 2\Gamma_0 \left(\frac{x}{b}\right)^{1-n_w} \quad (2.48)$$

where Γ_0 is the given root circulation and $0 < n_w < 1$ is a constant that represents the wing loading. The extremes $n_w = 0$ and $n_w = 1$ correspond to a delta wing configuration and to a wing along which the loading is constant and suddenly drops at zero at the tip. The intermediate case $n_w = 1/2$ is the elliptic loading. By analogy from Equation (2.32), the central portion of the spiral has a circulation:

$$\Gamma(r) = 2\gamma(\lambda r)^{1-n_w} \quad (2.49)$$

and a tangential velocity:

$$v_\theta = \frac{\gamma \lambda^{1-n_w} r^{-n_w}}{\pi} = \beta_w r^{-n_w} \quad (2.50)$$

The equation of the spiral is then:

$$r = \left(\frac{\beta_w t}{\theta - \theta_\infty} \right)^{1/(n_w+1)} \quad (2.51)$$

that is valid only in the central portion of the spiral of radius:

$$r_0(t) \sim (\beta_w t)^{1/(n_w+1)} \quad (2.52)$$

2.2.4 Accelerated flow past a wedge

A generalization of Kaden's problem, for which the exponent $m = 2/3$, is done by Pullin [111] who considered an accelerated flow past a wedge of angle $0 < \beta_a < \pi$ (Figure 2.6). The analysis is carried out by using asymptotic expansion and the flow is effectively divided in two regions. The inner region close to the edge is where the flow is dominated by roll-up of the vortex sheet. The outer region is where the flow can be

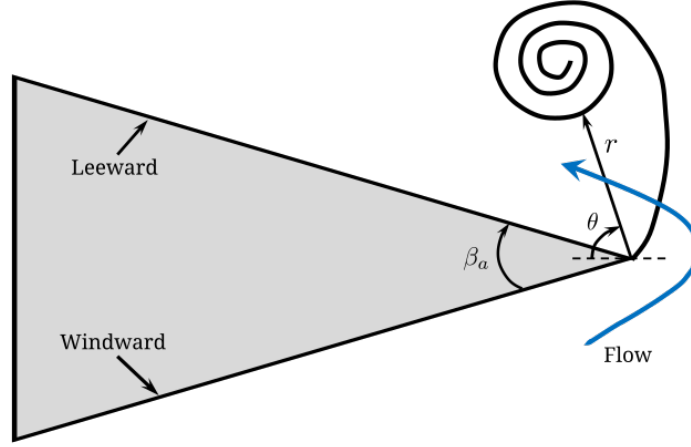


Figure 2.6: Sketch of the shear layer roll up due to an accelerated flow past a wedge of angle β_a .

considered inviscid and the complex potential depends only on the specific geometry. An attached flow past a wedge of angle β_a has a complex potential of the form:

$$w_o = -W t^{\nu_p} z^\mu \quad (2.53)$$

where $\nu_p \geq 0$ is the time exponent and depends on the flow kinematics, W is a positive dimensional constant and the exponent μ is related to the wedge angle β_a through the following relationship:

$$\mu = \pi / (2\pi - \beta_a) \quad (2.54)$$

The above equation is obtained by imposing the boundary condition $w = 0$ on the faces of the wedge.

The outer potential w_o makes the velocity at the tip of the wedge to be infinite, for the considered range of β_a . We need to impose a Kutta condition that assumes the separation of the streamlines at the tip to be smooth. This implies the presence of a stagnation point at the tip on the leeward side of the wedge (Figure 2.6). As a consequence, the complex potential of the inner flow must have, by dimensional analysis, the form:

$$w_i = W^{\frac{2}{2-\mu}} t^{\frac{2\nu_p+\mu}{2-\mu}} f\left(\frac{z}{W^{\frac{1}{2-\mu}} t^{\frac{1+\nu_p}{2-\mu}}}\right) \quad (2.55)$$

The match between the inner and the outer flows yields to the following parametric equation of the sheet:

$$Z = W^{\frac{1}{2-\mu}} t^m \zeta_0 + \left(\frac{\Gamma^m}{k}\right)^{\frac{1}{2m-1}} e^{ik^{2/(2m-1)}/\Gamma^{m/2-1}} \quad (2.56)$$

where the exponent:

$$m = \frac{1 + \nu_p}{2 - \mu} > \frac{1}{2} \quad (2.57)$$

for wedge angles $0 < \beta_a < \pi$. The first term in the right hand side of Equation (2.56) is the position of the tip of the spiral Z_T . If we centre a polar coordinate system on Z_T (Figure 2.6), the circulation at a radius r from the centre is:

$$\Gamma = k^{1/m} r^{2-1/m}, \quad k \propto W^{\frac{1}{2-\mu}} \quad (2.58)$$

Proceeding in the same exact way we did above to derive Kaden's spiral, we obtain the radial and tangential coordinates of the spiral:

$$r = k \left(\frac{t}{2\pi\theta} \right)^m, \quad \theta = \frac{\Gamma t}{2\pi r^2} \quad (2.59)$$

Figure 2.7a shows the self-similar spiral shape numerically found by Pullin [111], for a wedge of angle $\beta_a = \pi/3$. The result presents a remarkable agreement with the experimental flow visualization made by Pullin and Perry [112], in which a start-up vortex forms from a wedge (Figure 2.7b).

The equation of the spiral can be alternatively obtained directly from Equation (2.22). The integral of the right-hand side is approximated as follows (see Saffman [125]):

$$\frac{1}{f e^{i\theta}} \int_{\theta_0}^{\infty} \hat{g}' d\hat{\theta} = -\frac{g(\theta)}{f(\theta) e^{i\theta}} \quad (2.60)$$

where $\theta \rightarrow \infty$ corresponds to the centre of the spiral and $\theta = \theta_0$ is the tip of the wedge. This approximation makes possible to separate Equation (2.22) into two real equations:

$$mf + (1 - 2m)g \frac{f'}{g'} = 0 \quad 2\pi(1 - 2m)f^2 = g' \quad (2.61)$$

that have the following solution:

$$g(\theta) = c\theta^{1-2m}, \quad f(\theta) = (c/2\pi)^{1/2} \theta^{-m} \quad (2.62)$$

where the exponent $m > 1/2$. The equation of the spiral can be finally retrieved from these two real functions.

2.2.5 Zero wedge angle: flow past a flat plate

When the wedge angle β_a goes to zero, the flow can be modelled as a flat plate that moves in an inviscid fluid. Earlier attempts to find a solution for this problem have been made by Anton [3], who studied the impulsive motion of a semi-infinite flat plate. He found that the parametric equation of the sheet evolves with an exponent $m = 2/3$, the same as Kaden's problem. Refinements and improvements of Anton [3]'s solution are found by Rott [121], who considered the motion provoked by the incidence of a weak shock on a plate edge. The problem is also discussed in [111] and an exhaustive analysis

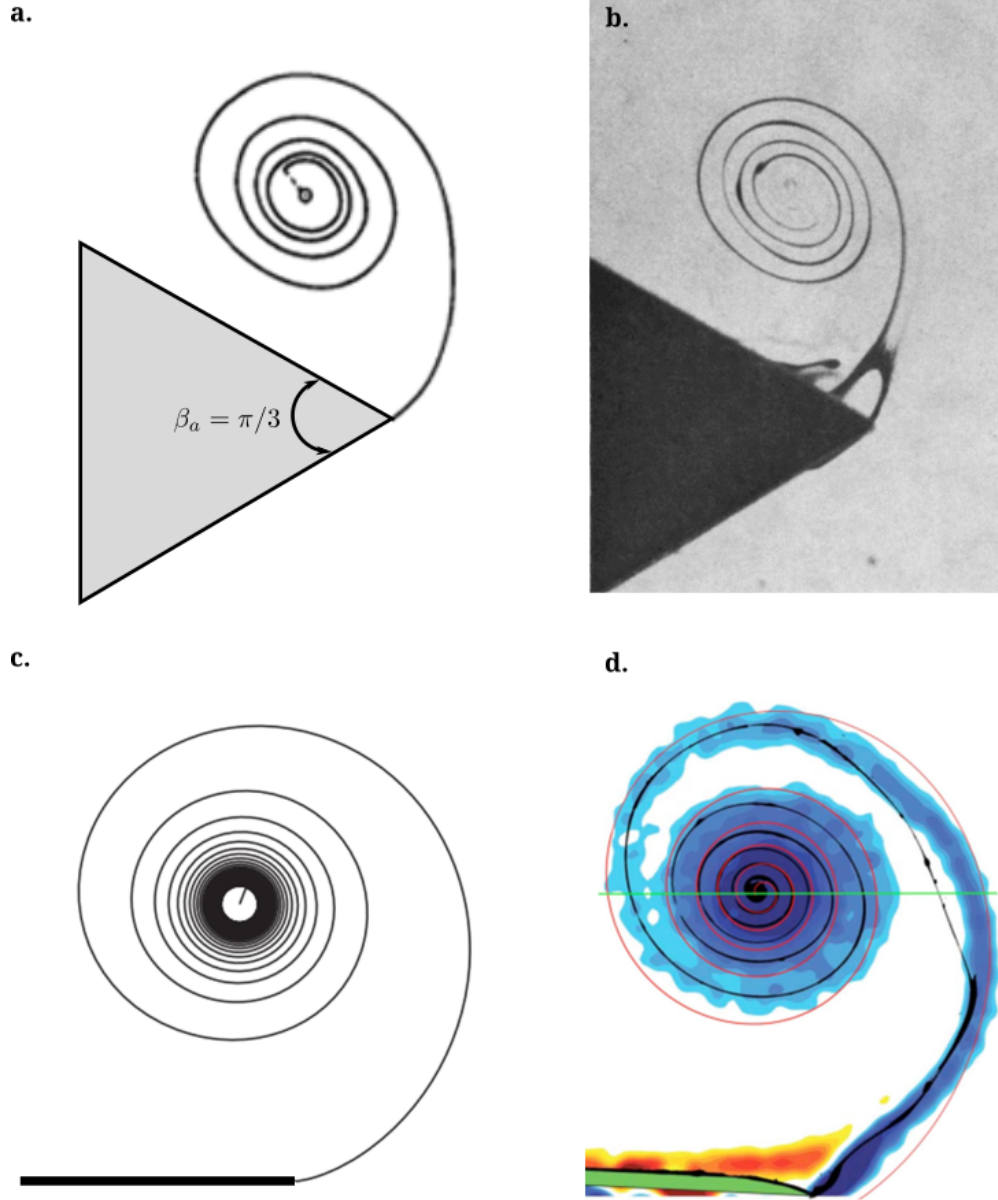


Figure 2.7: (a) Self-similar vortex sheet shape rolling-up from a wedge of angle $\pi/3$, numerically obtained by Pullin [111]. (b) Experimental visualization of dye released from the surface of a wedge of angle $\pi/3$ made by Pullin and Perry [112]. (c) Numerical solution obtained by Pullin and Sader [113] of a vortex sheet rolling-up from the edge if an impulsively started flat plate. (d) Experimental and numerical representation of a shear layer issuing from the sharp edge of an impulsively started flat plate, made by Lepage et al. [84]. The dye visualization (black line) and the numerical vortex sheet (red line) are plotted on top of the vorticity field computed from PIV.

has been recently published by Pullin and Sader [113]. They consider a two-dimensional flat plate that rotates and translates according to the following power laws:

$$U(t) = U_0 t^q, \quad \Omega(t) = \Omega_0 t^p \quad (2.63)$$

where U_0 and Ω_0 are the characteristic translational and rotational velocities. The exponents $q \geq 0$ and $p \geq 0$ specify the time dependence of the translation and rotation component. The specific kinematics of the plate leads to find similarity solutions for the vortex sheet in the form of:

$$Z(\Lambda, t) = t^m f(\Lambda), \quad \Lambda = 1 - \frac{1}{\Im t^n} \Gamma \quad (2.64)$$

where the similarity parameter Λ depends on the circulation and replaces θ in Equation (2.21). The edge of the plate is the separation point and corresponds to $\Lambda = 0$ while $\Lambda = 1$ is the vortex-sheet free edge. If we substitute Equation (2.64) into Equation (2.15), we obtain a solving equation in which the variables are the time exponents q and p of Equation (2.63). If the rotational motion of the flat plate is predominant over the translation, the solution of the equation requires the exponents to be:

$$m = 2\frac{1+p}{3}, \quad n = \frac{4p+1}{3}, \quad q > \frac{2p-1}{3} \quad (2.65)$$

which leads to:

$$Z(\Lambda, t) = t^{2(1+p)/3} f(\Lambda) \quad (2.66)$$

This solution is identified as *Type I* vortex sheet and represents a strong rolled-up vortex whose centre is above the plate and moves normally to it. *Type I* vortex sheet does not depends on the position of the rotational centre and occurs when the plate experiences a strong rotation. The shape depends on the exponent p and the spiral issuing from a plate that rotates at constant speed ($p = 0$) is shown in Figure 2.7c. While the presence of a non-zero wedge angle induces elliptical distortions on the spiral shape (Figure 2.7a-b), we observe that the turns of the spiral for the flat-plate are approximately circular. This result is experimentally confirmed by Pullin and Perry [112] and more recently by Lepage et al. [84] (Figure 2.7d), who studied the roll-up of shear layers from the sharp-edged of a rotating rectangular flat plate.

When the translation dominates over the rotational motion of the plate, the solution needs the exponent to be:

$$m = 1 + q, \quad n = p + \frac{q+1}{2}, \quad q < \frac{2p-1}{3} \quad (2.67)$$

with a parametric equation of the sheet:

$$Z(\Lambda, t) = t^{1+q} f(\Lambda) \quad (2.68)$$

This solution is referred as *Type II* vortex sheet and occurs when the self-induced velocity is small compared to the translational component. A *Type II* solution appears as a straight vortex sheet that detaches parallel to the plate at the edge and rotates as a rigid body with the plate.

Finally, when there is dynamic balance between rotation and translation, the solution requires the exponent to be $q = (2p - 1)/3$. In this condition a third class of vortex sheet, called *Type III* vortex sheet, is defined and represents an intermediate vortex-state transition between *Type I* and *Type II* solutions.

2.3 Growth of a primary coherent structure

When the shear layer rolls-up, a coherent structure emerges in the flow field and progressively grows. This structure is generally referred to as a primary vortex. As long as the vortex is attached to the body through the shear layer, the vortex grows in size and strength. Although the flow conditions and the geometry of the vortex generator have an influence on how the vortex develops, the mechanism of growth is similar among the different cases. In this section we review the growth of a primary vortex generated from three different geometries, with the aim of highlighting the main aspects about the vortex growth mechanism.

2.3.1 Start-up vortex issuing from a flat plate

We consider a two-dimensional flat plate that rotates and translates according to [Equation \(2.63\)](#). The motion of the plate causes the occurrence of a start-up vortex. The growth of this vortex can be divided in four different stages [90]. During the first stage, called Rayleigh stage, the flow is potential everywhere except for a thin layer of fluid around the body. The thickness of this layer is constant all around the plate and is proportional to $\sqrt{\nu t}$, where ν is the kinematic viscosity. As the plate moves, the convective terms of the Navier-Stokes equation become comparable with the viscous term. The structure of the start-up vortex appears in the flow and the viscous stage begins. When the convective terms progressively become predominant we have the self-similar inviscid stage. The shear layer rolls-up with a self-similar spiral shape that depends on the kinematic exponents p and q of [Equation \(2.63\)](#), as described in [section 2.2.5](#). In this stage, the vortex generated from the roll-up is still small enough to be independent of the plate geometry except for the local edge. According to Pullin and Sader [113]'s analysis, we can determine the circulation Γ that is shed in the flow. At any material point on the vortex sheet, the circulation Γ is conserved [125]. It follows

from Equation (2.64) that the total shed circulation at the plate edge ($\Lambda = 0$) is:

$$\Gamma(t) = \mathfrak{J}t^n \quad (2.69)$$

where \mathfrak{J} is the shed circulation constant. All the total shed circulation released in the flow due to the plate motion is entrained into the start-up vortex in this stage of the growth. This means that Equation (2.69) can be used to evaluate the start-up vortex circulation in the first stages of its formation. When the rotation is predominant over the translation (*Type I* vortex sheet), the shed circulation is:

$$\Gamma(t) = \mathfrak{J}t^{(1+4p)/3}, \quad \mathfrak{J} = J \left(\frac{3\hat{\beta}^4}{1+p} \right)^{1/3} \quad \text{for } q > \frac{2p-1}{3} \quad (2.70)$$

Here $\hat{\beta}$ is a fixed parameter that depends on the position of the rotation centre and on the ratio rotational-to-translational plate velocities. The parameter J is the same dimensionless constant that Pullin [111] numerically determined.

When the translation is the dominant motion (*Type II* vortex sheet), the shed circulation is given by:

$$\Gamma(t) = \mathfrak{J}t^{p+((1+q)/2)}, \quad \mathfrak{J} = \hat{\beta} \sqrt{\frac{2\pi}{1+q} \frac{\Gamma_c \left(1 + \frac{p}{1+q} \right)}{\Gamma_c \left(\frac{3}{2} + \frac{p}{1+q} \right)}} \quad \text{for } q < \frac{2p-1}{3} \quad (2.71)$$

where Γ_c is the complete gamma function and does not indicate the circulation. When there is dynamical balance between translation and rotation (*Type III* vortex sheet) the shed circulation is identical to Equation (2.70), with the parameter $\mathfrak{J} \approx 1.11072$ for $\hat{\beta} < 1$ and $\mathfrak{J} \approx 1.178\hat{\beta}^{1/3}$ for $\hat{\beta} > 1$. These results are numerically confirmed by Koumoutsakos and Shields [74] and more recently by Xu and Nitsche [146], who used them to scale the core trajectory and circulation of the start-up vortex. Rosi and Rival [120] experimentally show that the circulation in the start-up vortex does not depend on the instantaneous Reynolds number and follows the inviscid prediction.

Finally, during the fourth and last stage the whole geometry of plate influences and modifies the start-up vortex growth that progressively drifts downstream the edge of the plate.

2.3.2 Vortex ring generated from a piston-cylinder apparatus

If we discharge a volume of fluid through a cylinder of diameter D by pushing a piston inside the cylinder at a speed U_P , an axisymmetric vortex ring is generated. Gao and Yu [46] accurately describe and model the growth mechanism of the vortex ring. During the first stage, the cylindrical shear layer separated from the cylinder rolls-up and all the

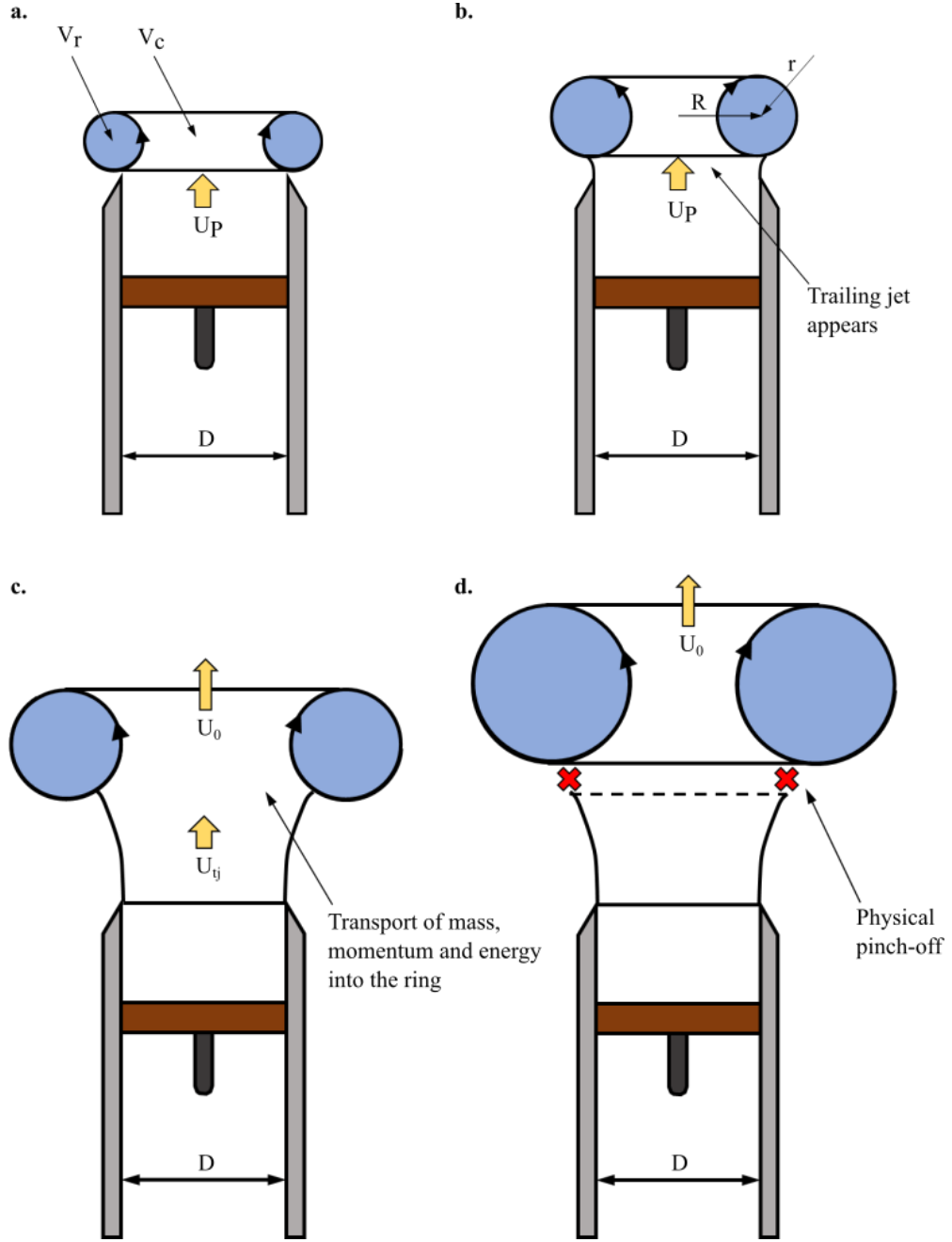


Figure 2.8: Sketch of the vortex ring growth in a piston-cylinder apparatus. (a) Beginning of the first stage with the vortex ring that remains close to the nozzle exit. (b) End of the first stage in which the vortex ring diameter is as big as the nozzle diameter and the trailing jet appears. (c) Beginning of the second stage in which the vortex ring moves away from the cylinder and the growth is sustained by the flux of vorticity from the trailing jet. (d) Physical pinch-off of the vortex ring from the trailing jet that indicates the end of the second stage. Drawings adapted from Gao and Yu [46].

fluid discharged from the nozzle is entrained into the vortex. The surrounding ambient fluid is not entrained in the vortex and the entrainment effect is therefore negligible in this phase. If we use the slug model that assumes the wall-normal velocity component to be smaller than the stream-wise component, the total circulation Γ discharged from the nozzle into the vortex ring is:

$$\Gamma(t) = \frac{1}{2}U_P^2 t \quad (2.72)$$

The vortex ring can be described as a core of radius r and volume V_r whose centre is at R from the ring centre, inside which a volume V_c is entrained (Figure 2.8a-b). As the vortex ring grows, both R and r increases with time but the core of the vortex ring is still sufficiently small to be approximated as a Norbury vortex [101] with a dimensionless radius $\varepsilon \approx r/R$. This approximation allows us to calculate the energy E and the impulse I of the vortex ring using Fraenkel [42]'s second order formulas (see also [133]):

$$\begin{aligned} E &= \frac{1}{2}\rho R\Gamma^2 \left[\ln\left(\frac{8}{\varepsilon}\right) - \frac{7}{4} + \frac{3}{8}\varepsilon^2 \ln\left(\frac{8}{\varepsilon}\right) \right] \\ I &= \rho\pi\Gamma R^2 \left(1 + \frac{3}{4}\varepsilon^2 \right) \end{aligned} \quad (2.73)$$

where ρ is the fluid density. The core size is also smaller compared to the nozzle diameter D and the roll-up of the shear layer can be modelled as a self-similar inviscid process in two dimensions, in which the radius R of the vortex ring increases as:

$$R = 0.5D + aDt^{2/3} \quad (2.74)$$

The coefficient a is experimentally determined by Didden [30] to be 0.17. This stage is very similar to the third stage of the start-up vortex generated from a flat plate and is also testified by the $2/3$ time exponent. The vortex ring rapidly grows in the radial direction and it does not translate downstream the cylinder exit. Didden [30] observed that the vortex does not move in the axial direction until the ring radius R is slightly larger than the radius of the nozzle. Based on his experiments, the condition $R = 0.54D$ represents the end of the first stage (Figure 2.8b). No trailing jet is observed during this stage.

The occurrence of the second stage is associated with the appearance of the trailing jet (Figure 2.8c). The vortex ring starts moving in the axial direction and now, its growth is also supported by the flux from the trailing jet. For this reason, the flux of circulation, impulse and energy into the vortex ring have to be evaluated. If we consider U_{tj} to be the local trailing jet velocity near the ring, the vorticity flux at the back of the ring is:

$$\frac{d\Gamma}{dt} = \int_0^\infty (U_{tj} - U_0)\omega dr \approx \frac{1}{2}U_{tj}^2 - U_{tj}U_0 \quad (2.75)$$

where U_0 is the translational velocity of the leading vortex ring and increases as the

vortex grows. The flux of impulse and energy from the trailing jet are:

$$\begin{aligned}\frac{dI}{dt} &= \pi(R-r)^2 \rho U_{tj} (U_{tj} - U_0) \\ \frac{dE}{dt} &= \frac{1}{2} \pi(R-r)^2 \rho U_{tj}^2 (U_{tj} - U_0)\end{aligned}\tag{2.76}$$

These additional differential equations coupled with [Equations \(2.72\)](#) and [\(2.73\)](#) describe the evolution of the dynamical properties of the vortex ring during the second stage of growth.

2.3.3 Leading edge vortex from a pitching wing

The pitching motion of a wing or an airfoil in the flow field results in the formation of a coherent structure. This structure is often referred as leading edge vortex (LEV) because it is generated from the leading edge of the wing. The growth stages of a LEV induces a transient fluid dynamic load on the wing. At lower Reynolds number, typical of insects flight [\[12, 36\]](#), the formation of LEVs produces transient high lift on the wing that helps insects to fly. The growth of a LEV from a constantly pitching airfoil makes the lift coefficient to increase above the static stall angle, in a phenomenon that is known as dynamic stall [\[100\]](#).

Eldredge and Jones [\[33\]](#) made an extensive review about the description and modelling of the LEV growth. When the wing start pitching, the flow in proximity of the leading edge is accelerated and vorticity generated at the edge forms a shear layer that quickly rolls up into the LEV. At this stage, the roll-up of the shear layer can again be modelled as a vortex sheet that evolves with a self-similar spiral shape. At early times, the LEV is observed as a closed recirculation region on the suction side of the plate. The LEV size occupies approximately half of the wing chord. As the wing keeps pitching, the LEV is fed by the shear layer and grows in both size and strength. The estimation of the amount of circulation into the LEV core requires to first identify the LEV contours. In experiments and simulations, the boundaries ∂A of the LEV may be defined by Eulerian methods, such as the Γ_1 and Γ_2 functions [\[51\]](#) or the swirling strength criterion [\[147\]](#), and Lagrangian coherent structure analysis [\[58\]](#) (see [chapter 3](#)). If we take $\mathbf{u} = (u, v, w)$ and $\boldsymbol{\omega} = (\omega_x, \omega_y, \omega_z)$ as the three-dimensional velocity and vorticity vectors, all the components that contribute to the net rate of change of the LEV circulation are [\[103\]](#):

$$\begin{aligned}\dot{\Gamma}_{LEV} &= - \int_{\partial A} w \frac{\partial \omega_z}{\partial z} dA + \int_{\partial A} \left(\omega_x \frac{\partial w}{\partial x} + \omega_y \frac{\partial w}{\partial y} + \omega_z \frac{\partial w}{\partial z} \right) dA \\ &\quad + \nu \int_{\partial A} \left(\frac{\partial^2 \omega_z}{\partial^2 x} + \frac{\partial^2 \omega_z}{\partial^2 y} + \frac{\partial^2 \omega_z}{\partial^2 z} \right) dA + \int_{\sigma} u_{\sigma} \omega_z d\sigma + \Phi\end{aligned}\tag{2.77}$$

The first term on the right-hand side of [Equation \(2.77\)](#) is the circulation flux due to span-wise convection. The vortex tilting and stretching is described by the second term

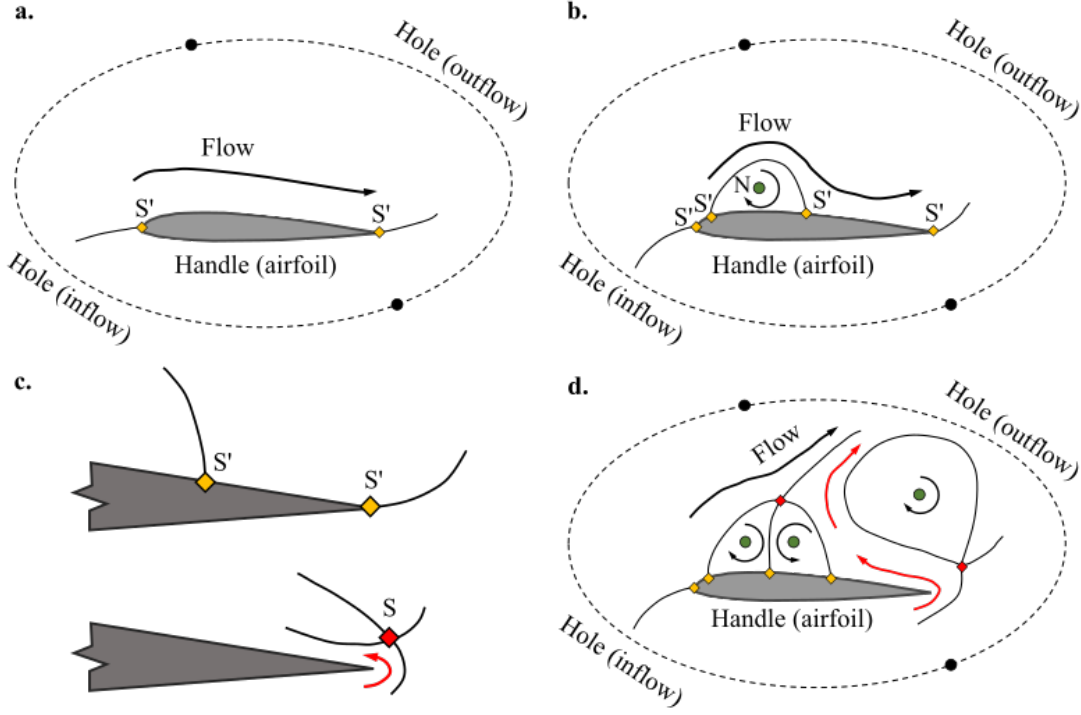


Figure 2.9: (a) (b) (c) the rear stagnation point S' and trailing-edge stagnation point S' merge to a (separated) fullsaddle S such that the channel for reversed flow opens, as indicated by the red arrow (d) write descriptions. Drawings adapted from Rival et al. [118].

and can be interpreted as the local amplification, or reduction, caused by local rate of strain. The circulation loss due to viscous diffusion is taken into account by the third term. The fourth term is the main component of the LEV growth and indicates the flux of circulation due to the feeding shear layer. The symbol σ indicates the direction perpendicular to the shear layer. Finally, the term Φ estimates the flux of secondary vorticity advected into the LEV from the surface of the plate. The secondary vorticity is a region of opposite-sign vorticity generated along the surface of the wing due to the growth of the LEV. The terms in the right-hand side of Equation (2.77) represent all the sources and sinks of vorticity and describe how the LEV circulation changes in time.

To characterize the different stages of LEV growth, Rival et al. [118] performed a topological analysis of the flow and compared it with experimental results. As pointed out by Foss [41], a flow domain is defined by the Euler characteristic:

$$\chi_{surface} = 2 - 2 \sum N_{handles} - \sum N_{holes} \quad (2.78)$$

This parameter is a topological invariant and remains constant for a given number of handles and holes across the domain. Handles are obstacles in the flow domain while inlet and outlet cross-sections are referred to as holes. For a moving wing in

the flow field, the only handle in the domain is the wing itself and the inflow and outflows boundaries are the two holes, as shown in [Figure 2.9](#). From [Equation \(2.78\)](#), the condition $\chi = -2$ has to be satisfied by all the possible singular points in the flow domain. In particular, full nodes N and saddles S are singular points in the flow and half-nodes N' and half-saddles S' are singular points on solid walls. When computing the Euler characteristic, full singularities are weighted twice.

The invariance of the Euler characteristic gives the topological scenarios shown in [Figure 2.9](#). The attached flow is modelled with two half-saddles S' placed at the leading and trailing edges of the wing ([Figure 2.9a](#)). The occurrence of the LEV leads to two additional half saddles S' on the wing and a full node N at the centre of the LEV region ([Figure 2.9b](#)). These singular points mark the location of the LEV and they do not change the invariance of the Euler characteristic. As the LEV grows, the half saddle point closer to the trailing edge moves toward the trailing edge. Once both half-saddles merge, the resulting new full saddle S separates from the trailing edge. This separation opens a channel for reversed flow at the trailing edge, as indicated in [Figure 2.9c](#), that is pushed towards the shear layer.

2.4 Limit process of the vortex formation

A vortex can not grow endlessly. When the vortex reaches a certain size and circulation, the shear layer does not feed the vortex anymore. The vortex is now physically separated from the shear layer and progressively moves away from the vortex generator. The vortex separation is observed in all the studied vortex configurations and happens when the circulation entrained in the core stops increasing. However, the precise identification of vortex separation is complicated. When the separation occurs, the vortex is very close to the shear layer and is tricky to distinguish the vortex core from the shear layer. As a consequence, the measure of the moment at which the circulation stops increasing is uncertain and many studies have been carried out to address this topic. In this section, we first mention how the primary vortex separates from the vortex generators we mentioned in the previous section. After that, we move the focus on the definition of a specific dimensionless number that identifies the vortex separation among all the different flow conditions.

2.4.1 Mechanism of separation

When a start-up vortex develops from the edge of a two-dimensional plate, four different stages of growth are identified [90]. At the end of the fourth stage, the start-up vortex is not fed by the shear layer anymore. From this moment, the circulation generated from the plate motion and estimated by [Equations \(2.70\) and \(2.71\)](#) using inviscid theory, is

not entrained in the core of the start-up vortex. Sattari et al. [126] made an interesting argument to identify the vortex growth limit and is related to the "flattening" of the shear layer. From flow visualization, they observe that streamlines are directed towards the vortex core before the separation whereas they point away from the core after the separation. This leads to the argument of the shear layer "flattening", defined as the competition between the tendency of shear layer to go straight in the stream-wise direction and go upwards due to the vortex induced velocity. When the vortex is small and close to the edge, the contribution of the induced velocity on the shear layer is high and fluid particles go in the vortex core. When the vortex progressively grows and moves away from the edge, the induced velocity decreases and the shear layer flattens. This brings to a gradual separation of the start-up vortex from the shear layer. If we scale the vortex circulation Γ with respect to the maximum velocity u_{max} within the shear layer velocity and the distance S between the vortex centre and the shear layer, Sattari et al. [126] showed that separation occurs when $\Gamma/(u_{max}S) \approx 1.5$.

For a piston-cylinder apparatus, the vortex ring stops growing at the end of the second stage. In this phase the vortex ring detaches from the trailing jet and Equations (2.72) and (2.73) fails because the flux from the trailing jet no longer exists. The vortex pinches-off and additional vorticity flux is rejected by the primary vortex ring [49] and instead forms secondary vortices similar to a Kelvin-Helmholtz instability [20]. The pinch-off of a vortex ring can be explained by making some energetic assumptions. The Kelvin [71] - Benjamin [7] variation principle assumes that a steady, axisymmetric and translating vortex can only accept additional vorticity from a feeding shear layer if the dimensionless energy of the new configuration is greater than the dimensionless energy of an alternative vortex ring configuration in which the additional vorticity is rejected by the vortex ring. To apply the Kelvin-Benjamin variational principle, we need to compare the energy provided by the piston E , with the energy required for a steadily translating vortex ring E_R . This approach needs the computation of the dimensionless energy of the vortex as follows:

$$E^* = \frac{E}{\sqrt{\rho I \Gamma^3}} \quad (2.79)$$

The vortex separates when the dimensionless energy E^* delivered by the piston becomes lower than the energy of a steadily translating vortex ring [49]. Mohseni and Gharib [94] found the limiting value of the dimensionless energy to be $E^* \approx 0.3$.

The vortex ring pinch-off can be also explained with a kinematic argument. When the vortex ring moves faster than its feeding shear layer, the pinch-off occurs. The shear layer velocity represents the critical separation velocity of the vortex ring. Mohseni and Gharib [94] estimated the velocity of the feeding shear layer to be around half of the piston velocity. This estimation is confirmed by Shusser and Gharib [131], who found that the vortex ring translational velocity is 59% of the piston speed when the dimensionless energy $E^* \approx 0.3$. This result suggests that the translational velocity and the dimensionless energy of the vortex ring are related quantities. This relationship

between the velocity U_0 of a viscous steady vortex ring and its dimensionless energy is estimated by Saffman [124] to be:

$$U_0 = \frac{2\Gamma}{\pi R} \left(E^* \sqrt{\pi} + \frac{3}{4} \right) \quad (2.80)$$

where R is the radius of the vortex ring (Figure 2.8).

The growth of a LEV from the leading edge of a wing induces the formation of opposite sign vorticity along the surface of the airfoil. The opposite sign vorticity is referred to as secondary vorticity and its magnitude increases together with LEV strength. The growth of secondary vorticity has two main effects. First, it pushes the LEV away from the wing surface and second, it cuts off the LEV connection with the feeding shear layer. This is known as vortex-induced separation [107] and is associated with a rapid drop in lift, as it happens when a pitching wing dynamically stalls [100]. This process is also accelerated by the trailing edge vorticity. As shown in Figure 2.9c, the occurrence and separation of a full saddle at the trailing edge gives rise to reversed flow. This flow moves from the trailing edge towards the feeding shear layer. By doing so, it enhances the secondary vorticity along the surface accelerating the LEV separation process [118]. The LEV separation can also be modelled through the same topological analysis shown in section 2.3.3 Two additional half-saddles represent the region of secondary vorticity inside which we place a new full node, a second full node is placed in the shear layer region and finally, a new full-saddle is added where the LEV separates from the shear layer (Figure 2.9d).

2.4.2 Vortex formation number

In all vortex dominated flows, the vortex formation has a limit above which the vortex can not entrain vorticity anymore from the feeding shear layer. This situation suggests the possibility to define a parameter that can be used to identify vortex pinch-off in the different flows. According to Dabiri [20], we first need to properly define a dimensionless vortex formation time as:

$$T^* = \frac{C\Gamma}{DU} \quad (2.81)$$

where Γ is the vortex circulation, D and U are characteristic speed and length scales and the constant factor C depends on the inverse dimensionless vorticity flux provided by the vortex generator. Once T^* is defined, the vortex pinch-off is identified by the vortex formation number \hat{T} that is the vortex formation time at which the total circulation fed by the vortex generator is equal to the final vortex circulation.

The vortex formation number was initially defined for vortex rings generated from a piston-cylinder apparatus. If we compute the vortex circulation according to Equa-

tion (2.72) and we consider the piston velocity U_P and the nozzle diameter D as the characteristic length scales, we arrive to:

$$T^* = \frac{U_P t}{D} = \frac{L}{D} \quad (2.82)$$

The dimensionless constant C is equal to 2 since the vorticity flux is approximately 1/2 [30]. If the piston strokes along a length $L = U_P t$, the dimensionless time of a piston-cylinder configuration is equivalent to the stroke ratio, described as the ratio of length to diameter of the ejected fluid column. For a wide range of piston speed profiles, the vortex ring reaches its critical value of dimensionless energy and separates from the feeding shear layer when the dimensionless time is around 4. This dimensionless time is referred as vortex formation number $\hat{T} = 4 \pm 0.5$ [49, 93, 116]. Limbourg and Nedić [87] have recently improved the prediction of the vortex formation number for different orifice geometries by including the effect of the flow contraction in the slug model at the exit of the nozzle [87]. When $T^* < \hat{T}$, the maximum circulation that a vortex ring can reach is equivalent to the total circulation discharged by the piston. The vortex size and circulation do not increase anymore when $T^* > \hat{T}$.

The wide variety of cases in which the vortex formation number is approximately 4 suggests the existence of a unique formation number that is valid for all vortex configurations. This idea is analysed and explained by Dabiri [20], who condensed it in the concept of optimal vortex formation. The optimal vortex formation can be seen as a unifying principle to understand the various solutions adopted in nature by animals to efficiently achieve propulsion. If we consider the cruise motion of fishes and cetaceans, Triantafyllou et al. [137] found a peak in propulsive efficiency when the Strouhal number, defined as:

$$St = \frac{fd}{U_\infty} \quad (2.83)$$

with f the flapping frequency, U_∞ the cruising speed and d the peak-to-peak motion amplitude, is in the range $0.25 \leq St \leq 0.35$. Taylor et al. [135] claimed that even flying animals such as birds or bats, have evolved stroke kinematics to satisfy the same range of the Strouhal number. Dabiri [20] proposed that the inverse of the Strouhal number is essentially equivalent to the concept of optimal vortex formation. As a consequence, the cruising kinematics of swimming and flying animals converge towards a formation time \hat{T} ranging from 3 and 4. The optimal vortex formation has also been extended to more complex cases, such as the vortex developing inside a left ventricle. Results show that in healthy condition, the formation time ranges between 3.3 and 5.5 [50], which is in agreement with laboratory results [22] and with the expected value of the optimal vortex formation.

Rival et al. [117] applied the concept of optimal vortex formation for a leading edge vortex forming from a plunging airfoil and used it as a criterion for LEV pinch-off. A similar approach is also used by Onoue and Breuer [103] for LEV generated from swept

and upswept pitching wings. They define a dimensionless time that takes into account the effect of the pitch rate and the leading-edge sweep angle as follows:

$$T^* = \frac{tU_{sl}}{\beta_{pp}c} \quad (2.84)$$

where U_{sl} is the shear layer velocity and $0.5 < \beta_{pp} < 1.5$ is a parameter related with the distance between the rotation point and the mid-chord ($\beta_{pp} = 1$ when the rotation point is at the mid-chord). In the way it is defined, Equation (2.84) is analogous to the dimensionless time of Equation (2.81). The parameter β_{pp} has the role of the constant factor C that depends on the physical configuration of the vortex generator. The dimensionless time is scaled by $C = 1/\beta_{pp}$ to account for the fact that the onset of LEV formation is either advanced or delayed as the rotation point of the wing is placed forward or after of the mid-chord [53]. The circulation of the LEV stops growing around a dimensionless time $T^* \approx 4$ for all the different leading-edge sweptback angles and pitch rates. The applicability of the optimal vortex formation in this configuration is also confirmed by energetic considerations. We know that the Kelvin-Benjamin variational principle is only defined for steady axisymmetric vortex ring. The LEV that forms in the wake of a pitching wing is not a steady axisymmetric vortex ring and the application of Kelvin-Benjamin variational principle is not ensured. Onoue and Breuer [103] also showed that the dimensionless energy of the LEV decreases down to a limiting value of 0.3 when the dimensionless time $T^* \approx 4$. This is the same number found for vortex rings [94] and the result extends the Kelvin-Benjamin variational principle to a LEV formed from a pitching wing.

We do also report numerical and experimental studies that manipulate the vortex formation time from the optimal number of 4. The growth and the formation number of a vortex can be controlled by changing the geometry or the kinematics of the specific vortex generator. Shusser et al. [133] delayed the formation number by constantly accelerating the piston instead of impulsively starting it. A delay of 10 % in the vortex formation time is also shown by Dabiri and Gharib [21], who immersed a piston-cylinder apparatus in a uniform bulk counterflow. On the contrary, Krueger et al. [80] reduced the formation number by putting the piston-cylinder apparatus in a uniform coflow. In analogy with the time-varying motion of the velum of a jellyfish, Dabiri and Gharib [23] delayed the formation number of the vortex ring up to $\hat{T} \approx 8$, by varying in time the cylinder exit diameter during the vortex formation. In direct contrast to the concept of a unique optimal formation, Afanasyev [1] observed that dipoles ejected from a nozzle do not pinch-off for values of the stroke ratio up to 15. Higher values of the optimal vortex formation are experimentally found by [88], who showed that the vortex ring ejected from an orifice reaches its maximum energy around a non-dimensional time of 6-7. Pedrizzetti [106] observed a stable growth evolution of the vortex ring with no evidence of pinch-off, proving that the optimal formation concept is not satisfied for a two-dimensional starting orifice flow.

Based on the literature studies we found about the topic, the debate whether the optimal vortex formation is a unifying principle or not is still open. Moreover, when considering more complex flow configurations such as the shedding of dipoles, the definition of an optimal vortex formation requires a view towards the three-dimensional vortex structure. Finally, no vortex formation numbers are defined in literature for pure rotating or translating flat plates.

2.5 Flow field after primary vortex separation

When the shear layer stops feeding the primary vortex, additional vorticity provided by the vortex generator is rejected from the vortex. This vorticity gives rise to the formation of other coherent structures that are generally refer to as secondary vortices. We observe the formation of secondary vortices as a result of a shear layer instability, from the interaction between the primary vortex and a close-by solid surface and from other mechanisms. In this section we give an overview about the different processes that lead to the formation of secondary vortices.

2.5.1 Kelvin-Helmholtz instability

The most common example of instability that occurs in fluid dynamics is the Kelvin-Helmholtz (KH) instability (Kelvin [71], Helmholtz [63]). This phenomenon occurs at the interface of two different fluids that travel at different velocities or when there is velocity shear in a single continuous fluid. We can observe this kind of instability at different scales. For instance, the wind interaction with forming clouds in the atmosphere leads to the occurrence of repetitive curlicues on the stable layer that resemble ocean breaking waves (Figure 2.10a). These waves will grow to eventually induce the formation of individual coherent structures. A similar pattern is also noted on the atmosphere of Jupiter, where bands of fluid at different velocities interact below the Great Red Spot giving rise to the formation of several coherent structures (Figure 1.1e). We also recognize the pattern of KH instability in the previously mentioned vortex generators. For instance, we can observe KH instability behind the trailing edge of a moving airfoil in the early flow visualization made by Prandtl [108] (Figure 2.3). Several coherent structures resulting from an unstable shear layer generated from the sharp edge of a flat plate are also detected in the flow visualization of Küchemann and Weber [81] (Figure 2.10b). KH instability appears in the flow topology even if we impulsively accelerate a thin ellipse instead of a flat plate, as confirmed by the numerical analysis of Wang et al. [138] and shown in Figure 2.10c. The shear layer does not always manifest signs of instability. Luchini and Tognaccini [90] show that the emergence of secondary vortices as a result of an unstable shear layer (Figure 2.10d) occurs only when the Reynolds number, derived from inviscid assumptions on the path followed

by the primary vortex core (see Pullin and Perry [112] for further details about the exact derivation), is higher than 4500. A slightly higher critical Reynolds number of 5000 above which the shear layer becomes unstable and secondary vortices appear is identified by Pedrizzetti [106]. Finally, the trailing jet issuing from a piston-cylinder apparatus shows KH instability when the primary vortex ring pinches-off. At this stage, the primary vortex ring is not fed anymore by the trailing jet and additional vorticity flux is rejected by the primary vortex ring [49]. The rejected vorticity leads to the occurrence of secondary vortices similar to a Kelvin-Helmholtz instability in the trailing jet [20] (Figure 2.10e).

A rigorous and general mathematical approach to describe Kelvin-Helmholtz instability is presented in Saffman [125]. We consider an undisturbed vortex sheet with parametric equation $Z = \Gamma/U$ and strength $\kappa = U$. This sheet is then perturbed with an infinitesimal periodic disturbance such that the parametric equation becomes:

$$Z = \frac{\Gamma}{U} + \sum_{-\infty}^{\infty} a_n(t) e^{in\Gamma\alpha} \quad (2.85)$$

where $a_n(t)$ are infinitesimal coefficients. If we substitute the above equation into the Birkhoff-Rott equation (Equation (2.15)), we get:

$$\sum_{-\infty}^{\infty} \frac{d\bar{a}_n}{dt} e^{-in\Gamma\alpha} = \frac{iU}{2\pi} \text{P.V.} \int_{-\infty}^{\infty} \frac{d\theta}{\theta} \left(1 + \sum_{-\infty}^{\infty} U a_n e^{in\Gamma\alpha} \left(\frac{1 - e^{in\theta\alpha}}{\alpha} \right) + O(a_n^2) \right) \quad (2.86)$$

with $\theta = \Gamma' - \Gamma$. If we reduce the above equation by considering $\text{P.V.} \int_{-\infty}^{\infty} d\theta/\theta = 0$ and $\text{P.V.} \int_{-\infty}^{\infty} (1 - e^{in\theta\alpha}) d\theta/\theta^2 = \pi n\alpha$, and we equate the coefficients of $e^{-in\Gamma\alpha}$ at the first order, we have:

$$\frac{d\bar{a}_n}{dt} = -\frac{i\pi nU}{\lambda_d} a_{-n}, \quad -\infty < n < \infty \quad (2.87)$$

where $\lambda_d = 2\pi/\alpha U$ is the wavelength of the disturbance. Then, the n th Fourier coefficients exponentially grow as $e^{\sigma_d t}$, with $\sigma_d = \pm\pi nU/\lambda_d$, and the sheet is unstable. The smaller the wavelength λ_d or the higher the mode n of the disturbance, the faster the growth rate of the instability.

The discussion of the stability of a vortex sheet is a tricky topic. Saffman [123] suggests that KH instability could be suppressed by stretching the sheet. The stretching of the sheet implies that its strength κ decreases in time as the sheet rolls-up. Moore and Griffith-Jones [96] discussed in details the stability of an expanding circular vortex sheet. Centring a polar coordinates system at the centre of the expanding circular sheet, the imposed disturbance deforms the circle into the curve:

$$r = R(t) + \varepsilon(t) e^{ist} \quad (2.88)$$

where $|\varepsilon| \ll R$ and s is a positive integer. The flow outside the sheet is irrotational and

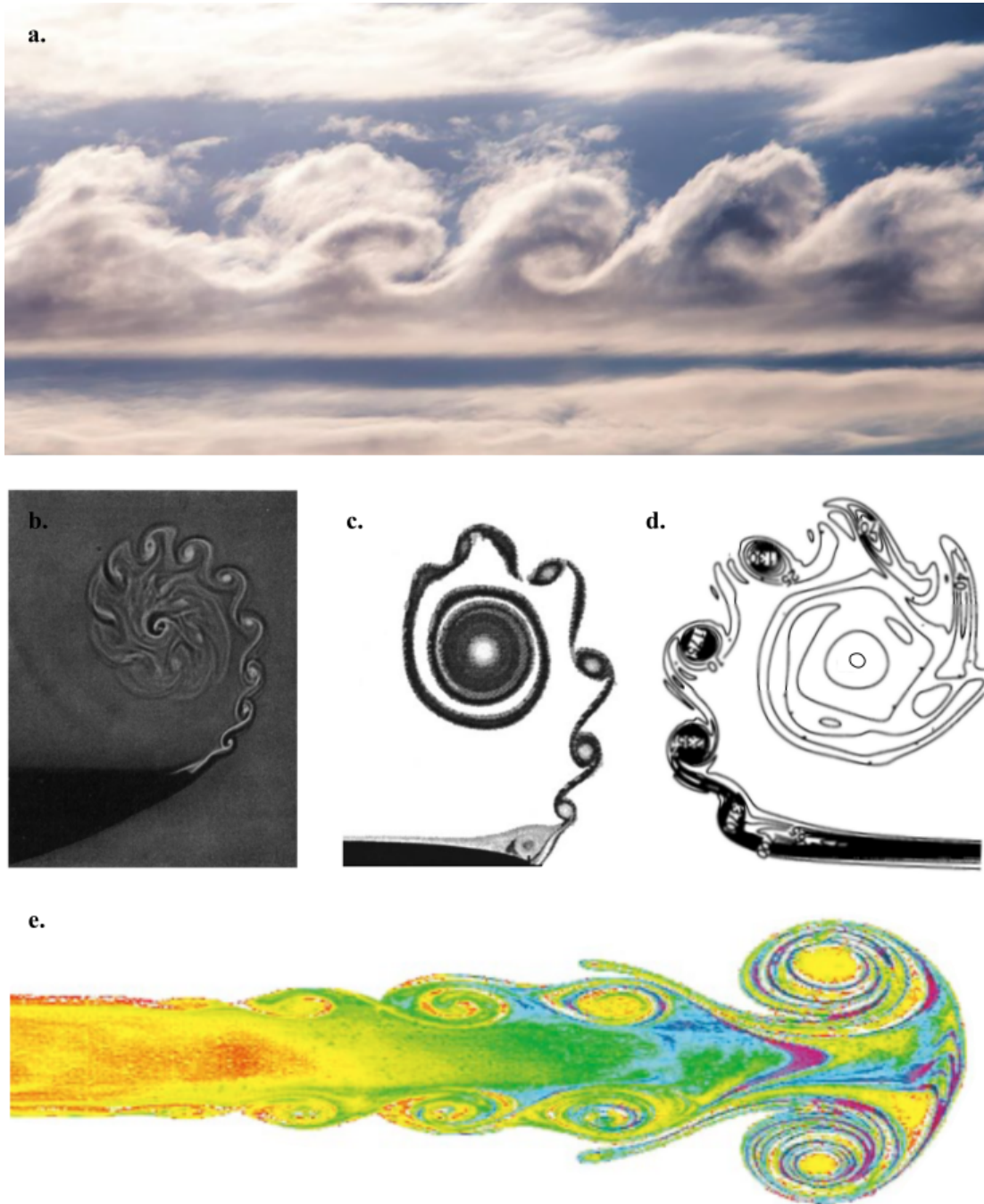


Figure 2.10: (a) Kelvin-Helmholtz instability in forming clouds observed in Tupper Lake, New York, in the Adirondack Mountains. (b) Flow visualization of shear layer fluctuations and instability issuing from the sharp edge of a flat plate. Image taken from Küchemann and Weber [81] (c) Shear layer instability behind an impulsively started thin ellipse. Image taken from the numerical analysis of Wang et al. [138]. (d) Iso-curves of vorticity field showing instability of the shear layer occurring from a flat-plate. Adapted image from the numerical analysis of Luchini and Tognaccini [90]. (e) Vorticity rejected in the trailing jet from the pinched-off vortex ring and results in the formation of secondary structures, akin to KH instability. Image taken from Gharib et al. [49].

imposing as boundary conditions the continuity of pressure and the equality of the normal velocity on the disturbed sheet, we get:

$$\ddot{\varepsilon} + \dot{\varepsilon} \left(\frac{2\dot{R}}{R} + \frac{is\Gamma}{2\pi R^2} \right) + \varepsilon \left(\frac{\ddot{R}}{R} - \frac{s(s-1)\Gamma^2}{8\pi^2 R^4} \right) = 0 \quad (2.89)$$

The vortex sheet is stable if all solutions of Equation (2.89) that are bounded at $t = 0$, remain bounded as $t \rightarrow \infty$. However, the solution of Equation (2.89) can not be analytically found for a general $R(t)$ and $s \neq 2$, but a solution can be determined for the special case:

$$R(t) = R_0(at + 1)^m \quad (2.90)$$

where R_0 is the initial radius of the circular sheet, a and m arbitrary constants. The interesting solutions are for $s > 2$ because when $s = 1$ the vortex sheet suffers a rigid displacement and $s = 2$ is a trivial solution because the vortex sheet deforms into an ellipse. If all solutions of Equation (2.89) have to remain bounded, Moore and Griffith-Jones [96]'s analysis lead to the criterion that the expanding vortex sheet is stable if $m \geq 1$ and unstable otherwise. The limit case in which the behaviour of the instability changes is at $m = 1/2$. When $m < 1/2$, the disturbances grow exponentially as in Kelvin-Helmholtz instability that corresponds to $m = 0$. For $1/2 < m < 1$, the disturbances grow weakly and independently of the wavelength. For a general $R(t)$ and $s \gg 1$, a Wentzel-Kramers-Brillouin (WKB) expansion is applied and results are consistent with the criterion obtained from a circular vortex sheet [96].

2.5.2 Other examples of instability

The Kelvin-Helmholtz instability is one example of instability and definitely the most interesting to discuss for the objectives of the present work. However, we can find other examples of flow instability.

The Rayleigh-Taylor (RT) instability [129] is an instability that occurs at the interface of two fluids with different densities. When a heavier fluid is above a lighter fluid, the interface progressively becomes unstable under gravity. Examples in nature are water suspended above oil, mushroom clouds from volcano explosions or even more catastrophic events, such as supernova explosions in which the expanding gas core accelerates inside a denser shell. If the two fluids at different densities are impulsively accelerated, we have the Richtmyer-Meshkov (RMI) instability [115, 91]. It normally appears when a shock wave interacts with the material interface separating the two different fluids. For both RT and RMI instabilities, the interface can be modelled as an unstable vortex sheet of varying strength which induces the occurrence of vortices in a process similar to Kelvin-Helmholtz instability [148].

Finally, an instability that is noteworthy and closer with the physical concepts and

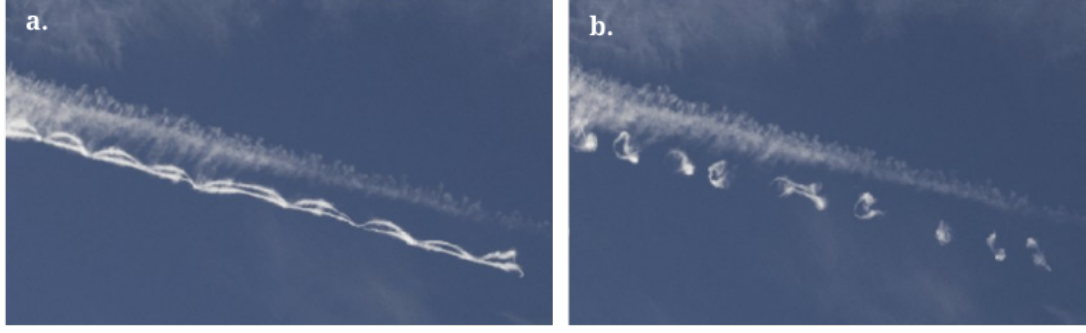


Figure 2.11: (a) Interaction between two airplane contrails whose instability leads to the formation of (b) a chain of vortex rings.

results discussed in the present work is the Crow instability.

Crow instability

The Crow instability, originally described by S. C. Crow [122], is a long wave three-dimensional instability that occurs from the interaction of a pair of counter-rotating vortices. An example is observed in the wake of large aircraft due to the interaction between wingtip vortices and contrails from the engine. The result is a distortion in the shape of the contrail (Figure 2.11a).

If we consider two counter-rotating vortex filaments with radius a and circulation $\pm\Gamma$ placed at a distance h and we put a small disturbance with axial wavenumber k on both filaments, the displacement \mathbf{x} of the disturbed vortices have equation:

$$\mathbf{x}(\xi, t) = \mathbf{x}_{si}(\xi, t) + \mathbf{x}_{mi}(\xi, t) \quad (2.91)$$

where ξ is a Lagrangian parameter increasing along each vortex. Depending on the nature of the initial disturbance, the two filaments are distorted in symmetric or anti-symmetric modes through the mutual interaction between the two filaments $\mathbf{x}_{mi}(\xi, t)$ and the self-induction of the single filament $\mathbf{x}_{si}(\xi, t)$. The distortions progressively grow proportional to $e^{\sigma t}$. Stability analysis shows that antisymmetric modes are stable. For the symmetric modes, the configuration is stable if σ is purely imaginary. For low values of kh and high values of a/h the configuration is unstable and there is a favoured wavelength for which the growth rate is maximum. The instability makes the two filaments physically interact and reconnect into a chain of vortex rings, as shown in Figure 2.11b. See also Saffman [125] and Leweke et al. [86] for a more detailed analysis.

2.5.3 Occurrence of secondary vortices

The instability of the shear layer grows and eventually gives rise to the formation of secondary vortices. The term secondary vortices refers to coherent vortical structures

formed after the primary vortex. In the way it is formulated, the definition of secondary vortices is not univocal because it includes all coherent structures formed after the primary vortex without taking into account the specific formation mechanism. In the previous section, we discussed the occurrence of secondary vortices from an unstable shear layer. However, reported studies in literature deal with secondary vortices that do not arise from an unstable shear layer.

Kissing et al. [72] define secondary vortices as opposite sign vortices that appear at the surface of a plunging and pitching airfoil. The motion of the airfoil leads to the formation of a primary vortex at the leading edge and the growth of the primary vortex induces opposite sign vorticity on the surface of the airfoil. This opposite sign vorticity grows between the primary vortex and the leading edge and becomes a secondary vortex. The growth of the secondary vortex interrupts the shear layer to feed the primary vortex. A third vortex is formed between the leading edge shear layer and the secondary vortex. These two structures are called secondary vortices and they are responsible for the primary vortex separation. A similar outline is also observed by Wojcik and Buchholz [143], in which secondary vorticity is generated at the surface of a pitching blade.

The formation of opposite sign vorticity between the primary vortex and a solid surface also happens when a primary vortex is pushed down towards an horizontal ground plane [62, 86]. The flow underneath the primary vortex induces opposite sign vorticity on the ground plane and the bounded vorticity separates to form one or more discrete secondary vortices that orbit the primary vortex. These secondary vortices have a weaker strength than the primary vortex and induce the primary vortex to rebound from the surface. Harris and Williamson [62] found that the strength of secondary vortices generated as a result of a ground effect with the approaching primary vortex linearly increases with the Reynolds number. They compare the strength of primary and secondary vortices and they showed that for $Re > 3000$ the ratio between the two strengths is Re independent.

A different formation mechanism is the one investigated in the present work and showed in [43]. When a flat plate rotates around its mid-chord, the separation of the primary vortex is followed by the shedding of several secondary vortices (Figure 2.12). The flow topology is similar to the pattern observed in Figure 2.10b-d, but there is a substantial difference. Secondary vortices generated from the rotating plate do not arise from an unstable shear layer but they are instead discretely released from the tip of the plate. The same evidence is also noted in the experiments of Corkery et al. [19], who studied the case of a rotating plate, and de Guyon and Mulleners [26], who observed smaller secondary vortices discretely detaching from a translating cone. The difference in the formation mechanism draws our attention and represents an additional motivation to study the configuration of a rotating flat plate.

We observed several formation mechanisms with which secondary vortices are generated. The frequency at which secondary vortices are released in the flow is also not unique. This is particularly evident when we look at shedding frequency of secondary vortices generated in the near wake of a circular cylinder [139]. These secondary vortices are oriented in the stream-wise direction, perpendicular to the primary Karman vortex that is oriented in the span-wise direction [13]. This phenomenon was previously called transition waves by Bloor [11]. The typical shear layer frequency in the wakes of cylinders is much higher than the frequency of the von Karman vortex street. A consensus about the exact relationship between the frequency of the primary vortex shedding f_k and the secondary vortices f_{sl} has not yet been found. Bloor [11] observed that the ratio between the characteristic frequencies varies with Reynolds number according to $f_k/f_{sl} = Re^{1/2}$. However, there is no consensus about the exponent value of the proposed relationship. Prasad and Williamson [110] indicated that an exponent value of 0.67 works for Re up to 10^5 and Wei and Smith [139] found 0.87 in the range from $Re = 1200$ to $11\,000$.

No clear relationships are established in the situation of an isolated primary vortex. Based on the flow visualisation around a submerged flat plate, Grift et al. [57] determined the shedding frequency of secondary vortices to lie in the range from 13 Hz to 20 Hz, for different values of acceleration, velocity, and immersion depth. This range corresponds to a Strouhal number around 0.2, according to the plate geometry and kinematics used by the authors. The secondary vortex shedding frequency behind a vertical flat plate increases with increasing acceleration of the flat plate according to Rosi and Rival [120].

What emerged from the reported studies is that the flow configuration affects the formation mechanism with which secondary vortices are generated. Moreover, there is not a clear consensus about the shedding frequency of secondary vortices. It is crucial to define a scaling parameter, such as the Strouhal frequency for the cylinder case, that allows for a more universal relationship between the shedding frequency or formation time of primary and secondary vortices as a function of the Reynolds number. Finally, we found only few studies that compute the strength of secondary vortices and none of them discuss in details the difference between primary and secondary vortices.

2.6 Three dimensional effects

The previous sections mainly deal with two-dimensional flows in which it is supposed that the out-of-plane velocity component is either a constant or zero. As observed by Auerbach [4], vortices generated by an impulsively started flow about a sharp edge and bounded by two sides are not influenced in the mid-plane by these two sides for a time. For this reason, measurements are carried out in the mid-plane (halfway between the

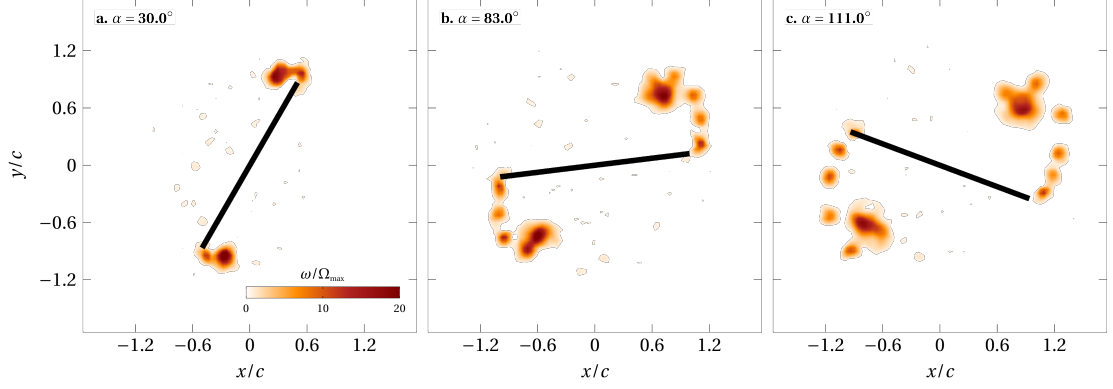


Figure 2.12: Snapshots of the vorticity field around a rotating plate for three angular positions. After the primary vortex formation at approximately 30° , several secondary vortices are discretely released from the plate tip. Negative vorticity around the plate has been removed for sake of clarity.

two sides) such that the out-of-plane velocity is negligible and the flow can be treated as two-dimensional. However, there are plenty of cases in which the three-dimensionality of the flow cannot be neglected. A pair of straight parallel vortices represents an elementary vortex configurations, whose study is motivated by its relevance to the problem of aircraft trailing wakes. Despite the conceptual simplicity, vortex pairs exhibit a variety of complex behaviours, ranging from two-dimensional dynamics, such as merging and rotation, to three-dimensional instabilities [86, 142]. The simultaneous growth of two distinct instabilities on a vortex pair leads to the formation of a chain of vortex rings, known as Crown instability (Figure 2.11).

An extensive review about the three-dimensional variation of the wake detaching from bluff bodies, such as spheres or cylinders, is made by Thompson et al. [136]. The shape of the wake depends on the motion of the body and on the presence of a nearby wall. In the case of a translating cylinder away from a solid wall, the wake exhibits three-dimensional instabilities with increasing Reynolds number. Below the Reynolds number of $Re \approx 46$, the wake appears as a periodic two-dimensional von Karman wake. When Re is above 200, the wake undergoes a sinusoidal span-wise distortion with a wavelength that is approximately four times the cylinder diameter. This wake is referred as *Mode A*. A further increase of Re above 260 reduces the span-wise wavelength to approximately one cylinder diameter and we have the *Mode B* wake. When the cylinder rotates and translates, the wake is not symmetric and the transition behaviour changes compared to the pure translating case. For ratios between the rotation and translation speeds smaller than 2, the transition to *Mode A* and *Mode B* is only shifted to slightly higher Reynolds number. For ratios higher than 2, the flow topology is significantly altered and we observe a single-sided vortex shedding. The proximity of a wall to the cylinder suppresses the passage of fluid underneath the cylinder. This also results in single-sided shed vortices that induce secondary wall vorticity, which rolls-up into weaker vortex structures and interact with the primary vortices to form the wake. If the

cylinder translates and rotates close to the wall, the magnitude of the secondary wall vorticity increases and induces an earlier development of the wake instability. In this scenario three-dimensional effects become predominant.

Bluff bodies are not the only example in which three-dimensional instabilities are observed. Vortices generated from straight sharp edges of plates, wedges or nozzles can also manifest sign of 3D instability. The influence of three-dimensional effects for a flat plate rotating around its edge is investigated by Leweke [85] and is interesting for the purpose of the present work. The rotation of the plate generates a vortex that expands in the span-wise direction and at mid-span the vortex is axisymmetric with no influence of the out-of-plane velocity. The perturbation that comes from the bottom of the plate, propagates along the span and induces a strong axial velocity along the vortex tube. As a result, the vorticity in the core becomes less concentrated, the vortex loses its axisymmetry and subsequently splits into smaller vortices. Leweke [85] quantitatively analysed the axial velocity induced by the perturbation along the vortex and identified two different regions of the flow. The first region corresponds to the early stage and there is no axial velocity. The second and late stage starts when the perturbation arrives at the mid-span, inducing an axial velocity that jeopardizes the symmetry of the vortex. The boundary between this two regions depends on the velocity of the perturbation that propagates along the vortex, which is proportional to the Reynolds number. In [chapter 3](#) we apply the results found in [85] about the perturbation velocity along the vortex to estimate the influence of three-dimensional effects in the present work.

2.7 Summary and objectives of the research

In this chapter we presented a detailed theoretical background about the formation of vortices. We started by defining the shear layer and its inviscid approximation referred to as vortex sheet. The self-induced velocity of vortex sheets is described by the Birkhoff-Rott equation and self similar solutions of this equation lead to several mathematical models of the spiralling roll-up of the shear layer. We first introduced the logarithmic spiral that describes the roll-up of the shear layer behind the trailing edge of moving airfoils, as observed and studied by Prandtl [109]. Following the work of Pullin [111], we moved to the spiral solution that describes how an accelerated flow past a wedge rolls-up and we reported the limit case of a zero wedge angle that corresponds to the flow past a flat plate. Particular attention was given to the roll-up of a semi-infinite vortex sheet whose roll-up is described by Kaden's spiral. The equation of Kaden's spiral will be used and adapted for the analysis presented in [chapter 4](#). The roll-up of the shear layer gives rise to the formation of a primary coherent vortex. We reviewed the growth process of the primary vortex for three different flow configurations and we highlighted the limiting process of the vortex growth. The primary vortex can not grow endlessly and Dabiri [20] hypothesized the existence of a unique vortex formation

number marking the primary vortex pinch-off in various flow configurations. The separation of the primary vortex often coincides with a growing instability of the shear layer that results in the occurrence of secondary coherent structures. These secondary structures are referred to as secondary vortices because they are generated after the primary vortex formation. The instability of the shear layer is not the only mechanism that leads to the generation of secondary vortices. Secondary structures also form from the interaction between the leading edge vortex and the surface of the airfoil, in ground effect when a vortex approaches the wall, or they are discretely released from the tip of a plate. Finally, the majority of the reported studies deal with two-dimensional flows and in the last section of the chapter we discussed the three-dimensionality of vortices.

The extensive review about the formation and growth of a primary vortex followed by the occurrence of several secondary structures has prompted us to ask what is the main difference between primary and secondary vortices. We know that the primary vortex growth has a limit but it is still not clear how the maximum strength and the pinch-off depend on the flow conditions or if a unifying principle can be applied. The occurrence of secondary vortices happens as a result of an unstable shear layer, but this is not the only formation mechanism. We wonder how the driving mechanism behind the formation of secondary vortices depends on the flow configuration. Finally, there is no consensus about a specific frequency range inside which secondary vortices are released from the different flow configurations. We also did not find experimental or numerical studies in which the strength of secondary vortices is computed.

These unsolved aspects and the role of vortex formation on lift and thrust production motivate us to analyse primary and secondary vortices behind a rotating plate. The first objective of the thesis is to characterize the growth process of the primary vortex as a function of the plate kinematics. This requires the definition of a dimensionless convective time that helps us to identify the pinch-off time among different experiments. We also want to determine the maximum limit strength reached when the primary vortex pinches-off and find the relationship between the plate kinematics and the primary vortex limit strength and pinch-off. The determination of the primary vortex limit strength and pinch-off is crucial to define a vortex formation number that works for all the tested cases. The second objective we want to address is the identification of the trajectory followed by primary and secondary vortices. This aspect is relevant in engineering applications because we observed in literature how the progressive drifting of vortices away from wings or airfoils coincides with a loss of aerodynamic performance. The third objective is to compute the timing and the strength of secondary vortices and check how the plate kinematics influence the development of secondary vortices. A study about the exact determination of the strength of secondary vortices is missing. We believe that a better understanding about the occurrence and shedding of secondary vortices might lead us to get additional information about the formation of the primary vortex. Last but not least, we want to combine all of these information to be able to predict the growth, the timing and the trajectory of primary and secondary

Chapter 2. Theoretical background

vortices. This will help us to get closer to the reason why primary and secondary vortices are different and have a better insight into the comprehension of vortex formation.

Chapter 3

Experimental measurements and analysis

The present thesis is an experimental work and in the current chapter we report and show how data are obtained and analysed. Firstly, an overview about the experimental set-up is given. This includes a detailed description of the rotation mechanism used to make a rectangular flat plate rotate around its mid-chord in quiescent water. The specific geometry and the kinematics of all the tested flat plates are also discussed.

Secondly, we described the entire optical set-up used to record particle image velocimetry (PIV) images from which we obtain quantitative velocity fields of the flow around the rotating plate. An entire section is dedicated to the impact of the camera resolution on the recorded images.

Finally, we present results from the experimental data and we discuss how the main flow parameters of the generated vortices, such as vorticity, circulation and size are computed.

3.1 The rotation mechanism

A schematic representation of the rotation mechanism is shown in [Figure 3.1](#). The mechanism is fastened to an outer aluminium frame through the supporting base. This allows us to finely adjust the position of the mechanism such that the mid span of the plate is at the desired measurement plane. The rotation kinematic input is given by a servo motor (Maxon RE 35) connected to a stainless steel shaft and transferred to the flat plate through a 1 : 1 conical coupling. A 1 : 19 gearbox is mounted on the motor to ensure high torque, speed, and acceleration. The rotational angle, speed, and acceleration are controlled via a Galil DMC-4040 motion controller, which allows for

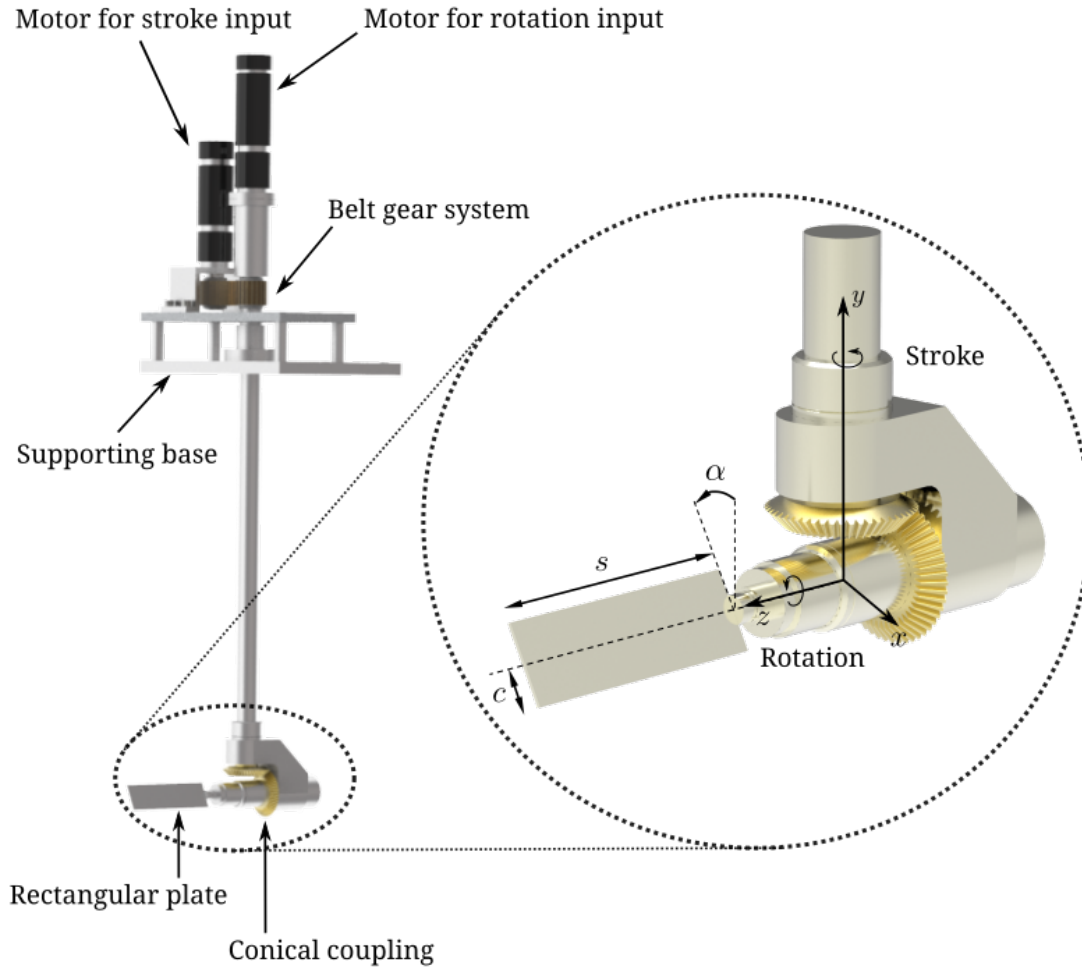


Figure 3.1: A schematic representation of the rotation mechanism used to rotate the plate model. The inlay shows a zoomed in section of the rectangular plate coupled to the shaft through a 1 : 1 conical gear. The servo motor makes a rectangular plate of span s , tip-to-centre length c and thickness t rotate about the z axis to an angle α . The stroke motion around the y axis is also possible with a second servo motor connected to the main shaft through a belt gear system, but this is not used here.

accurate control of arbitrary motion profiles. This mechanism is very reliable and robust and experiments show an error of less than 0.1° between the motor input signal and the motor output signal measured by the encoder through the entire plate rotation [48]. Motions are conducted with a high level of repeatability.

A second servo motor of the same type is mounted on top of the supporting base to allow the plate to also perform the stroke motion. The motion is transferred from the servo motor to the main shaft through a belt gear system. In this way, the plate can also stroke around the y axis (Figure 3.1). The combination of the stroke and the rotation about the z axis results in the flapping motion of the plate, similar to the mechanism used by insects to fly. The flapping motion is outside the scope of the present work but it is noteworthy because it shows the potential of our mechanism in the study of

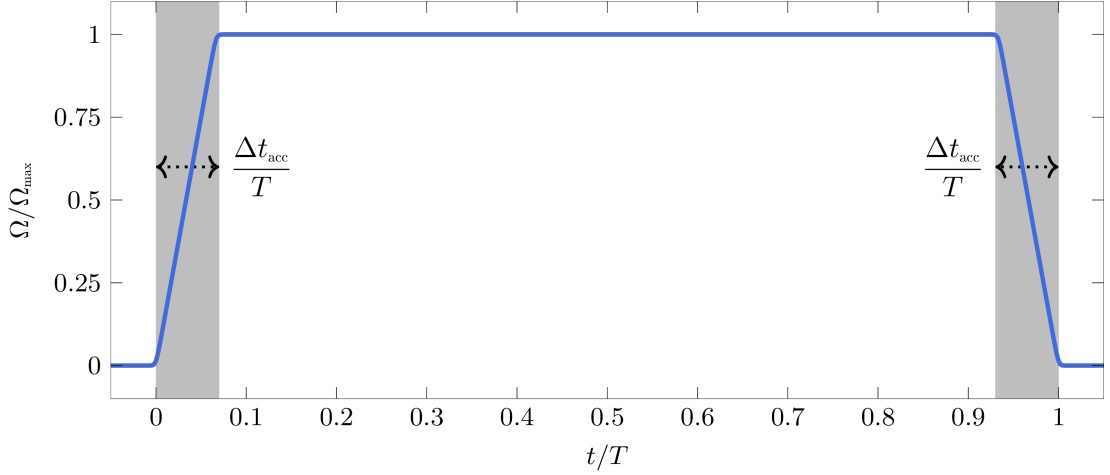


Figure 3.2: Trapezoidal velocity profile as a function of the dimensionless time t/T . The grey shaded regions indicate the portion of the motion during which the plate is accelerated.

vortices generated through more complex and advanced kinematic inputs.

3.1.1 Plate geometry and kinematics

The rotation mechanism allows the plate to rotate about the z axis with an angle α following a prescribed kinematics (Figure 3.1). In this thesis, we consider a trapezoidal rotational velocity profile and a fixed rotational amplitude of $\alpha = 180^\circ$, as schematically presented in Figure 3.2. To ensure a continuous acceleration profile, the corners of the velocity trapezoid are smoothed according to the Eldredge smoothing function [31]:

$$\dot{\alpha}(t/T) = \frac{k}{a} \ln \left[\frac{\cosh(at/T) \cosh(a(t/T - a))}{\cosh(a(t/T - \Delta t_{\text{acc}}/T)) \cosh(a(t/T - 1 + \Delta t_{\text{acc}}/T))} \right] \quad (3.1)$$

with T the time duration of the motion, a the corner smoothing parameter, Δt_{acc} the duration of the acceleration, and k the parameter related to the maximum velocity Ω_{max} . The grey areas in Figure 4.1b are the regions during which the plate is accelerated and the added mass effects take place. During the experiments, the corner smoothing parameter and the rotational acceleration are kept constant to 100 and 6000°s^{-2} , respectively. The influence of the plate kinematics into the formation of vortices is studied by varying the maximum rotational speed of the plate Ω_{max} from 30°s^{-1} to 400°s^{-1} .

Regarding the geometry of the plate, we select a rectangular shape whose dimensions are the span s , the length l and the thickness h . We refer here to the chord of the plate c as the distance between the rotation point and the tip of the plate (Figure 3.1). The value of the plate tip speed depends on the position of the rotation point and we find the chord c to be a better characteristic length scale than the entire length l of the plate. The span s is kept constant among all the different tested cases, but we vary the chord c

and the thickness h .

The first series of experiments is conducted with a rectangular glass flat plate, with length $l = 8$ cm, span $s = 16$ cm and thickness $h = 2$ mm. The rotation point is placed at mid-length, which gives a chord $c = 4$ cm. For this series of experiments, vortices are formed symmetrically behind both ends of the plate. The second series of measurements has the aim to evaluate the mutual influence between vortices generated from the two sides of the plate. For this purpose, the length of the plate is reduced to $l = 4$ cm and the rotation point is shifted to the edge of the plate. As a consequence, the chord length c is preserved to 4 cm and vortices are formed only on one end of the plate. This allows us to study the influence of the rotation point and detect potential interferences caused by symmetric vortex release on both tips when the rotation point is at mid-length. A third set of measurements with a longer plate with length $l = 12$ cm and the rotation point at mid-length, yielding a chord length of $c = 6$ cm, was conducted to provide insight into the influence of the chord length on the vortex formation.

Finally, the fourth and last set of measurements are taken with a thicker plate of thickness $h = 4$ mm. The length l is reduced to 8 cm and the rotation point is kept at mid-length such that $c = 4$ cm, as it was for the first series of measurements. The thickness is increased from 2 mm to 4 mm with the objective of defining the role of the thickness on the vortex formation. All the flat plates with 2 mm thickness are made out of glass. The glass makes the plate stiff enough to not bend due to the interaction with water and its transparency prevents shadow regions when performing particle image velocimetry (PIV). When the thickness of the plate is increased to 4 mm, the glass becomes more complicated to easily cut. For this reason the chosen material for the 4 mm tested plate is laser cut PMMA that turns out to be rigid enough to not deform in water. PMMA is not as transparent as glass, but placing LEDs on both sides of the plate removes all the shadow regions.

3.1.2 Scaling parameters

After we have presented and discussed the motion kinematics and the geometry of the plate, we need to identify non-dimensional scaling parameters. In the present thesis, we use three non-dimensional variables to describe a rotating rectangular plate with varying speed and dimensions. The first one is the Reynolds number Re , defined as follows:

$$Re = \frac{u_{max}c}{\nu} = \frac{\Omega_{max}c^2}{\nu} \quad (3.2)$$

where $u_{max} = \Omega_{max}c$ is the maximum tip speed of the plate, c is the distance between the rotation point and the tip of the plate (referred in the thesis as the plate chord) and $\nu = 10^{-6} \text{m}^2 \text{s}^{-1}$ is the kinematic viscosity of the water at 20 °C. The maximum rotation speed of the plate Ω_{max} varies from 30°s^{-1} to 400°s^{-1} and leads to a Reynolds number

$Re = (\Omega_{\max} c^2)/\nu$ ranging from 840 to 11 150. All the measurements mentioned in this thesis are in this range of Reynolds number.

The second parameter we need to define is a convective or dimensionless time variable t^* . The dimensional time t is given by the ratio between the travelled arc length $l = \alpha c$ and the tip speed of the plate $u_{tip} = \Omega c$. If we scale the dimensional time t with respect to the rotational speed of the plate, we have:

$$t^* = \Omega \frac{l}{u_{tip}} = \alpha \quad (3.3)$$

It follows that the angular position of the plate serves as the dimensionless time variable.

Finally, the third and last parameter is a dimensionless time scaled with respect to the plate thickness h :

$$T^* = \frac{\alpha c}{h} \quad (3.4)$$

We can describe this dimensionless time as the number of thicknesses h that the plate travels along the arc length $l = \alpha c$. The importance of this alternative convective time will be further discussed in [chapter 5](#).

3.2 Particle image velocimetry

Quantitative information of the flow field around the plate is obtained using particle image velocimetry (PIV), which is easy to use, robust and non-intrusive nature. We mount the rotation mechanism on top of an octagonal tank. The tank is filled with water and has an outer diameter of 0.75 m, which is big enough to prevent wall boundary interference effects on the rotating plate. The exact position of the rotation mechanism is chosen such that the flat plate is exactly at the centre of the tank. In this way, we are sure to avoid wall and surface effects on the formation of vortices. The flow is homogeneously seeded with polystyrene particles that are small enough ($\approx 60 \mu\text{m}$) to follow the fluid. The measurement plane is illuminated with two LEDs as the light source and a camera is used to record and track the motion of the illuminated particles. The camera and the two light sources are at a fixed position around the tank ([Figure 3.3](#)).

During all our experiments, we first make sure that the plate starts the rotation when the chord is oriented in the vertical direction. The camera, the LEDs and the rotation mechanism are synchronised by means of a voltage trigger signal that is programmed to turn the LEDs on and make the camera record images as soon as the plate motion starts. With the help of the feedback from the motor encoder, the position of the plate is monitored and the image recording stops when the plate has travelled 180° . With this procedure, we can easily link every recorded snapshot to the corresponding angular

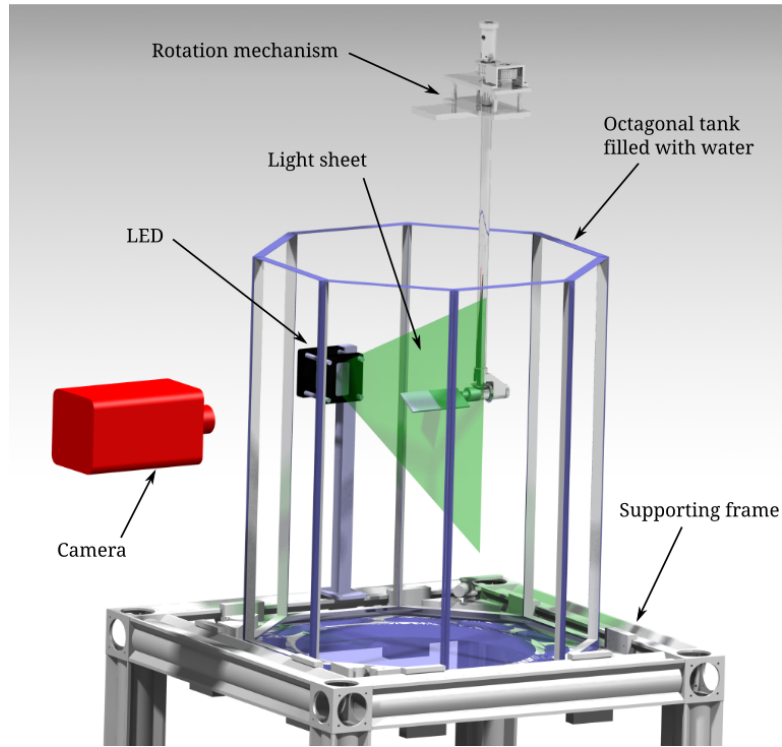


Figure 3.3: Rendering of the optical experimental set-up used to take PIV images. For sake of clarity, the optical set-up is shown with the LED only on one side of the tank.

position of the plate. In the next part of this section, we discuss in detail the different components used to record PIV images.

Seeding particles

Polyamide 12 fine powder (VESTOSINT 2157 natural color, from EVONIK Industries) is used in the current experiment as the seeding agent. These particles have a spherical shape of diameter $56\text{ }\mu\text{m}$, a refractive index of 1.5 and a density of 1.016 g cm^{-3} . The amount of particles that are put in water should guarantee a homogeneous distribution over the entire volume. If the particle density is low, the PIV cross-correlation algorithm fails to properly compute the velocity flow field in the whole region. On the contrary, if the density is too high, the correlation algorithm does not distinguish a particle from the other. This will lead to gaps in the evaluated velocity field. The density of Polyamide 12 is very close to water density and particles remain suspended in water and follow the flow. After a few hours of inactivity, these particles start to aggregate and settle at the bottom of the tank. This situation requires the flow to be stirred before starting experiments. After stirring the flow, particles need at least 10 min to return in a quiescent state and have a brownian motion.

Light source

Seeding particles in the fluid need to be illuminated with a high intensity light source. Two high-power pulsed light-emitting diodes (LED Pulsed System, ILA 5150 GmbH) are

used to create a light sheet with sufficient light intensity in the measurement plane. The LEDs emit a wavelength around 530 nm that corresponds to a green light. Compared to lasers that are the most used source of light in PIV, LEDs have a wider spectral width of up to tens of nanometers and a short coherence length of $O(10 \text{ } \mu\text{m})$. As a consequence, speckle effects do not affect LEDs light sources [114]. In addition, LED based illumination is easier to set-up, safer and cheaper than lasers. The experimental applicability of high-power LED for PIV has been demonstrated previously by [15, 140, 76]. LEDs are placed on both sides of the plate to reduce shadow regions. Cylindrical lenses are installed to create light sheets of equal intensity and are properly aligned to illuminate the particles in the flow from opposite directions in the same plane. The two light sheets from opposite ends overlapped at the mid-span of the plate where the images were captured. The thickness of the light sheet was approximately 5 mm.

Cameras

We use two different cameras during our experiments: a FASTCAM SA-X2 high speed camera and a PIV sCMOS camera made by ILA 5150 GmbH. The high speed camera allows to record time-resolved images at a lower resolution and the sCMOS gives us phase-averaged images at higher resolution. The combination of both set of measurements is crucial for an in-depth analysis of vortex formation.

3.2.1 Time-resolved measurements

Time-resolved PIV images are obtained with a FASTCAM SA-X2 high speed camera. The camera is equipped with a 35 mm Canon lens and the camera is aligned carefully such that the optical axis of the lens is aligned with the rotational axis of the plate and is perpendicular to the light sheet (Figure 3.3). The frame rate and the exposure time are varied, depending on the dynamics of the motion. A frame rate and exposure time of 250 Hz and 1 ms are selected for the lowest tested speed. These values are 2000 Hz and 0.5 ms for the highest tested speeds. The frame rate is high enough to capture the dynamics of the motion and the LED is set to continuous mode. The camera resolution is $1024 \text{ px} \times 1024 \text{ px}$, which corresponds to a field of view of $20 \text{ cm} \times 20 \text{ cm}$. The raw data are processed by the commercial software PIVview (PIVTEC GmbH, ILA 5150 GmbH) using a correlation model based on minimum squared differences and a multi-pass interrogation algorithm with three iterations. The final interrogation window size is $32 \text{ px} \times 32 \text{ px}$ with an overlap of 68 %. A third order B-spline interpolation method for sub-pixel image shifting is performed on all passes. The resulting physical resolution is 1 mm, or $0.025c$ with $c = 4 \text{ cm}$.

3.2.2 Phase-averaged measurements

Phase-averaged images are recorded with a PIV sCMOS camera (ILA 5150 GmbH). The sCMOS camera has a resolution of $2560 \text{ px} \times 2160 \text{ px}$ with a maximum frame rate of 100 Hz. This frame rate is too low to capture the whole dynamics at the investigated speeds and accelerations. The LEDs are set in pulsed mode with a fixed pulse width of $500 \text{ }\mu\text{s}$ and pair of snapshots with the plate at 90° are taken. The time interval between the two pulses is varied from $1500 \text{ }\mu\text{s}$ to $12\,000 \text{ }\mu\text{s}$, based on the plate speed, and a $600 \text{ }\mu\text{s}$ camera exposure time is chosen. The raw data are processed with a correlation mode based on squared difference and a multi-grid algorithm with image deformation with three iterations. The final interrogation window size is $24 \text{ px} \times 24 \text{ px}$ with an overlap of 65%. A third order B-spline interpolation method for sub-pixel image shifting is performed on all passes. The resulting physical resolution is 0.5 mm , or $0.0125c$ with $c = 4 \text{ cm}$, and is double the spatial resolution obtained from processing time-resolved data.

3.3 Velocity and vorticity fields from PIV data

The processing of PIV images gives direct information about the velocity field. The outcome of our processed PIV images is a planar velocity field that can be used to estimate other significant fluid mechanical quantities. For our purpose, the vorticity field is the most important differential quantity to compute and, unlike the velocity, is Galilean invariant. The Navier-Stokes equation itself can be rewritten to give the vorticity equation:

$$\frac{\partial \boldsymbol{\omega}}{\partial t} + \mathbf{u} \cdot \nabla \boldsymbol{\omega} = \boldsymbol{\omega} \cdot \nabla \mathbf{u} + \nu \nabla^2 \boldsymbol{\omega} \quad (3.5)$$

which has the advantage of having eliminated the pressure term.

Planar PIV provides only two velocity field components and excludes the possibility to fully compute differential quantities. If we consider $\mathbf{x} = (x, y, z)$ to be the space vector and $\mathbf{u} = (u, v, w)$, $\boldsymbol{\omega} = (\omega_x, \omega_y, \omega_z)$ to be the three-dimensional velocity and vorticity vectors, the velocity gradient tensor:

$$\frac{d\mathbf{u}}{d\mathbf{x}} = \begin{bmatrix} \frac{\partial u}{\partial x} & \frac{\partial v}{\partial x} & \frac{\partial w}{\partial x} \\ \frac{\partial u}{\partial y} & \frac{\partial v}{\partial y} & \frac{\partial w}{\partial y} \\ \frac{\partial u}{\partial z} & \frac{\partial v}{\partial z} & \frac{\partial w}{\partial z} \end{bmatrix} \quad (3.6)$$

can be decomposed into a symmetric and antisymmetric part, which as a function of

the strain ε and vorticity ω components is:

$$\frac{d\mathbf{u}}{d\mathbf{x}} = \begin{bmatrix} \varepsilon_{xx} & \frac{1}{2}\varepsilon_{xy} & \frac{1}{2}\varepsilon_{xz} \\ \frac{1}{2}\varepsilon_{yx} & \varepsilon_{yy} & \frac{1}{2}\varepsilon_{yz} \\ \frac{1}{2}\varepsilon_{zx} & \frac{1}{2}\varepsilon_{zy} & \varepsilon_{zz} \end{bmatrix} + \begin{bmatrix} 0 & \frac{1}{2}\omega_z & -\frac{1}{2}\omega_x \\ -\frac{1}{2}\omega_z & 0 & \frac{1}{2}\omega_y \\ -\frac{1}{2}\omega_x & \frac{1}{2}\omega_y & 0 \end{bmatrix} \quad (3.7)$$

The first matrix of the right-hand side of the above equation represents the strain tensor, in which the diagonal components are the elongation strains and off-diagonal elements are the shearing strains. The second matrix is the antisymmetric part of the velocity gradient tensor and contains vorticity components.

Given that 2C PIV provides only u and v velocity components, which can be differentiated only in the x and y directions, the only components of the velocity gradient tensor that we can measure are:

$$\begin{aligned} \omega_z(x, y) &= \frac{\partial v}{\partial x}(x, y) - \frac{\partial u}{\partial y}(x, y) \\ \varepsilon_{xy}(x, y) &= \frac{\partial u}{\partial y}(x, y) + \frac{\partial v}{\partial x}(x, y) \\ \varepsilon_{xx}(x, y) + \varepsilon_{yy}(x, y) &= \frac{\partial u}{\partial x}(x, y) + \frac{\partial v}{\partial y}(x, y) \end{aligned} \quad (3.8)$$

From our PIV images, we can only compute the vorticity component ω_z normal to the light sheet. We can also determine the in-plane shearing ε_{xy} and the extensional strains ε_{xx} and ε_{yy} , even though for our scope they are not as relevant as the vorticity component. Since we take measurements in an incompressible fluid such as water ($\nabla \cdot \mathbf{u}$), we can also estimate the out-of-plane strain from the third relationship of Equation (3.8):

$$\varepsilon_{zz} = \frac{\partial w}{\partial z} = -\frac{\partial u}{\partial x}(x, y) - \frac{\partial v}{\partial y}(x, y) \quad (3.9)$$

From the evaluation of out-of-plane strain we can not retrieve the out-of-plane velocity component w , which can be only estimated through stereo PIV. In the present work, the flow field evolution of vortices around a rotating plate is mostly shown through the vorticity component ω_z .

3.3.1 Flow field evolution in time

The computation of the vorticity field on time-resolved data, gives a qualitative and quantitative insight about the formation of vortices as the plate rotates. The velocity and vorticity fields for selected time instants during the full 180° rotation of the plate, accelerated from rest at $6000^\circ/\text{s}^2$ and with a maximum rotational speed of $300^\circ/\text{s}$, are shown in Figure 3.4. The corresponding Reynolds number is 8380. At the beginning and the end of the rotation, the wing's chord is oriented in the vertical direction. The plate is rotated clock wisely and the rotational angle α indicates the angle with respect to the

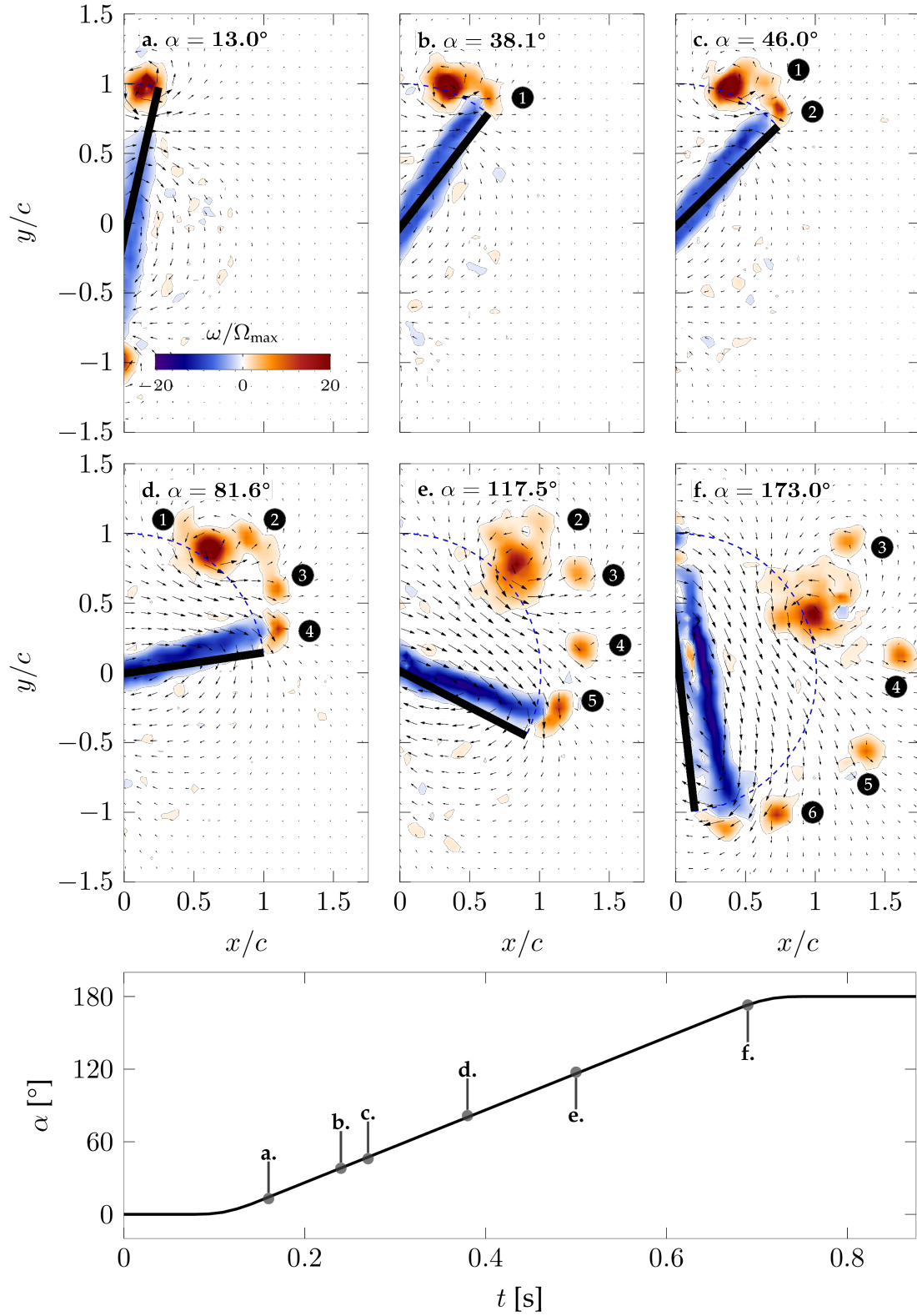


Figure 3.4: (a-f) Velocity and vorticity fields at several angular positions when the rotates at 300°s^{-1} . The dashed line represents the plate tip trajectory and six secondary vortices are shed after the primary vortex formation. Velocity vectors are plotted every 3 grid points. (bottom) Plate's angle α with respect to the vertical position as a function of time and dots correspond to (a-f) flow field snapshots.

initial vertical orientation of the wing. The vortex development and shedding for both tips is similar (Figure 2.12) and we focus here on the structures generated around the tip that was initially at the top. During the rotation, multiple counter-clockwise rotating vortices are formed at the tips of the plate and they are highlighted by a concentration of positive vorticity. Negative vorticity is associated with the flow region around the rotating plate.

At $\alpha = 13^\circ$, the acceleration phase is already ended and the plate rotates with the maximum rotational velocity of 300°s^{-1} (Figure 3.4 bottom). Fluid is accelerated around the tip creating a cloud of positive vorticity that rolls up into the primary vortex (Figure 3.4a). As the motion continues, the primary vortex further accumulates vorticity and grows in size until it pinches-off. When the pinch-off happens, the feeding process of the primary vortex from the shear layer is stopped and the primary vortex stops growing. As the plate keeps rotating after the primary vortex has stopped growing, vorticity continues to be generated and accumulates around the plate tip. At $\alpha = 38^\circ$, we observe the formation of the first secondary vortex (Figure 3.4b). The shedding of secondary vortices carries on until the rotation is finished. At 46° , the first secondary vortex has shed and convects around the primary vortex. In the meantime, the next secondary vortex is forming (Figure 3.4c). When the plate has travelled almost half of the rotation, four secondary vortices are clearly distinguished in the flow field. We also note that the first secondary vortex merged with the primary vortex and is no longer present in the flow field (Figure 3.4d). Merging also occurs to the second secondary vortex that is incorporated in the primary vortex and is no longer visible at 118° (Figure 3.4e). At this angular position, the fifth secondary vortex has already shed. The sixth and last secondary vortex separates from the tip when the plate has almost finished rotating. At 173° , only four out of six secondary vortices are observed in the flow field due to the merging of the first two secondary vortices with the primary vortex (Figure 3.4f).

From the simple visual observation of the velocity and vorticity fields, we highlight some noteworthy aspects. The primary vortex keeps following the plate tip trajectory, highlighted by a dashed line in Figure 3.4, during the full rotation. Secondary vortices are substantially smaller than the first one and they are very similar to each other, akin to Kelvin-Helmholtz instabilities. The first two secondary vortices tend to roll and merge into the primary vortex. The later shed secondary vortices follow the tip trajectory while they drift radially outwards. All the shed vortices seem to follow a spiralling trajectory that connects the plate tip to the primary vortex centre. We observed in total the formation of six secondary vortices. The first four form when the plate rotates from approximately 38° to 90° . The later two formed during the second half of the motion. This observation suggests that the timing of secondary vortices is not constant but increases as more vortices are released in the flow. These observations are further investigated in the next two chapters.

In Figure 3.4, the flow field snapshots are shown in the fixed reference of frame. In the

following, the flow field is presented in the plate's reference frame, for sake of simplicity.

3.3.2 Flow field with the plate at 90°

Time-resolved data capture the flow field around the plate during the entire rotation. However, time-resolved data are longer to process, heavier to store and the grid resolution can be improved. We combine time-resolved data with phase-averaged measurements to get higher resolution images of the flow field at a fixed angular position of 90°. Phase-averaged images allows us to check how the augmented grid resolution affects the computation of integral and differential physical flow quantities. Moreover, high resolution images at 90° provide a quick overview of the flow field as we vary the Reynolds number, i.e. the maximum speed of the plate.

A number of 15 pair of snapshots recorded at 90° are taken for each tested speed. This number is high enough to ensure repeatability of measurements. Even from a single snapshot the flow topology is well resolved. Comparison between a single snapshot and phase-averaged vorticity fields at $Re = 8380$ is shown in [Figure 3.5](#). We removed the negative vorticity around the rotating plate for a clearer view of the flow field. Four shed secondary vortices follow the primary vortex. The cloud of vorticity at the tip of the plate indicates the formation of the fifth secondary vortex. A shed secondary vortex whose centre is at $x/c = 0.57, y/c = 1$ orbits around the primary vortex and is about to merge ([Figure 3.5b](#)). This first secondary vortex is clearly distinguished from the primary vortex, while in [Figure 3.4d](#) the secondary vortex is already included in the primary vortex region. The higher resolution gives a more detailed view of the merging process. All the other qualitative details we get from simple flow visualization are well captured by time-resolved images. This means that the resolution of high-speed images is considered sufficient to highlight the topology of primary and secondary vortices formed from the tip of the plate.

If we increase the Reynolds number from 8380 to 11150 ([Figure 3.6a](#)), we observe the presence of three secondary vortices rather than four. A closer look to the right side of the primary vortex highlights a positive vorticity region that corresponds to the merging of the first secondary vortex. This means that the flow topology at higher Reynolds number does not show any substantial changes. If we reduce the Reynolds number to 1955 ([Figure 3.6b](#)), we do not observe the occurrence of clear and isolated secondary structures. We note instead a layer of fluid that connects the primary vortex to the tip of the plate. This layer of fluid presents some irregularities and is interrupted at certain locations, which can be interpreted as a sign of an unstable shear layer. If we further reduce the Reynolds number to 840 ([Figure 3.6c](#)), the shear layer now appears as a continuous layer of fluid that rolls-up into the primary vortex. In contrast with the irregular shear layer observed at 1955, the continuous layer of fluid represents a stable shear layer. From these observations, we identified the existence of three different flow

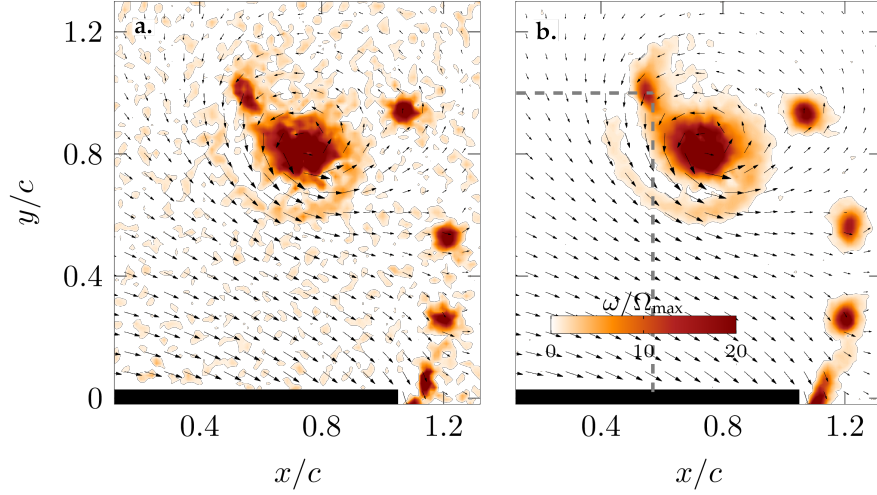


Figure 3.5: (a) Single snapshot of the velocity and the vorticity field compared with (b) their phase-averaged vorticity and velocity fields at $Re = 8380$. Velocity vectors are plotted every 5 grid points and negative vorticity is removed for a clearer view of the vortices. The dashed lines highlight the location of the secondary vortex merging with the primary vortex.

regimes depending on the Reynolds number. An in-depth analysis about the occurrence of these three different regimes is given in [chapter 4](#).

3.4 Identification of coherent structures

The tracking of the vortex growth requires us to properly identify the vortex region in the flow field that represents one of the biggest challenges in vortex dynamics. The complexity of defining a vortex justifies the introduction of multiple identification criteria and techniques. Most of them are Eulerian in nature and they exploit the instantaneous velocity field and its derivatives. They are faster and easier to compute but they present some disadvantages. Lagrangian methods, which take into account information along integrated particle trajectories, can be used to overcome some of the disadvantages of the Eulerian methods. Combination of both Eulerian and Lagrangian methods represents a powerful tool for an in-depth analysis into vortex formation.

3.4.1 Eulerian methods

Eulerian criteria are generally formulated in terms of the invariants of the velocity gradient tensor $\nabla \mathbf{u}$ [54]. The Q -criterion [66] defines a coherent vortex as the region where Q , the second invariant of $\nabla \mathbf{u}$, is higher than 0. The Δ -criterion [17] defines a vortex core as the region with complex eigenvalues of $\nabla \mathbf{u}$ where pathlines are locally closed [68] and the discriminant Δ is positive. The λ_2 criterion considers the presence

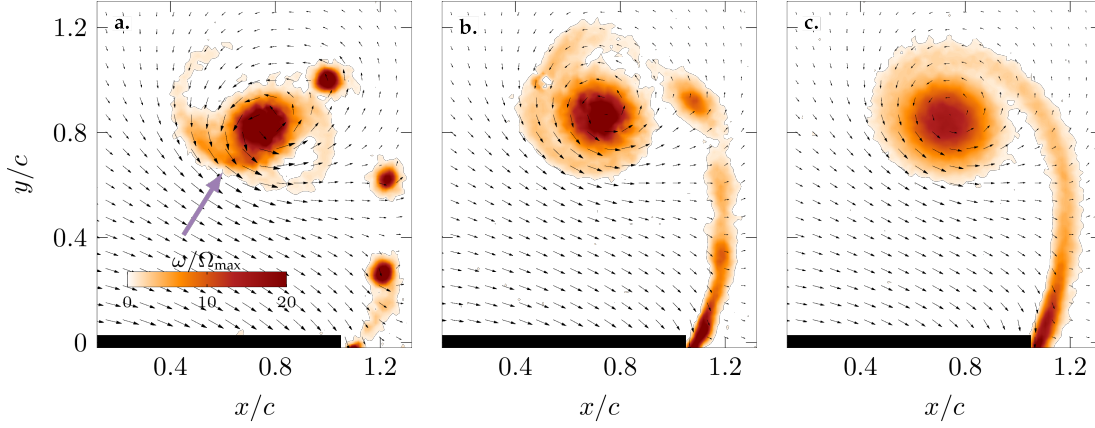


Figure 3.6: Velocity and vorticity fields at (a) $Re = 11150$, (b) $Re = 1955$ and (c) $Re = 840$. Velocity vectors are plotted every 5 grid points and negative vorticity is removed for a clearer view of the flow field. The arrow highlights the positive vorticity region that corresponds to the merging of the first secondary vortex for $Re = 11150$.

of a pressure minimum in the flow field. The occurrence of a local pressure minimum requires two negative eigenvalues of the velocity gradient tensor. Since the three eigenvalues are $\lambda_1 \leq \lambda_2 \leq \lambda_3$, the criterion defines a vortex as the region where λ_2 is negative [68]. Among all the Eulerian vortex identification methods, we have mostly used the swirling strength criterion and Γ criteria to identify vortex contours.

λ_{ci} criterion

The swirling criterion [147], detects a vortex core in the flow region where $\nabla \mathbf{u}$ has a complex pairs of eigenvalues. A scalar quantity λ_{ci} named as the swirling strength, is defined as the squared magnitude of the imaginary part of the complex eigenvalue. Giving a certain positive threshold to λ_{ci} , a coherent vortex is identified as the area where the swirling strength is higher than the selected value. Contours of primary and secondary vortices identified with the swirling strength criterion are shown in Figure 3.7a.

Γ_1 and Γ_2 criteria

The Eulerian criteria we mentioned above are gradient-based and they are strongly affected by small-scale turbulence. We describe here two criteria to identify the centre and the boundary of coherent vortices that considers only the flow topology and not its magnitude. The first method involves the definition of the following dimensionless scalar function Γ_1 [51], written here in the discrete form for PIV data:

$$\Gamma_1(P) = \frac{1}{N} \sum_S \frac{(\mathbf{PM} \times \mathbf{U}_M) \cdot \mathbf{z}}{\|\mathbf{PM}\| \cdot \|\mathbf{U}_M\|} = \frac{1}{N} \sum_S \sin \theta_M \quad (3.10)$$

The point M lies in a two dimensional domain S . The region S is centred around P and \mathbf{z} is a unit vector normal to the measurement plane. N represents the number of grid

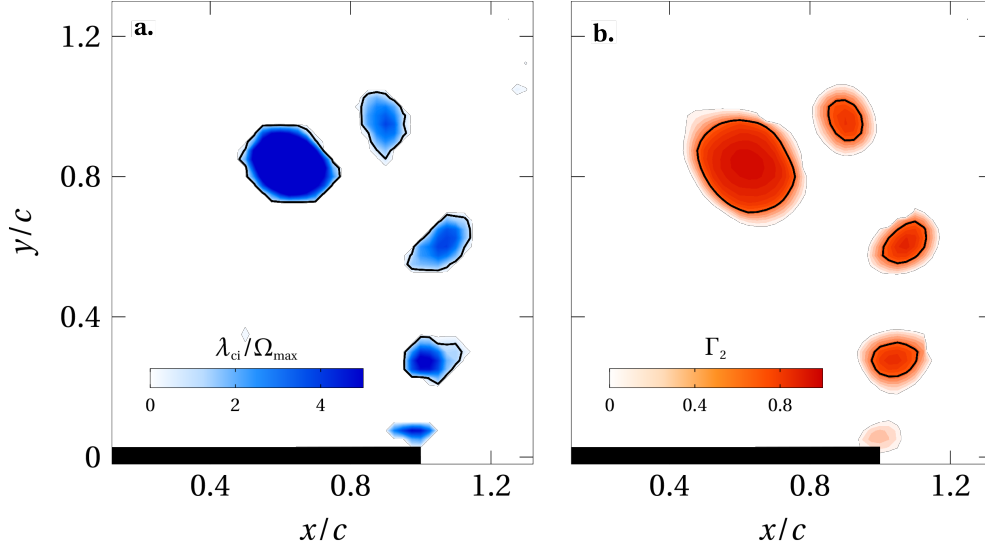


Figure 3.7: (a) Swirling strength λ_{ci} and (b) Γ_2 criteria applied to time-resolved data with the plate at 90° and $Re = 8380$.

points M that lie in the domain S . The angle between the velocity vector \mathbf{U}_M and the radius vector \mathbf{PM} is θ_M . According to its definition, the Γ_1 is in the range $-1 < \Gamma_1 < 1$. In the proximity of the vortex centre the magnitude of Γ_1 reaches values higher than 0.9. The location of the centre is determined based on a threshold computation. The function Γ_1 is not Galilean invariant and a new function is required to properly identify the boundary of the vortical structures. If we take into account the local mean velocity around P , a new dimensionless and Galilean invariant scalar function Γ_2 is defined by Graftieaux et al. [51] as follows:

$$\Gamma_2(P) = \frac{1}{N} \sum_S \frac{[\mathbf{PM} \times (\mathbf{U}_M - \tilde{\mathbf{U}}_P)] \cdot \mathbf{z}}{\|\mathbf{PM}\| \cdot \|\mathbf{U}_M - \tilde{\mathbf{U}}_P\|} \quad (3.11)$$

where $\tilde{\mathbf{U}}_P = 1/N \sum_S \mathbf{U}$. The vortex region is identified as the area where the flow is locally dominated by rotation and the scalar dimensionless function is in the range $2/\pi < |\Gamma_2| < 1$. Contours of primary and secondary vortices identified with Γ_2 criterion are shown in [Figure 3.7b](#).

Eulerian methods are not invariant to time-dependent rotations, and thus are not objective (frame-independent) [59]. Additionally, all the above Eulerian criteria require a user-defined threshold to indicate the regions where a structure exists. The use of a threshold leads to an intrinsic level of ambiguity in the definition of a coherent structure. In case of high temporal and spatial resolution, Lagrangian techniques can be applied to provide complementary information.

3.4.2 Lagrangian data analysis

Lagrangian methods take advantage of the temporal information by integrating the observed quantities over a time interval. They are more complicated to apply and present a high computational cost but provide additional information about the flow field dynamics. They exploit the ergodicity of the system, which makes them inherently more robust to measurement noise and turbulent fluctuations.

A popular method for tracking vortices and analysing vortex dynamics is based on the calculation of the finite-time Lyapunov exponent (FTLE) [60]. The FTLE is a scalar field computed from particle trajectories and quantifies the stretching between particles trajectories, highlighting repelling or attracting regions in the fluid. The flow map $F_{t_0}^{t_1}(\mathbf{x}_0)$ computes the trajectory of a particle from an initial position \mathbf{x}_0 at time t_0 to its current position at time t_1 . The flow map gradient $\nabla F_{t_0}^{t_1}(\mathbf{x}_0)$ is then computed between times t_0 and t_1 by finite differences:

$$\nabla F_{t_0}^{t_1}(\mathbf{x}_0) = \begin{pmatrix} \frac{x(t_1; t_0, \mathbf{x}_0 + \delta x) - x(t_1; t_0, \mathbf{x}_0 - \delta x)}{2\delta x} & \frac{x(t_1; t_0, \mathbf{x}_0 + \delta y) - x(t_1; t_0, \mathbf{x}_0 - \delta y)}{2\delta y} \\ \frac{y(t_1; t_0, \mathbf{x}_0 + \delta x) - y(t_1; t_0, \mathbf{x}_0 - \delta x)}{2\delta x} & \frac{y(t_1; t_0, \mathbf{x}_0 + \delta y) - y(t_1; t_0, \mathbf{x}_0 - \delta y)}{2\delta y} \end{pmatrix}. \quad (3.12)$$

The maximum stretching $\sigma(t_0, \mathbf{x}_0)$ is given by the maximum eigenvalue λ_{max} of the Cauchy-Green tensor:

$$\sigma(t_0, \mathbf{x}_0) = \sqrt{\lambda_{max} \left([\nabla F_{t_0}^{t_1}(\mathbf{x}_0)]^T \nabla F_{t_0}^{t_1}(\mathbf{x}_0) \right)}. \quad (3.13)$$

The finite-time Lyapunov exponent is defined as the growth exponent of the maximum stretching:

$$\text{FTLE}_{t_0}^{t_1}(\mathbf{x}_0) = \frac{\ln(\sigma(t_0, \mathbf{x}_0))}{t_1 - t_0}. \quad (3.14)$$

For forward time integration ($t_1 > t_0$) FTLE ridges highlight repelling lines in the flow (positive FTLE). By integrating backward in time ($t_1 < t_0$) the attracting lines are highlighted (negative FTLE). These FTLE ridges, referred to as Lagrangian coherent structures (LCS), are effective at identifying boundaries of vortical structures and their temporal evolution in vortex dominated flows. When attracting or repelling lines intersect the surface of an object, such as a plate, a half-saddle is formed (Figure 3.8). The existence of an intersection between a solid wall and a FTLE ridge is technically not possible due to the no-slip condition. Klose et al. [73] recently showed that the no-slip condition mathematically converts the wall into a set of non-hyperbolic fixed points. As a result, any intersection with FTLE ridges is inhibited. Attracting lines are a good indicators of shear layers, and their intersections with repelling lines define Lagrangian full-saddle points (Figure 3.8). The full-saddles points topologically delimit points that particles can not cross and provide a good criterion to identify vortex separation [100, 65, 119, 76]. Eulerian methods are not suitable to easily identify saddle points due

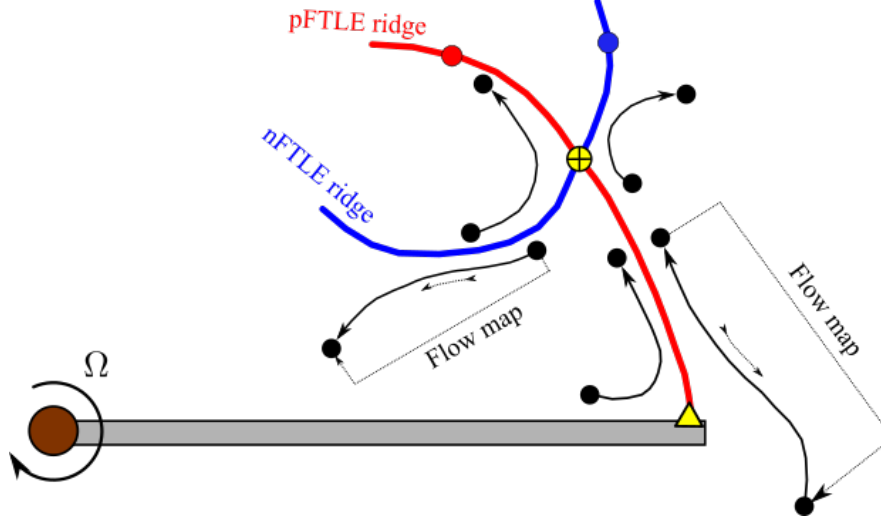


Figure 3.8: A schematic of the calculation of Lagrangian FTLE ridges around a rotating plate. Fluid particles close to the plate tip are stretched alongside attracting material lines (nFTLE ridges), whereas fluid particles are repelled by pFTLE ridge. The intersection between the attracting line and the plate tip identifies a half-saddle point. The intersection between attracting and repelling lines is a full-saddle point and fluid particles can not cross it.

to their variation with the frame of reference. The FTLE method is inherently objective and results are invariant with respect to any Euclidean frame change.

3.5 Computation of the vortex circulation

The velocity field obtained from PIV images can also be used to estimate integral quantities. The integration of the instantaneous velocity field yields field quantities such as the stream function or scalar values through path integrals. An example is the circulation, which is obtained through the path integration of the velocity field. This quantity is of particular interest in fluid dynamics because it is independent of the reference frame and is commonly used to quantify the strength of a vortex. The circulation is related to the vorticity by Stokes theorem:

$$\Gamma = \oint_{\partial A} \mathbf{u} \cdot d\mathbf{l} = \int_A \boldsymbol{\omega} \cdot \mathbf{n} dS \quad (3.15)$$

where ∂A is the contour of the flow region A inside which the circulation is computed. The Stokes theorem can also be applied for (x, y) -gridded velocity data. If we consider a generic grid point (i, j) , the circulation inside the region A is expressed as follows:

$$\Gamma = \sum_{i,j \in A} \omega_{i,j} dA_{i,j} = dx dy \sum_{i,j \in A} \omega_{i,j} \quad (3.16)$$

where $\omega_{i,j}$ is the vorticity value in the grid point (i, j) . In this formula we assumed that each grid point has the same area $dA = dxdy$, as it is for our data. The circulation can also be computed from the closed contour integral of the velocity field. If we consider $u_{i,j}$ and $v_{i,j}$ to be the grid Cartesian components of the velocity field on the contour ∂A , the circulation is given by:

$$\Gamma = \sum_{i,j \in \partial A} (u_{i,j}dx + v_{i,j}dy) \quad (3.17)$$

The quantity that is directly measured is the velocity field and vorticity is a derived quantity. For this reason, the circulation computed from the velocity field can lead to less uncertainties than the value obtained from Equation (3.16). In the following, we compare the circulation of primary and secondary vortices obtained from both velocity and vorticity fields.

The first thing to do when computing the circulation is the identification of the vortex contour. We used both the swirling strength and the Γ_2 criteria described in the previous section to identify vortex boundaries. The swirling strength criterion defines the vortex boundary as the limit over which the swirling strength λ_{ci} is negative. The threshold we set for the swirling strength criterion is 0. The contour given by Γ_2 considers the vortex core area as the flow region where Γ_2 is higher than $2/\pi$, which is the selected threshold. The circulation of the primary vortex, normalized with respect to the chord and the tip speed velocity, as a function of α is computed with both methods and results are shown in Figure 3.9a. The circulation increases with α until the plate has travelled approximately 30° . Above this angular position, the primary vortex circulation does not increase anymore. This behaviour highlights the limiting process of the primary vortex growth and both Γ_2 and λ_{ci} criteria capture this aspect. The difference between the circulation obtained from the two methods never exceeds 5%. A visual observation of the primary vortex contours obtained with the two methods is shown in Figure 3.9b, where we can see that the two different boundaries define approximately the same area. We conclude that both identification techniques provide the same result in terms of the primary vortex circulation and in the later chapters we use λ_{ci} criterion to detect vortex regions.

We now compute the primary vortex circulation by integrating the velocity around the contours defined by Γ_2 and λ_{ci} . The purpose is to check the discrepancy between the two methods of integration. We observe from Figure 3.9a that the highest discrepancy is observed when the plate is around 30° and 70° . At 30° , the vortex has almost reached its maximum circulation and the first secondary vortex is about to form. This makes the uncertainty of the velocity field around the primary vortex higher and the circulation computed from the two different methods deviates more. The discrepancy at 70° can be justified by considering that the first secondary vortex orbits very close to the primary and is about to merge. The proximity of the secondary vortex can lead to higher uncertainty on the velocity field around the primary vortex, which results in a slightly

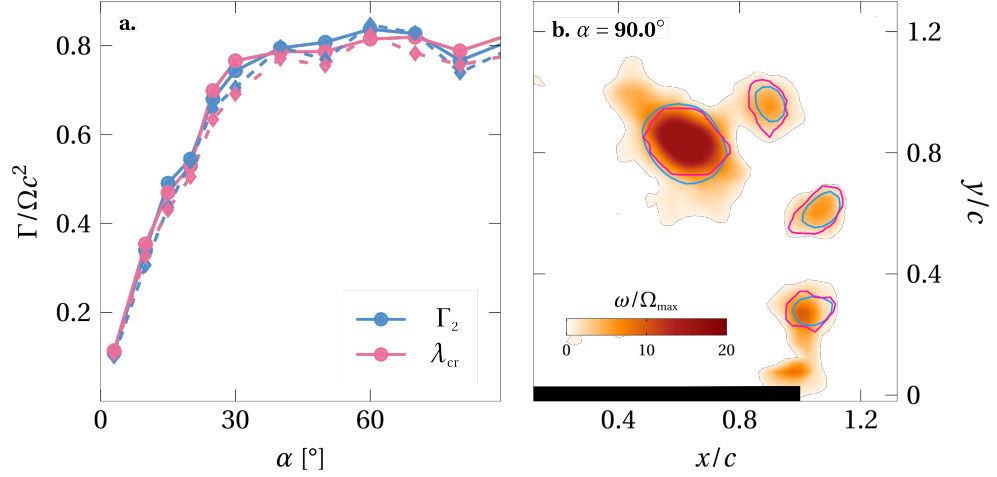


Figure 3.9: (a) Comparison between dimensionless circulation of the primary vortex as a function of α , computed with the swirling strength and Γ_2 criteria. Continuous lines and dots represent circulation computed by integrating vorticity inside the contours. Dashed lines and diamond marks represent circulation computed by integrating the velocity around the contours. (b) Vorticity flow field at $\alpha = 90^\circ$ for $Re = 8380$, overlapped with the swirling strength and Γ_2 contours.

bigger discrepancy in the computation of the circulation. However, the discrepancy between the two methods of integration never exceeds 5% and both methods provide the same information about the limiting process of the primary vortex.

The circulation is also computed for all the shed secondary vortices. We follow the same procedure used for the primary vortex and we first identify the contours with both criteria (Figure 3.9b). We observe that contours identified with the swirling criterion are slightly bigger than boundaries obtained from the Γ_2 function. Moreover, Γ_2 criterion fails to identify closed contours for some of the shed secondary vortices. For this reason, we decide to use the swirling strength criterion to identify contours of all secondary vortices. The circulation of all secondary vortices shed at $Re = 8380$, normalized with respect to the chord and the tip speed velocity, is shown in Figure 3.10. All secondary vortices present a much smaller circulation compared to the primary vortex. If we compute the circulation by integrating vorticity inside the contours (grey box plot in Figure 3.9) the circulation of all secondary vortices lies in a range that goes from 0.06 to 0.18. The strength of secondary vortices seems to be influenced by the increase of the number n of previously shed vortices. The uncertainty indicated by the grey box plot can be reduced if we integrate the velocity field around the vortex contours (purple box plot of Figure 3.9). The circulation range now goes from 0.06 to 0.14 and we observe a global increase of the circulation entrained into later shed secondary vortices. The reason behind this is further investigated in chapter 5.

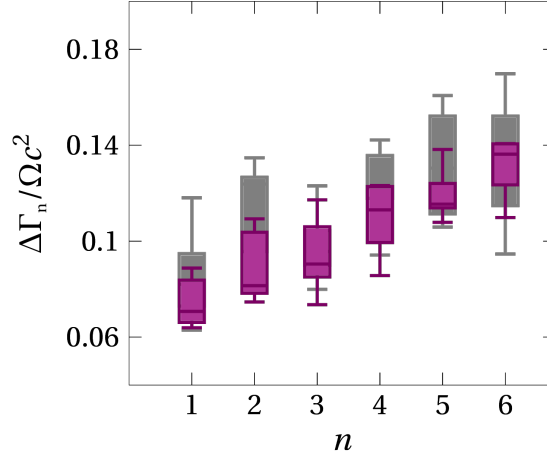


Figure 3.10: Circulation of all the n secondary vortices shed at $Re = 8380$. The box plot in grey indicates circulation computed by integrating the vorticity inside the contours. The integration of the velocity field around the same contours is shown by the purple box plot.

3.6 Computation of radial velocity and vorticity distribution

As a last step, we are interested in extracting a measure of the size of vortices and to check how computed quantities, such as velocity, vorticity and circulation, are related. For this purpose, we evaluate the vorticity and velocity distributions of formed vortices. Experimental velocity and vorticity grid points in the core region of vortices are fitted with the well known Lamb-Oseen vortex model [82, 104]. This model is an exact solution of the Navier-Stokes equations for a laminar and axisymmetric flow. If we consider a polar coordinate system placed at the vortex centre, the tangential velocity as a function of the radial distance r is:

$$v_\theta(r, t) = \frac{\Gamma'}{2\pi r} \left[1 - e^{-\frac{r^2}{r_c^2(t)}} \right] \quad (3.18)$$

From the radial equation of the tangential velocity, we can retrieve the vorticity distribution:

$$\omega(r, t) = \frac{\Gamma'}{\pi r_c^2(t)} e^{-\frac{r^2}{r_c^2(t)}} \quad (3.19)$$

This model is used to represent the viscous decay of a singular line vortex that has a finite circulation:

$$\Gamma(r, t) = 2\pi r v_\theta = \Gamma' \left[1 - e^{-\frac{r^2}{r_c^2(t)}} \right] \quad (3.20)$$

and satisfies the following boundary conditions:

$$\Gamma(r = 0, t = 0) = \Gamma', \quad \Gamma(r = 0, t) = 0, \quad \Gamma(r \rightarrow \infty, t) = \Gamma' \quad (3.21)$$

At $t = 0$, the entire circulation is concentrated on the line vortex. At a later time t , the line vortex radially expands with an expanding core radius $r_c(t) = \sqrt{4\nu t}$, with ν being the kinematic viscosity. The Lamb-Oseen vortex at a 'frozen' time t_0 and core radius $r_c = \sqrt{4\nu t_0}$ is equivalent to a q-vortex or a Batchelor vortex [6].

3.6.1 Description of the fitting algorithm

In this section we describe the Lamb-Oseen vortex fitting algorithm used to extract velocity and vorticity distributions from experimental data. A similar approach was also used by Stevens and Babinsky [134] to estimate the circulation of a LEV generated from a pitching flat plate. The initial step is to select a region that fully includes the analysing vortex. All the vorticity points inside this region are used to retrieve the Lamb-Oseen fit. The next step is to compute the radial distance r of all the vorticity points from the vortex centre. We first select the location of the maximum vorticity level in the selected region as the vortex centre (x_c, y_c) . The coordinates of this point are highlighted in orange in Figure 3.11a. Once we know the vorticity points in the vortex region and their distance from the centre r , we can fit the experimental points with Equation (3.19).

The fitting algorithm properly selects the location of the vortex centre and allows to go beyond the resolution of our PIV data. We consider a neighbourhood area centred around (x_c, y_c) (grey square in Figure 3.11a) and we divide it into a m^2 number of points. The choice of m is based on a sensitivity analysis. We quantify the computational cost of the algorithm and the percentage error $Rmsq_{\%}$ for increasing m and use them as a benchmark to evaluate the optimum sub-grid width. The percentage error is calculated as the root mean square error between the experimental vorticity points and the Lamb-Oseen fit. The trade-off is made by comparing the benefit from the reduced $Rmsq_{\%}$ and the drawback due to higher computational cost. The increased computational time is not worth the reduced percentage error when $m > 8$ (Figure 3.11c-d) and we choose to divide the neighbourhood area A_n in 64 points. Each point (x_i, y_i) inside the neighbourhood area, with $i = 1, \dots, 64$, is iteratively assumed to be the vortex centre (x_c, y_c) . The output of our algorithm is to find the best centre location that minimizes the root mean square between the experimental data and the fit. This point is highlighted in purple in Figure 3.11a.

The location of the vortex centre significantly influences the goodness of the results. A comparison between vorticity distributions with the centre placed at the starting point and at the refined output position is shown in Figure 3.11b. If the centre of the vorticity distribution is assumed to be the initial position, the error is 20 % higher. This result proves the goodness of the algorithm to refine the vortex location centre beyond the grid data resolution.

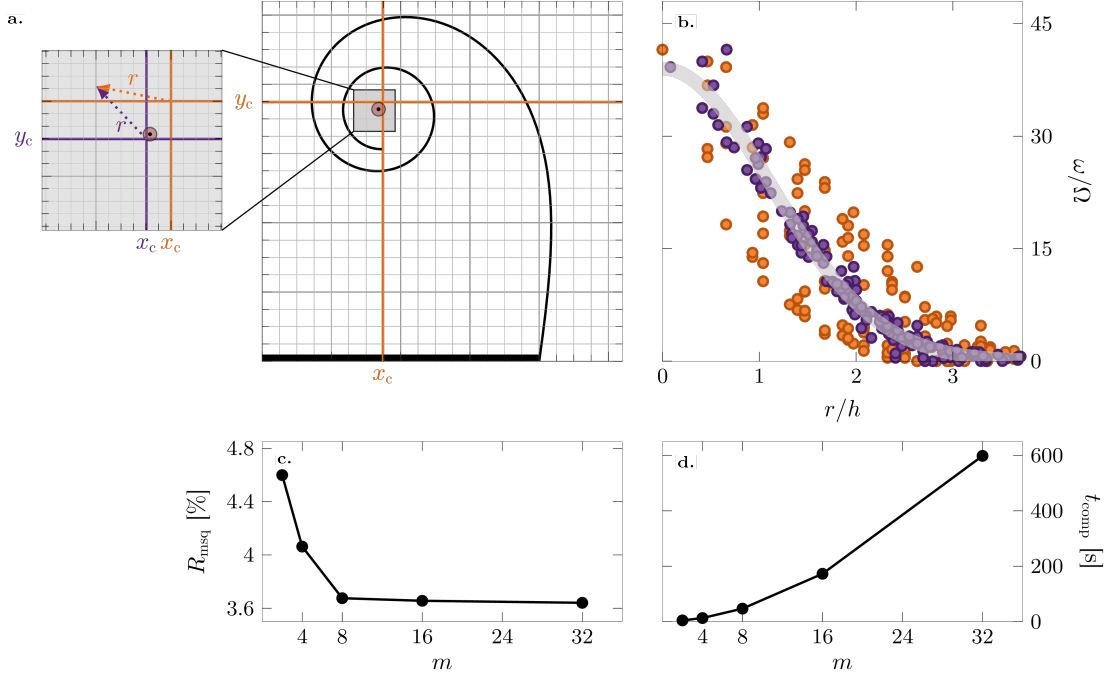


Figure 3.11: (a) Schematic drawing of the flow region in which the fitting algorithm is applied. The rolled-up portion of the spiral describes the vortex location. The grey square box is the neighbourhood area inside which the best centre location is selected. The coordinates (x_c, y_c) in orange and purple illustrate the initial and the best vortex centre positions. (b) Vorticity distributions with the centre located at the initial (orange dots) and final (purple dots) positions. The solid grey line represents the Lamb-Oseen curve. (c) Percentage error $R_{rmsq}_{\%}$ of experimental points from the Lamb-Oseen fit and (d) computational time as a function of the number of sub-grid points m .

The last thing we mention is the choice of the size of the neighbourhood area. We perform a sensitivity analysis using the displacement vector Δ between the initial and the final centre positions:

$$\Delta = (x_{c,f} - x_{c,i})\mathbf{i} + (y_{c,f} - y_{c,i})\mathbf{j} \quad (3.22)$$

as a benchmark to properly evaluate the correct size of the neighbourhood area. For all the experimental runs, we have never observed a displacement Δ higher than 0.5 mm. We decide to choose a square region of side 0.55 mm as the neighbourhood area around the initial centre location, for all the tested cases. This area is large enough to include the best output location of the vortex centre but not too large to significantly increase the computational cost.

3.6.2 Size and velocity profile for the primary vortex

The output of the fitting algorithm is the best location of the vortex centre, from which the radial scattering of the experimental vorticity points is evaluated. Once the experimental distribution is known, we can fit the experimental data with the Lamb-Oseen fit.

We normalized the radial distance from the centre with respect to the plate thickness h and the vorticity with respect to the angular speed of the plate Ω . We first apply the algorithm to the primary vortex for $Re = 8380$ and with the plate at 30° that approximately corresponds to the angular position at which the vortex stops growing (Figure 3.9a). The solid grey line in Figure 3.11b represents the Lamb-Oseen fit of the primary vortex at 30° . The fit allows us to estimate the core radius and the maximum level of vorticity of the vortex. The core radius r_c represents a measure of the vortex size and the maximum level of vorticity ω_{max} at the centre is related to the core radius through Equation (3.19):

$$\omega_{max} = \frac{\Gamma'}{\pi r_c^2(t)} \quad (3.23)$$

We estimate a core radius of $r_c/h = 1.6$ and a maximum vorticity of $\omega_{max}/\Omega = 39$ for the primary vortex at 30° .

Once we determine the values of r_c and ω_{max} , we can compute the circulation as a function of the distance from the centre with Equation (3.19). The result is shown by the solid grey line in Figure 3.12a and the curve is compared with the experimental circulation. We measure the circulation around a varying radius circle centred at the vortex centre (x_c, y_c) and the agreement with Lamb-Oseen is remarkable (Figure 3.12a). The circulation inside a circle of radius r_c directly follows from Equation (3.20) and is:

$$\Gamma_{rc} = \omega_{max} \pi r_c^2 (1 - e^{-1}) \quad (3.24)$$

For $\alpha = 30^\circ$, the circulation inside a circle of radius $r_c = 0.0034$ m is $\Gamma_{rc}/(\Omega c^2) = 0.59$. This value is lower than 0.76 measured at 30° with λ_{ci} and Γ_2 (Figure 3.9a). The explanation behind this discrepancy is first that the circular core area of radius r_c is smaller than the region identified with the other two methods (Figure 3.12b). Secondly, a Lamb-Oseen vortex is by definition a circular core region. Our experiments show that the vortex region slightly differs from a circular shape (Figure 3.12b). The dimensionless circulation measured with Γ_2 or λ_{ci} matches the value retrieved from Lamb-Oseen if we take a core radius of approximately $1.3r_c$ (Figure 3.12a). We define the scaling parameter k as the ratio between the circulation inside a circle of radius r_c and the circulation measured from the swirling strength or Γ_2 criterion. The value of k is obtained from Equation (3.20) by considering that the circulation measured from λ_{ci} or Γ_2 criterion is equivalent to the circulation inside a core radius of $1.3r_c$. This leads us to:

$$k = \frac{\Gamma_{rc}}{\Gamma_{\lambda_{ci}}} = \frac{1 - e^{-1}}{1 - e^{-1.3^2}} \approx 0.78 \quad (3.25)$$

We observe that the primary vortex keeps the same value of the scaling parameter k for later angular positions and for all the tested speeds.

The identification of the core radius and maximum vorticity allows us to determine the tangential and radial velocity distributions. If we set a polar coordinate system at

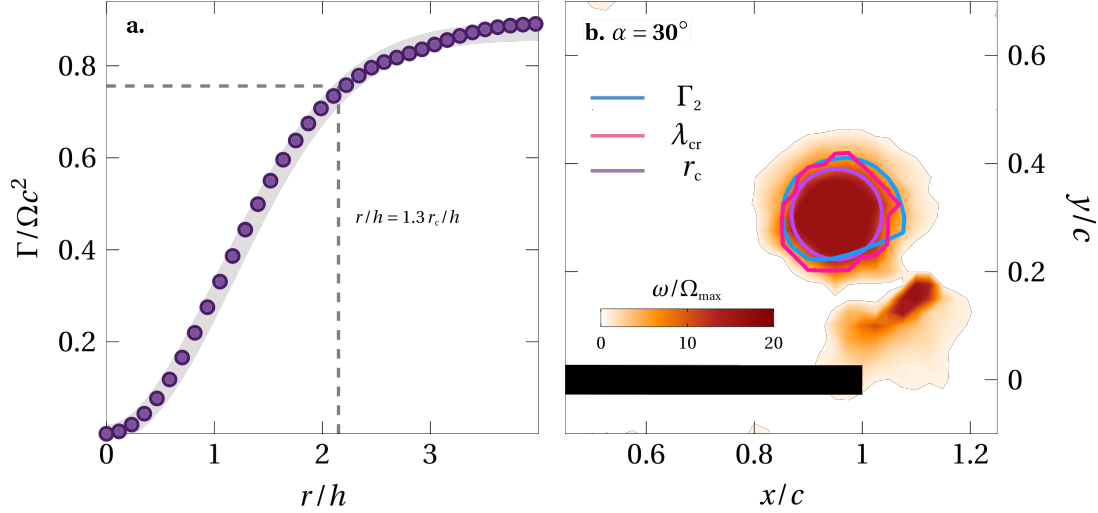


Figure 3.12: (a) Measured circulation as a function of the radial distance from the vortex centre at $\alpha = 30^\circ$ for $Re = 8380$. The solid grey line corresponds to the Lamb-Oseen curve. (b) Snapshot of the vorticity field at 30° in which the three different contours are highlighted.

the vortex centre, the radial velocity of a Lamb-Oseen vortex is zero and the tangential velocity is given by Equation (3.18) and shown by the grey line in Figure 3.13a. The tangential velocity increases with the radial distance from the centre, until the core radius value is reached. At this point the tangential velocity equals the tip plate speed and decreases afterwards. As we did above for the circulation, we compare the Lamb-Oseen tangential velocity with experimental values. Each grid point of processed PIV images has Cartesian components u, v of the velocity field. We need first to pass from Cartesian to polar coordinates by using the following conversion:

$$v_\theta = \frac{xv - yu}{r}, \quad v_r = \frac{xu + yv}{r} \quad (3.26)$$

where $r = \sqrt{x^2 + y^2}$ is the distance from the vortex centre. Then, we subtract the velocity of the vortex centre from the velocity field. This step is required because the Lamb-Oseen vortex is irrotational and does not translate while the primary vortex moves along the tip plate trajectory (Figure 3.4a-f). At each radial distance r from the vortex centre we calculate the average and the standard deviation of the tangential velocity. As for the circulation, the match between experimental values of the tangential velocity and Lamb-Oseen is remarkable (Figure 3.13a). The same is also done for the radial velocity for which we measure an average value of zero, regardless the distance r from the centre.

We observed in Figure 3.9a that the primary vortex circulation stops growing when the plate is around 30° . Beyond this angular position, circulation is not entrained anymore and the only mechanism acting on the primary vortex is the viscous diffusion. The plate travels 30° in $t_0 = 0.21s$, as shown in the bottom plot of Figure 3.4, and the core radius

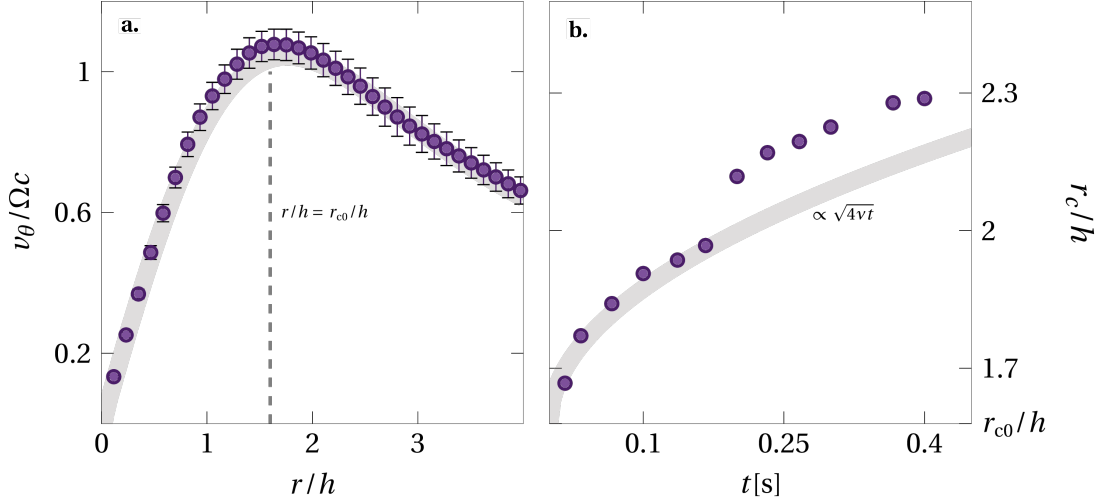


Figure 3.13: Measured tangential velocity as a function of the radial distance from the vortex centre at $\alpha = 30^\circ$ for $Re = 8380$. The solid grey line corresponds to the Lamb-Oseen curve. (b) Time evolution of the primary vortex core radius from 30° compared with the viscous diffusion.

of the primary vortex is $r_{c0} = 0.0034$ m (Figure 3.11b). From this point, we can estimate the viscous diffusion in time of the core radius with the following equation:

$$r_c(t) = r_{c0} + \sqrt{4\nu(t - t_0)} \quad (3.27)$$

that is illustrated in Figure 3.13b by the solid grey line. When the plate travels from 30° to 70° , the core radius expands in time according to Equation (3.27). Around 0.2 s after the plate reached 30° , the core radius has a jump and deviates from the viscous diffusion law. This happens when the plate is around 90° (Figure 3.4d), which corresponds to the moment at which the first secondary vortex merges with the primary. The increase of the core size does not correspond to an increase of circulation of the primary vortex that remains constant to $\Gamma/(\Omega c^2) \approx 0.8$ (Figure 3.9a). The hypothesis we make is that during the merging the vorticity coming from the first secondary vortex is redistributed in a bigger area such that the circulation remains the same. However, the merging process of vortices is out of the scope of the present work and we address the reader to the work of Leweke et al. [86], Meunier et al. [92], in which the merging of a corotating vortex pair of unequal strength is discussed in details. After that, the core radius returns to increase according to the viscous diffusion law.

3.6.3 Size and velocity profile for secondary vortices

The same fitting algorithm can also be applied to secondary vortices. We take the first and the last secondary vortices shed at $Re = 8380$ and we compute the vorticity and velocity distributions for both of them. The distributions of the first and last secondary

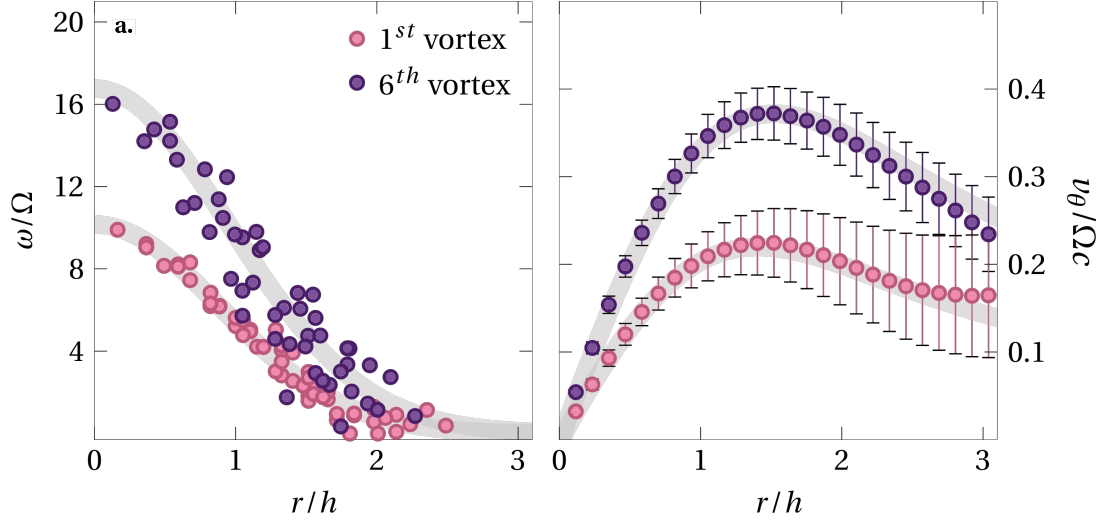


Figure 3.14: (a) Vorticity and (b) tangential velocity distribution of the first and last secondary vortices shed at $Re = 8380$.

vortices are evaluated when the plate is at 41° and 135° , respectively. These angular positions correspond to the moment at which the vortices separate from the tip of the plate. See next chapter and in particular [section 4.3.3](#) for further details about the identification of the shedding timing of secondary vortices.

The Lamb-Oseen model fits well the experimental data for both secondary vortices ([Figure 3.14a](#)) and confirms that the vorticity inside primary and secondary vortices is well represented by Lamb-Oseen's model. The secondary vortex that sheds immediately after the primary vortex has a non-dimensional maximum vorticity of approximately 10 and a core radius of 1.26 times the plate thickness. The last secondary vortex that is shed when the plate is towards the end of the rotation presents a maximum vorticity of 17 and a radius-to-thickness ratio r_c/h of 1.34. This result suggests that the last secondary vortex is slightly stronger than the first one, as also observed in [Figure 3.10](#).

The tangential velocity increases as a function of the distance from the vortex centre for both secondary vortices, according to [Equation \(3.18\)](#) ([Figure 3.14b](#)). At $r = r_c$, the tangential velocity around the first secondary vortex is on average around 0.2 times the tip speed of the plate. A higher value of 0.35 is reached around the last secondary vortex at a distance r_c from the centre, confirming the evidence that the last vortex is stronger than the first one. Beyond the core radius r_c , the tangential velocity decreases in agreement with [Equation \(3.18\)](#). The higher uncertainty of experimental values associated with the tangential velocity around the first secondary vortex is due to the close presence of the primary vortex.

As we did for the primary vortex, we can estimate the circulation of secondary vortices from Lamb-Oseen's fit. We show in [Figure 3.15a](#) the circulation of the two analysed vortices as a function of the radial distance from their centres. At a radial distance $r = r_c$,

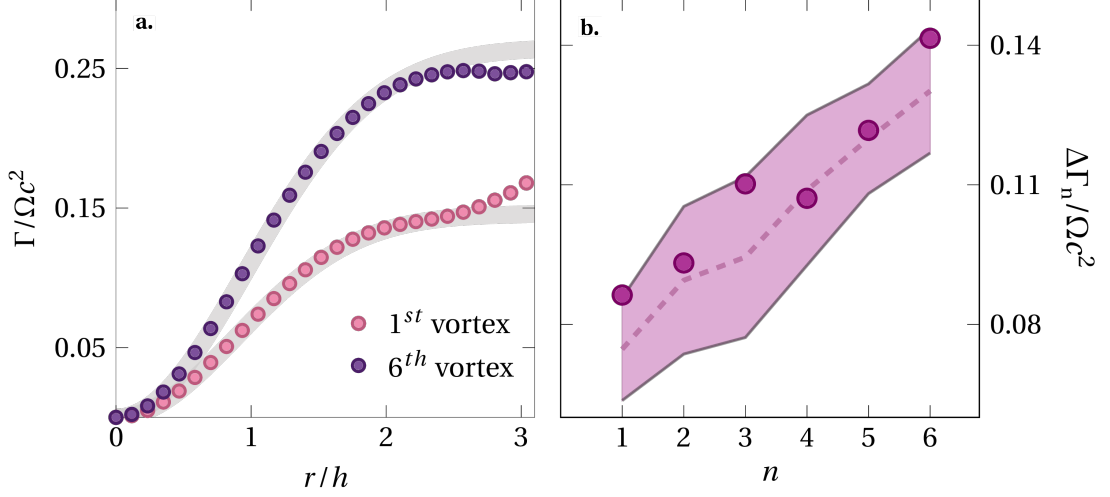


Figure 3.15: (a) Measured circulation of the first and last secondary vortices shed at $Re = 8380$ as a function of the radial distance from the vortex centre. (b) Circulation of all shed secondary vortices estimated with Lamb-Oseen (purple dots) overlapped on the pink region that corresponds to the pink box plot of Figure 3.10.

the dimensionless circulation entrained in the first and last secondary vortices is 0.09 and 0.14. These values are very close to the circulation measured inside the contours identified with the swirling strength criterion. Contrary to the primary vortex that slightly differs from a circular shape, a circle of radius r_c resembles well the contours of secondary vortices identified with λ_{ci} (Figure 3.9b). We estimate the circulation from Lamb-Oseen for all the six shed secondary vortices at $Re = 8380$ and we show results in Figure 3.15b. The later the secondary vortex is released, the higher the circulation entrained in its core radius. This observation is in line with the results shown in Figure 3.10, in which the circulation of secondary vortices is computed by integrating the velocity field around λ_{ci} contours. The increase of circulation in the later shed secondary vortices is further discussed in chapter 5.

3.7 Influence of the flow field resolution and three-dimensional effects

In the previous sections, we showed the comparison between vorticity and velocity fields from time-resolved and phase-averaged data. Time-resolved data have a lower spatial resolution compared to phase-averaged images, but all the main topological aspects of the flow field are still well captured (see Figure 3.4d and Figure 3.5b). The main difference consists in a more detailed view of the merging process between the primary and the first secondary vortices.

Here, we analyse the impact of the flow field resolution on the computation of quantita-

tive flow features, in particular the vorticity distribution. We apply the fitting algorithm to the primary vortex when the plate is at 90° and we compare results to phase-averaged data (Figure 3.16). The maximum vorticity has a value of 25 and the same value is confirmed for higher resolution data. A slight difference is noted for the core radius that is 17% smaller when we apply the fitting algorithm to phase-averaged data. An increased resolution provides a more refined and smaller area of the vortex region. As a consequence, the measured circulation of the primary vortex is lower when the grid resolution is increased. This evidence is also confirmed by the two identification criteria λ_{ci} and Γ_2 , which identify a slightly smaller region of the primary vortex. There are two interesting aspects to underline. First, we obtain the same value of circulation inside the contours identified with λ_{ci} and Γ_2 for phase-averaged data as well. Second, the ratio between the circulation inside a circle of radius r_c and the circulation inside a λ_{ci} or Γ_2 contour is equal to the same scaling factor k defined in Equation (3.25). These two observations add validity to the identification of the primary vortex contour made from time-resolved images.

We used the fourth secondary vortex as a benchmark to check how the resolution affects the vorticity distribution of secondary vortices. The reason behind this choice is that the fourth secondary vortex is shed when the plate is around 90° and the comparison is not affected by viscous diffusion. As we observed for the primary vortex, the maximum vorticity of the fourth secondary vortex estimated from higher and lower resolution data has the same value that is equal to 14 (Figure 3.16). The core radius is approximately 19% smaller for higher resolution data, which leads to a lower measured circulation. We also measure a smaller core region of the fourth secondary vortex with both λ_{ci} and Γ_2 criteria for higher resolution data.

We conclude that higher resolved data gives a better refinement of the vortex region and slightly smaller values of circulation compared to time-resolved data. However, this improvement is not fundamental for the purpose of this work and does not prevent us to use time-resolved data in the next chapters.

The last thing we discuss is the possible influence of three-dimensional effects in the measurement plane. We place the measurement plane at mid-span and since the plate rotates about its mid-chord, the symmetry should guarantee that three-dimensional effects are negligible. As observed by Auerbach [4], vortices generated by an impulsively started flow about a sharp edge and bounded by two sides are not influenced in the mid-plane from these two sides for a time. However, the vortex perturbation along the span propagates from the root of the plate towards the measurement plane and induces an axial velocity (see section 2.6 for further details). This axial velocity is orthogonal to the measurement plane and can affect our results. To have a rough estimation of the velocity u_{sh} of the perturbation along the vortex we extract data from experimental observations found in [85]. The velocity with which the perturbation propagates along the span is proportional to the circulation based Reynolds number $Re_\Gamma = \Gamma/\nu$ and in

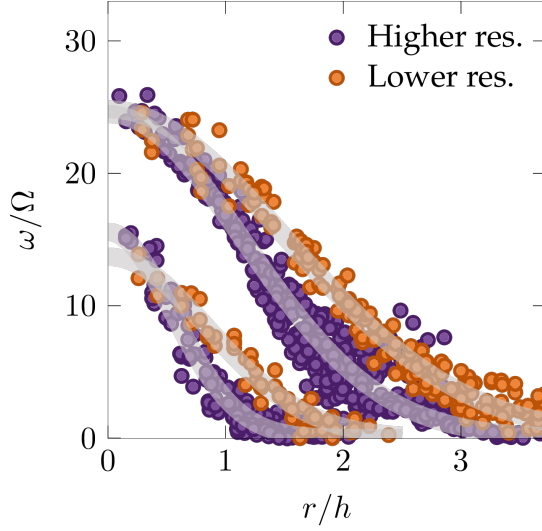


Figure 3.16: Vorticity distributions of primary and fourth secondary vortices computed from time-resolved (orange) and phase-averaged (purple) data. The solid grey lines are the corresponding Lamb-Oseen fit.

the range $2400 < Re_{\Gamma} < 12000$ can be estimated through the following equation:

$$u_{sh} = cRe_{\Gamma} + d \quad (3.28)$$

where $c = 2.2 \times 10^{-5} \text{ m s}^{-1}$ and $d = -0.015 \text{ m s}^{-1}$ are fitting constants extracted from the data in [85]. Equation (3.28) is used to check if the perturbation arrives at the measurement plane during the motion of the plate. For $Re = 8380$ the primary vortex reaches a dimensional strength of $0.0063 \text{ m}^2 \text{ s}^{-1}$ (Figure 3.9a), which leads to a circulation based Reynolds number of 6300. The perturbation has to travel 8 cm along the span direction to reach the measurement plane and has a speed of 0.12 m s^{-1} , according to Equation (3.28). This means that the perturbation arrives at the measurement plane in 0.7 s that corresponds to the entire period of the plate rotation (Figure 3.4 bottom). We conclude that the perturbation is in the measurement plane only when the rotation has already finished and is not responsible for the appearance of secondary vortices.

3.8 Summary and conclusions

In this chapter we presented how our experimental data are taken and processed. The first part is dedicated to the description of the rotation mechanism, highlighting its robustness and reliability to take repeatable measurements. We also showed the geometry and the kinematics of the rotating plate, whose motion leads to the formation of several vortical structures.

The description of the entire optical set-up used to record PIV images was presented

and particular attention was given to the cameras used. The high-speed camera allowed us to get time-resolved data during the entire motion of the plate. The processing of this data showed the occurrence of a primary vortical structures, followed by the subsequent shedding of smaller secondary vortices. We used the sCMOS, which has a higher resolution but a lower frame rate than the high speed camera, to grab phase-averaged data of the velocity and vorticity field when the plate has travelled 90° . We observed from these images the existence of three different flow topologies, depending on the maximum rotational speed of the plate. Phase-averaged data allowed us to check if the increased grid resolution provided additional and more refined quantitative information about the flow field. A direct comparison between time-resolved and phase-averaged data showed that higher-resolved data does not contribute more quantitative information to the purpose of the present work.

Finally, we dedicated the last sections to the computation of the main vortex quantities. We discussed the different methods used to identify vortex contours and we applied the swirling strength and the Γ_2 criteria. The circulation was computed by integrating both vorticity inside the contour and velocity around the same contour. Results showed no discrepancies between the two ways of integration, except for a lower uncertainty when computing the circulation of secondary vortices from a closed line integral of the velocity. We also evaluated the vorticity and velocity distributions of primary and secondary vortices. We fitted the experimental data with the Lamb-Oseen vortex model and we described the working procedure of the fitting algorithm. The algorithm provided the best location of the vortex centre and we estimated the core radius and the maximum level of vorticity for each formed vortex. All the techniques and data showed in this chapter are the starting point of the next two chapters, in which we present the main results of the thesis.

Chapter 4

Discrete shedding of secondary vortices

In this chapter the focus is mainly on the shedding of secondary vortices. First, we recall the most important studies found in literature about this topic. We highlight the main questions that are still unanswered and that represent the motivation of our study. At the end of the first section we clarify the unsolved aspects we are going to address. Afterwards, a brief summary of the experimental set-up is given. Look at [chapter 3](#) for further details. The third section is the core part of the chapter. We describe there the results we got and we try to provide a physical explanation to all of them. Finally, we summarize the take home messages from this chapter.

The work presented in this chapter has been published in Journal of Fluid Mechanics [\[43\]](#).

4.1 Literature studies about the topic

The life of vortices around bluff bodies often begins with a shear layer [\[39, 67, 120, 38, 19\]](#). When a bluff body moves relative to a fluid flow, a thin layer of fluid emerges at the edge of the body where non-zero shear flow gradients are present. This shear layer is characterised by increased values of the flow vorticity. In the wake of the body, the shear layer rolls-up and the shear layer vorticity accumulates into a coherent vortex. The interplay between the free stream or body's velocity and the induced velocity of the growing coherent vortex cause the shear layer to become curved. This curvature changes continuously in time. The roll-up of a semi-infinite shear layer or vortex sheet was first described by Kaden [\[69\]](#), who derived the following self-similar equation to

describe the shear layer shape at any point in time t :

$$r = K(t/\theta)^{2/3} \quad (4.1)$$

where K is a dimensional constant, and r and θ are the radial and angular coordinates along the spiral with $r = 0, \theta \rightarrow \infty$ at the spiral centre, $r \rightarrow \infty, \theta \rightarrow 0$ at the opposite end of the semi-sheet at infinity. The exponent $2/3$ is retrieved from dimensional analysis and the obtained curve is a spiral with tight inner turns (see [section 2.2.2](#)). The initial strength of the flat sheet increases monotonically with increasing distance away from the tip of the body. For $t > 0$, the spiral has an infinite number of turns leading to a singularity of the velocity and the sheet strength decreases to zero for $\theta \rightarrow \infty$ in the spiral centre. The maximum value of the sheet strength is now located somewhere along the sheet [125]. In reality, viscosity will remove any singularity at the spiral centre and yield the development of a viscous core [97].

At the early stages of the roll-up, Kaden's spiral is tight with a low local radius of curvature. It accurately represents the initial evolution of the shear layer. At later stages, the radius of curvature increases due to the viscous interactions within the shear layer and between the shear layer and the coherent primary vortex that grows due to the continuous accumulation of vorticity at the centre of the spiral. The distortions can be investigated by modelling the inner portion of the spiral as a single point vortex located at the centre [95]. The entire shear layer roll-up can also be predicted by a point-vortex representation of an initially straight vortex sheet [75, 27]. The degree of the elliptical distortions depends on the shape of the object. They are almost negligible for flat plates and become more pronounced when the edge has a non-zero wedge angle [111].

The accumulation of the vorticity in the coherent vortex in the spiral centre does not continue indefinitely. There is a physical limit to the size and the amount of circulation the primary vortex can collect [49, 26, 46, 94]. When the primary vortex is about to pinch-off, a trailing pressure maximum is observed along the shear layer [83]. The shear layer region between the tip and the trailing pressure maximum has an adverse pressure gradient. The remaining portion of the shear layer is characterised by a positive pressure gradient. The two regions of the shear layer are now separated and the vorticity associated with the adverse pressure gradient can not be entrained into the vortex core. The trailing pressure maximum travels downstream together with the primary vortex, causing the subsequent pinch-off of the primary vortex [128]. Additional vorticity will not be entrained by the primary vortex after pinch-off and instead can accumulate into smaller secondary vortices within the trailing shear layer similar to a Kelvin-Helmholtz instability [20]. The increases in shear layer curvature during the initial stages of the vortex formation momentarily stops when the end of the primary vortex growth is reached [126]. Secondary vortices occur first between the primary vortex and the tip at locations where the sheet strength according to Kaden is maximal [95, 74].

The emergence of secondary vortices seem to occur only if the Reynolds number is above a critical threshold. The value of this critical Reynolds number varies for different object geometries and boundary conditions. Critical values in a range from $Re = 1000$ to 3000 were observed in a cylinder wake by Wu et al. [144]. The lower limit was slightly higher for [11], who did not detect any instabilities for $Re < 1300$. The span-wise and end configurations strongly affect the shear layer breaking behind a cylinder. Parallel and oblique vortex shedding are obtained by changing the inclination of end plates [110]. The shear layer manifests instabilities at $Re = 1200$ for parallel shedding and at $Re = 2600$ for oblique shedding. The critical Reynolds number for an accelerated sharp edged plate lies in a higher range. Pullin and Perry [112], Williamson [141] started to visually observed secondary vortices along the shear layer for $Re = 4268$. This value was later confirmed by Luchini and Tognaccini [90], who numerically observed the occurrence of secondary vortices in a range from $Re = 4500$ to 5000 .

For Reynolds numbers above the critical value, series of secondary vortices appear in the trailing shear layer with a seemingly constant distance between them. The typical shear layer frequency in the wakes of cylinders is much higher than the frequency of the von Karman vortex street. A consensus about the exact relationship between the frequency of the primary vortex shedding f_K and the secondary of shear layer vortices f_{SL} has not yet been found. Bloor [11] observed that the ratio between the characteristic frequencies varies with Reynolds number according to $f_K/f_{SL} = Re^{1/2}$. However, there is no consensus about the exponent value of the proposed relationship. Prasad and Williamson [110] indicated that an exponent value of 0.67 works for Re up to 10^5 and Wei and Smith [139] found 0.87 in the range from $Re = 1200$ to $11\,000$. No clear relationships are established in the situation of an isolated primary vortex. Based on the flow visualisation around a submerged flat plate, Grift et al. [57] determined the shedding frequency of secondary vortices to lie in the range from 13 Hz to 20 Hz , for different values of acceleration, velocity, and immersion depth. This range corresponds to a Strouhal number around 0.2 , according to the plate geometry and kinematics used by the authors. The secondary vortex shedding frequency behind a vertical flat plate increases with increasing acceleration of the flat plate according to Rosi and Rival. It is crucial to define a scaling parameter, such as the Strouhal frequency for the cylinder case, that allows for a more universal relationship between the shedding frequency or formation time of primary and secondary vortices as a function of the Reynolds number.

Secondary vortices also have a practical relevance for a broad range of applications. They can create additional lift on delta wings at high angles of attack [45], cause vortex induced oscillations of solid structure that lead to fatigue damage [130], and lead to increased drag and noise for wing tip vortices [9]. A precise prediction of secondary vortices can improve aerodynamic performance and reduce vortex induced vibrations and noise.

Here, we present an experimental study of secondary vortices generated by a rotating

flat plate in a quiescent fluid. The experimental setup is discussed in details in the following section and is similar to the configurations used by David et al. [25], Corkery et al. [19], Carr et al. [16]. The plate is rotated with a constant rotational velocity which is varied across different experiments. The rotation of the plate generates a start up or a primary vortex. As the plate keeps rotating, the primary vortex separates and smaller secondary vortices are observed. First, we determine the critical Reynolds number above which secondary vortices are observed in the shear layer behind the tip of the rotating plate. Second, we describe the path of secondary vortices and model their path using a modified Kaden spiral. Finally, we estimate the timing of the secondary vortex shedding process and analyse the effect of the Reynolds number on the timing.

4.2 Experimental methods

The first series of measurements is conducted with a rectangular flat glass plate, with length $l = 8$ cm, width or span $s = 16$ cm and thickness $h = 2$ mm that is rotated about 180° in a water tank around its centre span-wise axis. The distance between the centre of rotation and the tip of the plate is referred to as the chord length c here. The length of the plate is reduced to $l = 4$ cm and the rotation point is shifted to the edge of the plate for the second set of measurements. The chord length or distance between the rotational point and the tip of the plate is preserved for both sets of experiments. For the first set of experiments, vortices are formed symmetrically behind both ends of the plate. For the second set of experiments, vortices are formed only on one end of the plate. This allows us to study the influence of the rotation point and detect potential interferences caused by symmetric vortex release on both tips when the rotation point is at mid-length. A third set of measurements with a longer plate with length $l = 12$ cm and the rotation point at mid-length, yielding a chord length of $c = 6$ cm, was conducted to provide insight into the influence of the chord length on the vortex formation. The glass plate is stiff enough to not bend due to the interaction with water and its transparency prevents shadow regions when performing particle image velocimetry (PIV). The experiments are conducted in an octagonal tank with an outer diameter of 0.75 m filled with water (Figure 4.1a).

The rotation mechanism is fastened to an outer aluminium frame such that the mid span of the plate is in the centre of the tank to limit wall interference effects. The kinematic input is given by a servo motor (Maxon RE 35) connected to a stainless steel shaft and transferred to the flat plate through a 1 : 1 conical coupling. A 1 : 19 gearbox is mounted on the motor to ensure high torque, speed, and acceleration. The rotational angle, speed, and acceleration are controlled via a Galil DMC-40 motion controller, which allows for accurate control of arbitrary motion profiles. The rotation programme is a trapezoidal rotational velocity profile with a fixed rotational amplitude of 180° (Figure 4.1b).

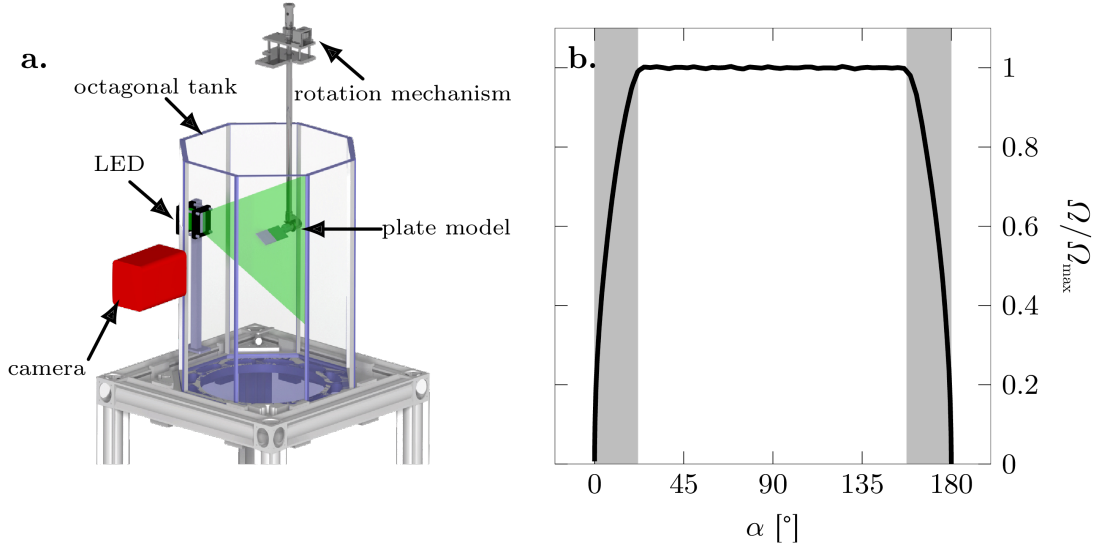


Figure 4.1: (a) Schematic of the experimental set-up and the rotation mechanism. (b) Trapezoidal velocity profile as a function of the angular position. The grey shaded regions indicate the portion of the motion during which the plate is accelerated.

To ensure a continuous acceleration profile, the corners of the velocity trapezoid are smoothed. The maximum rotational speed Ω_{\max} is varied from 30°s^{-1} to 400°s^{-1} . This leads to a Reynolds number $Re = (\Omega_{\max} c^2)/\nu$ ranging from 840 to 11 150. ν is the kinematic viscosity of the water and the chord c is defined as the distance between the rotation point and the tip of the plate. The rotational acceleration $\dot{\Omega}$ is fixed at 6000°s^{-2} .

The PIV images are recorded in the cross-sectional plane at the model mid span. A high-power pulsed light-emitting diode (LED Pulsed System, ILA 5150 GmbH) is used to create a light sheet in the measurement plane. The applicability of high-power LED for PIV has been demonstrated previously by Willert et al. [140], Krishna et al. [76]. Time-resolved PIV images are recorded with a Photron FASTCAM SA-X2 high speed camera. The camera is equipped with a 35 mm Canon lens and the camera is aligned carefully such that the optical axis of the lens is aligned with the rotational axis of the plate and is perpendicular to the light sheet (Figure 4.1a). The frame rate and the exposure time are varied, depending on the dynamics of the motion. A frame rate and exposure time of 250 Hz and 1 ms are selected for a rotational speed of 30°s^{-1} . These values are 2000 Hz and 0.5 ms for the highest tested speeds. The frame rate is high enough to capture the dynamics of the motion and the LED is set to continuous mode. The camera resolution is $1024 \text{ px} \times 1024 \text{ px}$, which corresponds to a field of view of $20 \text{ cm} \times 20 \text{ cm}$. The raw data are processed by the commercial software PIVview (PIVTEC GmbH, ILA 5150 GmbH) using a correlation model based on minimum squared differences and a multi-pass interrogation algorithm with three iterations. The final interrogation window size is $32 \text{ px} \times 32 \text{ px}$ with an overlap of 68 %. A third order B-spline interpolation method for sub-pixel image shifting is performed on all passes. The resulting physical resolution is 1 mm, or $0.025c$ with $c = 4 \text{ cm}$.

4.3 Results

4.3.1 Modelling the shear layer roll-up

At $Re = 840$, the plate rotation gives rise to the formation of a primary vortex (Figure 4.2). The vorticity fields at different angular positions are shown in the plate's frame of reference. The primary vortex is the only coherent structure that can be observed and it is connected to the plate tip through a continuous shear layer. No sign of instabilities are observed in the shear layer as the plate continues the rotation. The shear layer remains connected to the primary vortex and rolls-up around its core. As a consequence, the shear layer roll-ups into a spiral that continuously grows in time.

To trace the spiralling topology of the shear layer in the individual snapshots, we start by fitting the Kaden spiral (Equation (4.1)) to the experimental data. At every time instant, the Kaden parameter K is determined such that the spiral passes through the plate's edge when the spiral centre is shifted to the instantaneous location of the primary vortex core. The location of the primary vortex core was retrieved using the dimensionless and Galilean invariant scalar function Γ_2 defined by Graftieaux et al. [51]. The resulting Kaden spirals are presented in Figure 4.3 at three instantaneous vorticity snapshots after a rotation of $\alpha = 105^\circ$ for increasing values of the Reynolds number: $Re = 840, 1955, 8380$. The dashed lines in Figure 4.3 indicate the plate tip trajectory since the start of the motion, the markers indicate the centre location of the primary vortex, and the solid lines are the fitted Kaden spirals. For all three Reynolds numbers, the centre of the primary vortex is located on the plate tip trajectory and the fitted spirals match the rolling up shear layer well based on visual inspection. The vorticity concentration along the shear layer evolves with increasing Reynolds number from a continuous band of vorticity at $Re = 840$ (Figure 4.3a) to an alignment of vorticity lumped into discrete vortices at $Re = 8380$ (Figure 4.3c). At the intermediate Reynolds number $Re = 1955$, the shear layer is undulating and some localised concentrations of high vorticity can be identified along it (Figure 4.3b). These are signs of an unstable shear layer. When we further increase the Reynolds number to 8380, the shear layer instability becomes more prominent. The primary vortex is no longer connected to the plate tip and the shear layer is broken into a series of distinct individual structures that we refer to as secondary vortices (Figure 4.3c). The fit of Kaden's spiral still describes well the unstable shear layer evolution and goes through the secondary vortices for the entire range of Reynolds numbers considered here.

So far, we have merely fitted Equation (4.1) to our experimental data at every time instant, treating Kaden's constant K as a fitting parameter. We observe that the main topology of the roll up is well captured by the Kaden spiral, but we have not yet gained any insight into the temporal evolution of the roll up or the motion of the primary vortex. If our shear layer would follow the time evolution predicted by Kaden's spiral,

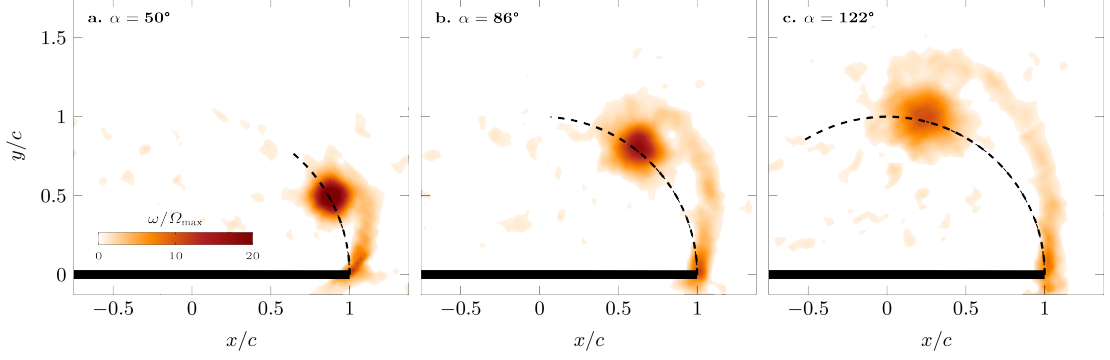


Figure 4.2: Vorticity fields for different angular positions (a) $\alpha = 50^\circ$, (b) $\alpha = 86^\circ$, and (c) $\alpha = 122^\circ$ for $Re = 840$. The dashed line represents the plate tip trajectory.

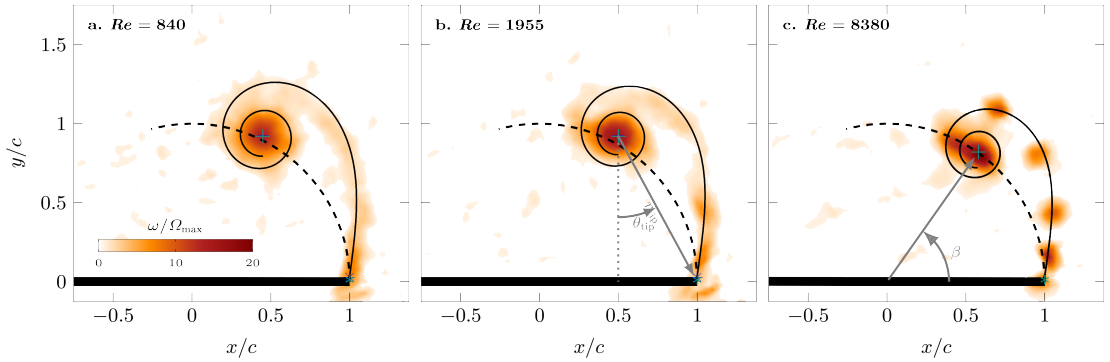


Figure 4.3: Fit of the Kaden's spiral (black solid curve) atop of instantaneous vorticity fields at $\alpha = 105^\circ$ for (a) $Re = 840$, (b) $Re = 1955$, and (c) $Re = 8380$. The marker * indicates the top right edge of the plate and the point where the spiral ends, + indicates the centre of the primary vortex and the point where the spiral begins. The spiral is only plotted for θ ranging from θ_{tip} to 4π . The dashed line represents the plate tip trajectory.

the obtained values for K should be constant for all time instants. Based on the results presented in Figure 4.4, we conclude that K is not a constant value for our data but increases linearly in time for all Reynolds numbers. The rate of increase of K with dimensional time decreases with increasing Re (Figure 4.4a), but all curves collapse when presented in terms of the angular position of the plate (Figure 4.4b). The angular position of the plate serves as the dimensionless time variable. It corresponds to the ratio between the travelled arc length $l = \Omega t c$ and the chord length and represents a convective time scale. The chord length refers to the length between the centre of rotation and the tip of the plate.

Based on these results, we propose here a modified version of the Kaden spiral to describe and predict the temporal evolution of the shear layer roll up:

$$r = \eta \alpha \left(\frac{\alpha}{\theta} \right)^{2/3}, \quad (4.2)$$

where r and θ are again the radial and angular coordinates of the spiral with respect

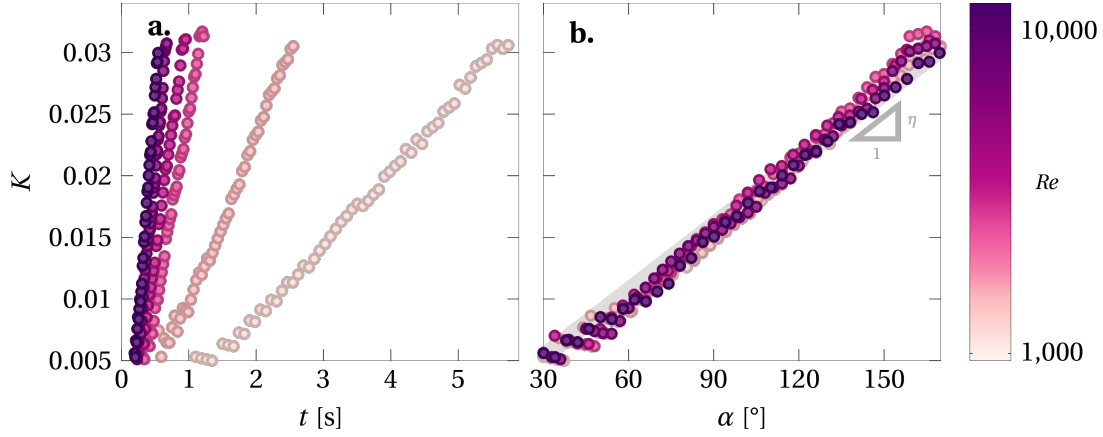


Figure 4.4: K parameter of Kaden's equation as a function of (a) time and (b) angular position of the plate for all the tested Reynolds numbers.

to the spiral centre or primary vortex centre, α is the angular position of the plate and $\eta\alpha$ replaces the dimensional constant K in Kaden's formulation (Equation (4.1)). The value of η is constant for all Re and is empirically determined based on the ensemble of experimental data to $\eta = 1.02 \times 10^{-2}$. The original solution of the Kaden spiral was derived for an unbound semi-infinite vortex sheet that starts out as a straight vortex sheet [69]. The open end of the sheet rolls up into a vortex with the centre at $(r, \theta) = (0, \infty)$ and the other side of the vortex sheet is at infinity $(r, \theta) = (\infty, 0)$. For our experimental conditions, the vortex sheet length is finite and its length increases in time. The open end rolls up into a primary vortex. The bound end of the vortex sheet is attached to the tip of the rotating plate and only the portion of the modified Kaden spiral for $\theta \in [\theta_{\text{tip}}, \infty]$ corresponds to our finite shear layer. Here, θ_{tip} decreases in time and indicates the bound end that is connected to the plate tip. The value of θ_{tip} is determined at every time step based solely on the observation that the primary vortex moves along a path that matches the plate tip trajectory as indicated in Figure 4.2 by the dashed line. Based on this purely geometric constraint, we also directly obtain the radial spiral coordinate where the modified Kaden spiral meets the plate tip, indicated by r_{tip} , and the angular location of the primary vortex with respect to the plate, denoted by β . The detailed derivation of θ_{tip} , r_{tip} , and β is provided in section 4.5.1. With this additional information, we can now write the spatial coordinates of the spiral in the plate's frame of reference as:

$$x_{\text{spiral}} = r \sin \theta + c \cos \beta \quad (4.3)$$

$$y_{\text{spiral}} = -r \cos \theta + c \sin \beta, \quad (4.4)$$

with θ and β defined as indicated in Figure 4.3. This modified version of the Kaden spiral is now a fully predictive model of the shear layer roll-up and the position of the primary vortex core with a single empirical constant η .

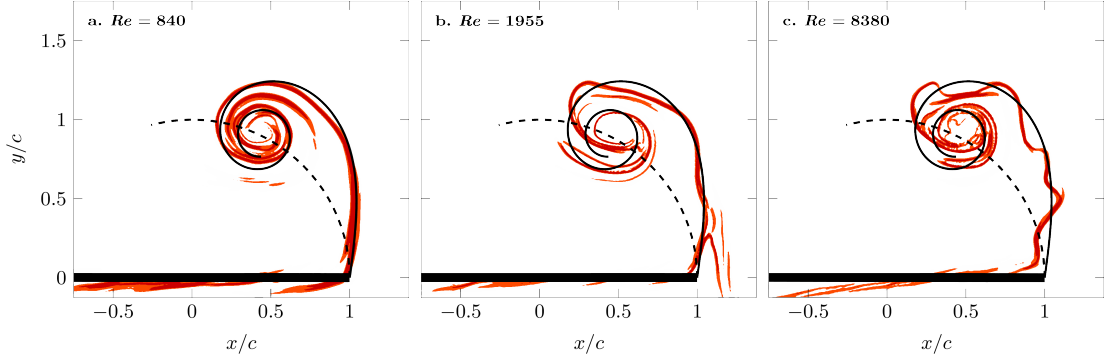


Figure 4.5: Model of the shear layer roll-up (solid curve) atop of nFTLE fields at $\alpha = 105^\circ$ for (a) $Re = 840$, (b) $Re = 1955$, and (c) $Re = 8380$. The spiral is only plotted for θ ranging from θ_{up} to 4π .

4.3.2 Validation of the model

The ability of our modified Kaden spiral to describe the roll-up of the shear layer is visually compared to the negative finite time Lyapunov exponent (nFTLE) fields corresponding to the vorticity fields presented in Figure 4.3a-c. The FTLE is a local measure of Lagrangian stretching of evolving fluid particle trajectories [58, 60]. The maximising ridges of the negative FTLE field indicate regions along which nearby fluid particles are attracted such as the boundaries of coherent structures. The FTLE ridges provide insight into the location and growth of vortices and the flow topology [56, 119].

At $Re = 840$ the shear layer is continuous and the attracting nFTLE ridges appears as a continuous spiral. The shape and the roll-up of the spiral is well described by our predictive model (Figure 4.5a). At $Re = 1955$, we are in a transitional regime where the shear layer is wavy and unstable (Figure 4.3b). This observation is confirmed by the FTLE ridges, where the attracting nFTLE ridge oscillates around our predicted spiral. The deviations become larger where the spiral rolls-up (Figure 4.5b). Finally, at $Re = 8380$ the shear layer is no longer visible in the vorticity field snapshot and we observe discrete secondary vortices instead (Figure 4.3c). The wavelength of the nFTLE ridge fluctuations has decrease with the increase of the Reynolds number towards the discrete shedding regime. The spiral computed with Equation (4.2) represents the middle line along which the FTLE ridge oscillates (Figure 4.5b). We can distinguish four lobes on the outside of the predicted spiral that surround four secondary vortices in Figure 4.3c. With increasing value of the Reynolds number, we can distinguish three regimes: a first regime ($Re < 1500$) which is characterised by a stable shear layer, a transitional regime ($1500 < Re < 2500$) which is characterised by first signs of instability, and a discrete vortex shedding regime ($Re > 2500$) where vorticity is only observed in isolated patches. For the three Re regimes observed, the modified Kaden spiral is able to predict the roll-up of the shear layer and the path of the secondary vortices for the entire rotation of the plate.

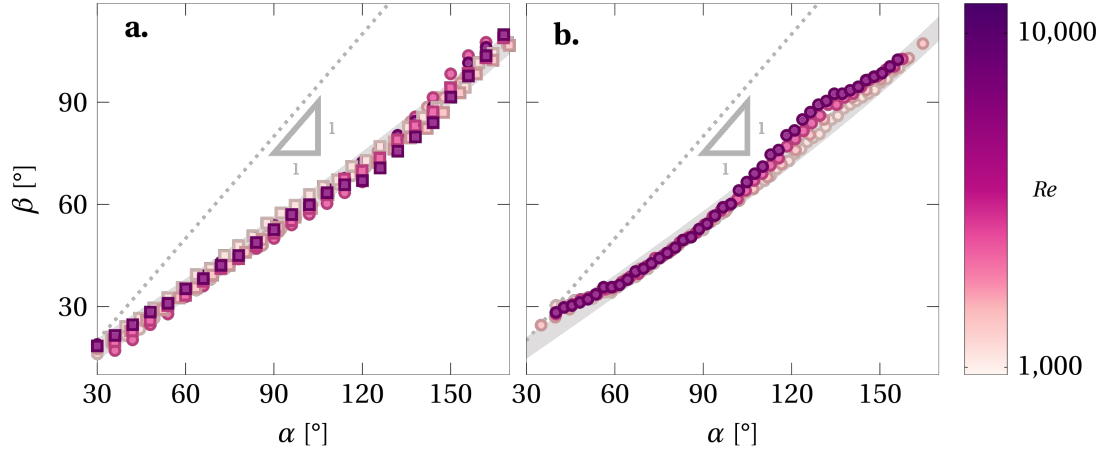


Figure 4.6: Variation of the angular location of the primary vortex (β) with convective time indicated by the plate's rotation angle (α) for (a) rotations around the mid-length and rotations around the edge, both with $c = 4$ cm ; and (b) rotation around the mid-length with $c = 6$ cm.

To further quantitatively validate our modified Kaden spiral model, we compare the measured angular locations of the primary vortex as a function of the convective time α with the predicted model results in Figure 4.6 for different Re . The angular position β of the primary vortex increases with α . The relationship between β and α is close to, but not entirely linear. The trajectory of the primary vortex is completely independent of the Reynolds number and is accurately predicted by the modified Kaden spiral. The trajectory is also not influenced by the total length of the plate. The measured data presented in Figure 4.6a include results from the plates with the rotational location at the mid-length and from the plates with the rotational location at one end of the plate. The distance between the rotational point and the tip is the same in both cases. From the perspective of vortex formation and shear layer roll-up, a plate with a length of 4 cm that rotates around one end is equivalent to a 8 cm long plate rotating around its centre location. The presence of a flipped and mirrored vortex system and shear layer topology on the other side of the longer plate has no influence on the roll-up nor on the trajectory of the primary vortex for the plate geometries and Reynolds numbers tested here.

The influence of the distance between the rotational point and the plate tip, referred to as the chord length here, is analysed by considering a plate with length 12 cm and chord length 6 cm. For rotational motions with the longer plate, we observe the same shear layer topology for the same Re -regimes described before. The modified Kaden spiral predictions still provide an excellent prediction of the shear layer roll-up and the trajectory of the primary vortex in Figure 4.6b. The angular velocity in terms of $d\beta/d\alpha$ is slightly increased for the higher chord length plates and a higher value of $\eta = 1.59 \times 10^{-2}$ was used for the modified Kaden spiral predictions of the larger chord length wing. For the two different chord lengths, the ratio $\eta/c = 0.260 \pm 0.005$. To take

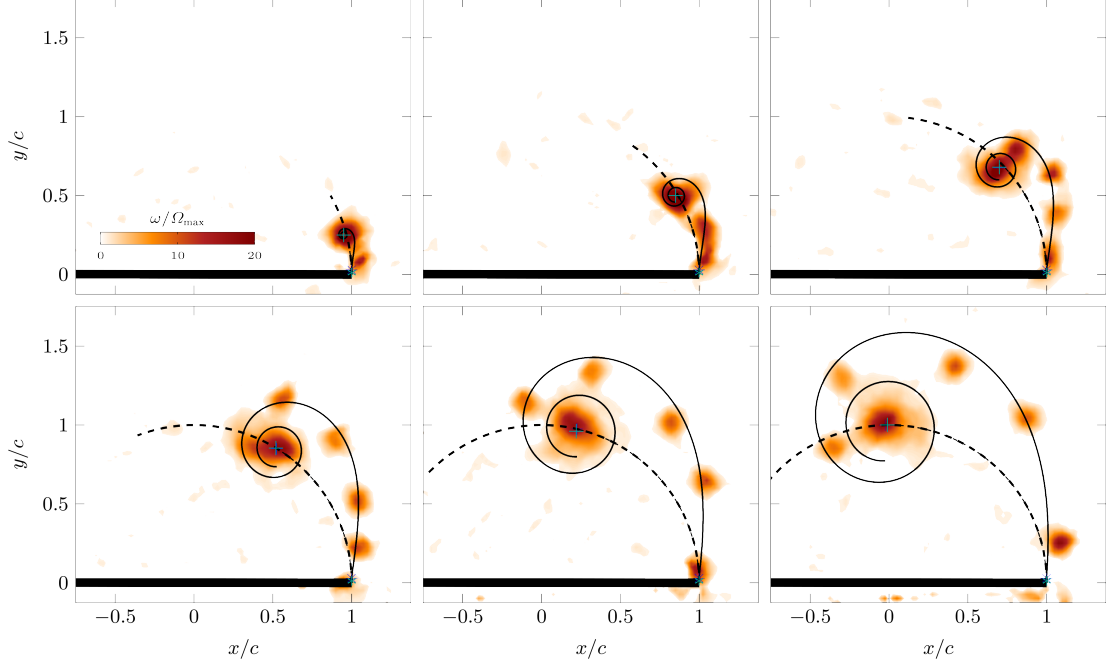


Figure 4.7: Temporal evolution of secondary vortices at different angular positions (a) $\alpha = 30.0^\circ$, (b) $\alpha = 55.7^\circ$, (c) $\alpha = 83.0^\circ$, (d) $\alpha = 110.5^\circ$, (e) $\alpha = 137.7^\circ$, and (f) $\alpha = 160.0^\circ$ for $Re = 8380$. The black curve is the modified Kaden's spiral, whose centre and end are the primary vortex centre (+) and the right top plate edge (*). The spiral is only plotted for θ ranging from θ_{tip} to 4π . The dashed line represents the plate tip trajectory.

into account the influence of the chord length in our modified Kaden spiral model, we replace the empirical constant η in Equation (4.2) with $\eta'c$ to obtain:

$$r = \eta'c\alpha \left(\frac{\alpha}{\theta}\right)^{2/3}, \quad (4.5)$$

where $\eta' = 0.260$ for all data presented in this paper.

4.3.3 Timing of the secondary vortex shedding

In the next part, we focus our attention on the successive shedding of secondary vortices. The first step is to determine if these secondary vortices are generated from the stretching of an initially unstable shear layer or if they are discretely released after the separation of the primary vortex. Figure 4.7 shows the flow topology at different plate angular positions for $Re = 8380$. Between $\alpha = 0^\circ$ and $\alpha = 30^\circ$ the primary vortex centre is close to the plate tip and no secondary vortices are observed. At $\alpha = 30^\circ$, the primary vortex has moved away from the tip along the circular tip trajectory and a first secondary vortex forms (Figure 4.7a). The first secondary vortex drifts towards the primary vortex core and they merge as a consequence of their mutual interaction (Figure 4.7b). The formation and shedding of successive secondary vortices is repeated along the entire

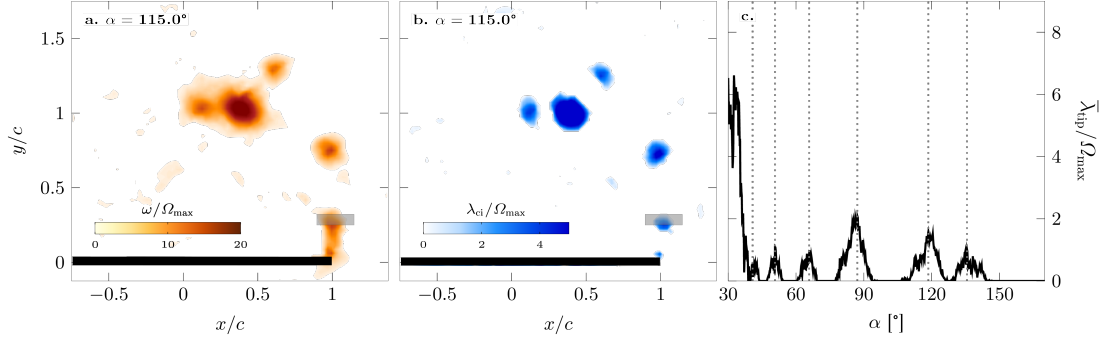


Figure 4.8: Snapshot of the (a) vorticity field and (b) the swirling strength at $\alpha = 115^\circ$ for $Re = 8380$. The black rectangle corresponds to the region in which $\bar{\lambda}_{tip}$ is computed. (c) Evolution of $\bar{\lambda}_{tip}$ as a function of the angular position of the plate. The dotted lines mark the local maxima in the average tip swirling strength. The timing of the local maxima are related to the separation angle of subsequent secondary vortices.

motion. Each vortex is independently formed and subsequently released from the plate tip. In this situation, the shear layer appears as a cloud of vorticity close to the plate tip from which vortices are discretely detached. Once the secondary vortices shed, they move away and are located along the modified time-varying Kaden spiral (Figure 4.7c-e). Vortices closer to the primary vortex deviate slightly from the predicted spiralling curve only when the plate rotation is about to finish (Figure 4.7f).

The second step is to compute the timing of secondary vortices. If we consider the vorticity field, the constant presence of the cloud of vorticity close to the tip hampers the identification of the separation time. To estimate the timing of shedding of the individual vortices we use the swirling strength criterion by Zhou et al. [147]. A vortex is considered a connected region where the value of the swirling strength λ_{ci} is positive. The swirling strength criteria allows us to distinguish more reliably whether a region of high vorticity concentration indicates the presence of a secondary vortex or whether it is due to a strong shear flow (see Figure 4.8a,b). To determine the timing of release of subsequent secondary vortices, we calculate and analysed the evolution of the local average swirling strength, denoted by $\bar{\lambda}_{tip}$, in a small rectangular region close to the tip of the plate. As we are purely interested in the counterclockwise rotating structure here, we only count the positive swirling strength in regions where the vorticity is positive. The location of the probing region is indicated in Figure 4.8a,b and an example of the resulting temporal evolution of the local average tip swirling strength for $Re = 8380$ is presented in Figure 4.8c. The temporal evolution of $\bar{\lambda}_{tip}$ has a global maximum and first peak at $\alpha = 32.6^\circ$ which is followed by six clearly distinguishable smaller peaks. The initial peak corresponds to the shedding of the primary vortex, and the subsequent smaller peaks mark the shedding of individual secondary vortices. The average swirling strength systematically drops to zero in between the individual peaks, further supporting the conclusion that the secondary vortices are discretely released from the tip of the plate. The timing of the local maxima of $\bar{\lambda}_{tip}$ is used to further analyse

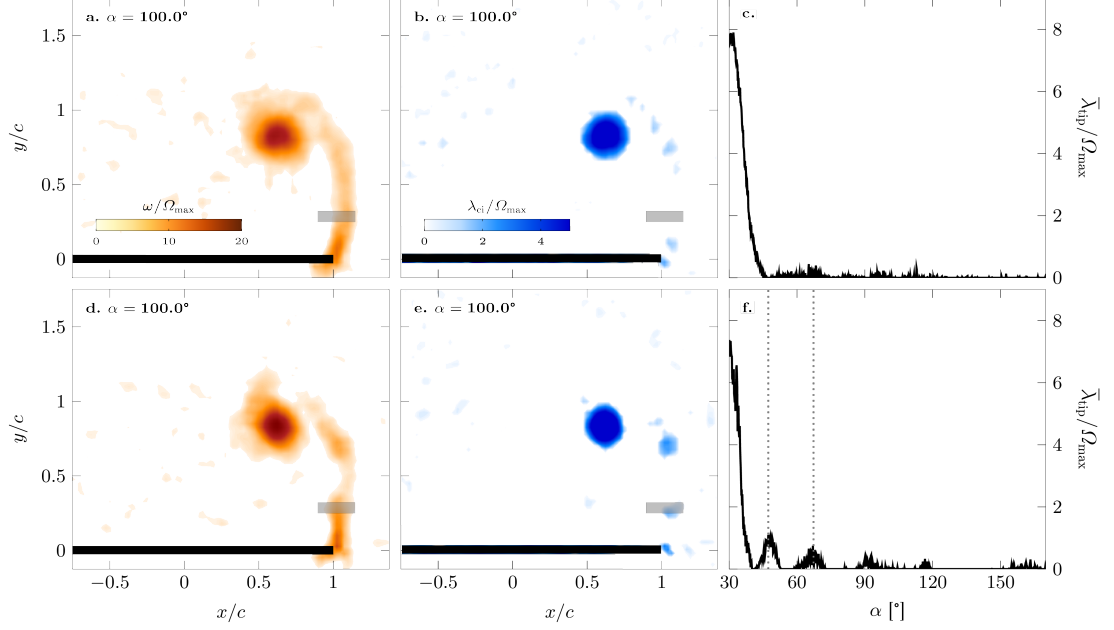


Figure 4.9: Snapshots of the (a,d) vorticity field and (b,e) swirling strength at $\alpha = 100^\circ$ and (c,f) evolution of $\bar{\lambda}_{tip}$ as a function of the angular position of the plate. The first row corresponds to $Re = 840$ at which the shear layer appears continuous. The second row is for $Re = 1955$ at which the shear layer shows signs of instability.

the shedding timing of the secondary vortices. This strategy to determine the timing of secondary vortex shedding is simple yet robust and allows for a systematic and automated extraction of the timings for all measurements. The results depend slightly on the location and size of the probing region which were carefully selected based on a sensitivity analysis (section 4.5.2).

Results of the timing extraction strategy for $Re = 840$ and $Re = 1955$ are summarised in Figure 4.9. For the lowest Reynolds number $Re = 840$, we have a continuous stable shear layer and the associated snapshot of the swirling strength at $\alpha = 100^\circ$ in Figure 4.9a shows a single isolated coherent structure and no sign of secondary vortices. This is confirmed by the time evolution of $\bar{\lambda}_{tip}$ (Figure 4.9c) that exhibits a single peak at $\alpha = 31.9^\circ$. No other peaks are observed afterwards confirming that the shear layer is a continuous layer of fluid without the presence of any instabilities for this Reynolds number. For the intermediate Reynolds number $Re = 1955$, the shear layer topology appeared to be undulating with some localised concentrations of high vorticity along it (Figure 4.3b). The temporal evolution of the average tip swirling strength reveals the shedding of two secondary coherent structures formed after the primary vortex (Figure 4.9b). These two structures are formed and released from the tip and they are not formed afterwards due to the stretching of the shear layer which does not become clear based solely on the vorticity flow topology.

The experiments are repeated five times at each Reynolds number. The separation

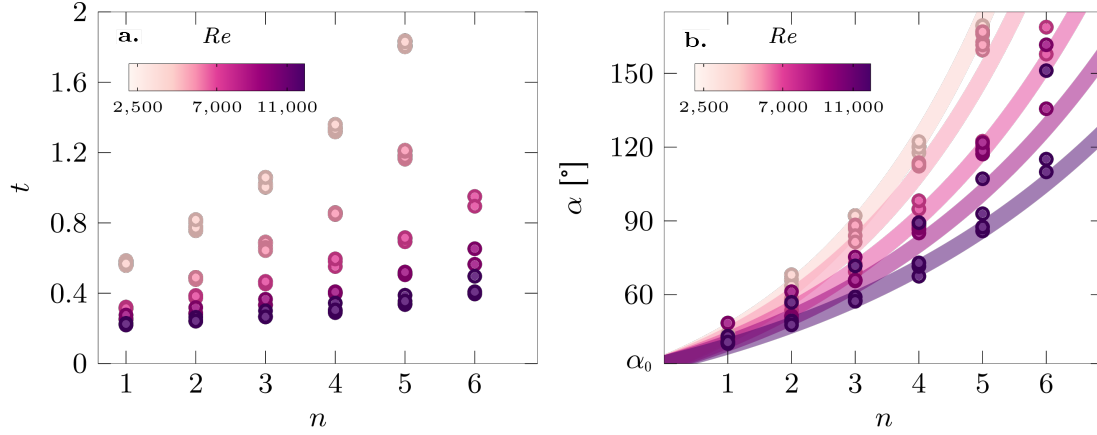


Figure 4.10: Delay between the successive shedding of secondary vortices in terms of (a) dimensional time and (b) convective time or angular distance between secondary vortices as of the shedding order n . The solid lines are the fit of the angular distance between vortices and n .

time and angle of successive secondary vortices are computed and analysed for all experiments with $Re > 2500$ corresponding to the discrete shedding regime. The timing of the secondary vortex shedding versus the number corresponding to the order of successive shedding is presented in Figure 4.10. In general, the time interval between successive vortices increases the more secondary vortices have been released and the time interval decreases with increasing Reynolds number, yielding a larger total number of secondary vortices at the end of the 180° plate rotation. If we hypothesise that the strength of the secondary vortices remains approximately constant, (see chapter 5 for a more detailed discussion about this aspect), then the increase in time interval should be due to a decrease in the circulation feeding rate by the shear layer. This feeding rate is related to the shear rate of at the tip of the plate and can be estimated by:

$$\frac{d\Gamma}{dt} \propto \frac{v_{\text{out}}^2 - v_{\text{in}}^2}{2} \approx \frac{(\Omega c)^2 - v_{\text{in}}^2(t)}{2} \quad (4.6)$$

where v_{out} refers to the velocity at the outer side of the shear layer, which equals the tip velocity Ωc and v_{in} refers to the velocity at the inner side of the shear layer. The velocity at the inner side v_{in} is close to zero during the initial part of the rotation as the plate rotates in a quiescent fluid and increases due to the accumulation of vortex induced velocity components along the direction of the plate's motion. The feeding rate thus decreases when the rotational velocity and the Reynolds number decrease and when the induced velocity due to an increased number of released vortices. This explains the general trends observed in Figure 4.10a,b.

To quantify the evolution of the shedding timing of the secondary vortices, we fit the measured values in Figure 4.10b with a power law in the form:

$$\alpha(n) = \alpha_0(1 + \chi)^n \quad (4.7)$$

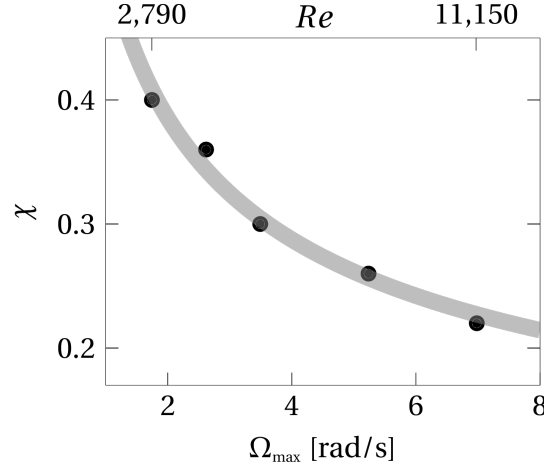


Figure 4.11: Coefficient χ as a function of the maximum rotational speed of the plate. The solid grey line is the power law fit of the experimental points.

where α_0 and χ are fitting constants and n counts the number of secondary vortices. This power law is suitable to represent the timing dynamics for all Reynolds numbers as all fits have a coefficient of determination R^2 -value above 99 %. The parameter α_0 does not significantly change with Re and stays constant around a value of 30 (Figure 4.10b). See next chapter for an in-depth discussion about α_0 . The fitting parameter χ indicates the relative increase in α between the convective timing of successive secondary vortices, i.e. $\alpha_{n+1}/\alpha_n = 1 + \chi$. A higher value of χ indicates a larger delay between successive vortices and a lower total number of vortices shed at the end of the motion. The evolution of χ as a function of the maximum rotational speed is presented in Figure 4.11. The value of χ decreases when the plate rotates faster and yields an increased feeding rate according to Equation (4.6). The solid grey line of Figure 4.11 represents the power law fit that can be expressed as a function of the Reynolds number:

$$\chi = aRe^{-b} \quad (4.8)$$

where Re varies from 2500 to 12 000 in the discrete shedding regime, and the fitting constants are experimentally determined to be $a = 11.7$ and $b = 0.4229$. If we substitute Equation (4.8) into Equation (4.7), we can estimate the angular positions at which secondary vortices separate for various speeds of the plate, i.e Reynolds number Re . For $Re = 1955$ that corresponds to the unstable shear layer regime, we should get secondary vortices at $\alpha = 47.1^\circ, 67.4^\circ, 102.6^\circ, 151.3^\circ$. The first two angular positions correspond to the locations where we observe the two local peaks of the average tip swirling strength in Figure 4.9f. Later than 67.4° , we mostly observe zero values of the average tip swirling strength for $Re = 1955$, expect around 100° and 150° at which we have small non-zero values. This evidence may further suggest that the flow at $Re = 1955$ present secondary vortices that shed from the plate according to Equations (4.7) and (4.8), even if the flow topology resembles an unstable shear layer.

4.4 Summary and conclusion

The roll-up of a shear layer behind a rotating plate in a quiescent fluid is experimentally studied for different rotational velocities or Reynolds numbers. Particular focus was directed towards the formation, trajectory, and timing of secondary vortices.

Based on the time-resolved PIV, we identified three Reynolds number regimes based on the stability of the shear layer. For $Re < 1500$, a stable shear layer in the form of a continuous band of vorticity is observed that rolls up into a single coherent primary vortex. For $Re > 2500$, the shear layer is unstable and secondary vortices are discretely released from the plate's tip during the rotation. In the intermediate regime for $1500 < Re < 2500$, first signs of instability appear. The shear layer is still a continuous band of vorticity but its shape is wavier and localised concentrations of higher vorticity emerge. In all three regimes, the centre of the primary vortex is located on the plate tip trajectory and the shear layer topology matches a spiral shape similar to the roll up of a free shear layer. A modified version of the Kaden spiral is proposed to describe and predict the temporal evolution of the shear layer roll up. The key modification is the replacement of the constant dimensional Kaden constant K by a factor $\eta' c \alpha$ that increases linearly with the rotational angle of the plate and takes into the effect of the chord length. A single value of η' has been empirically determined for all experimental conditions presented in this paper. The proposed modified Kaden spiral model describes the spatiotemporal evolution of the shear layer and accurately predicts the trajectory of the centre of the primary vortex for all Reynolds numbers and different plate dimensions.

The timing of secondary vortices shedding for Reynolds numbers in the discrete shedding regimes is determined using the swirling strength criterion. The swirling strength fields confirm that secondary vortices form directly at the tip of the plate and not further downstream due to the stretching of the shear layer. The separation time of each secondary vortex is identified as a local maximum in the temporal evolution of the average swirling strength close to the plate tip.

The time interval between the release of successive vortices is not constant during the rotation but increases the more secondary vortices have been released. The shedding time interval also increases with decreasing Reynolds number, yielding a lower total number of secondary vortices at the end of the 180° plate rotation for lower Re . The increased time interval under both conditions is due to a reduced circulation feeding rate.

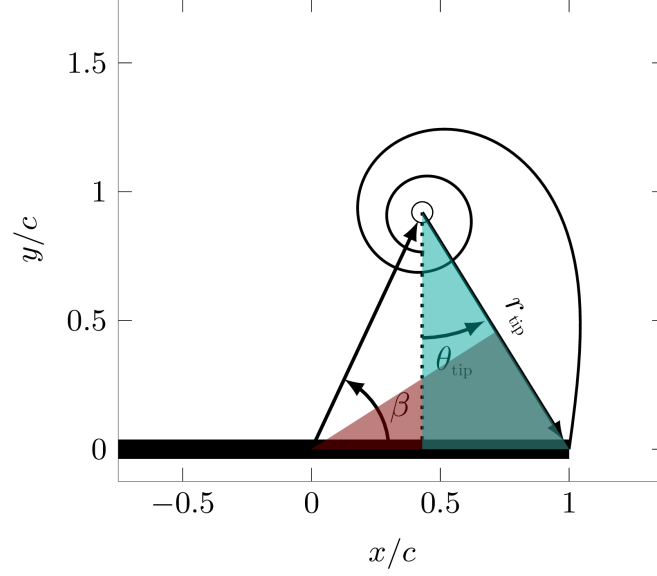


Figure 4.12: Definition of the radial and angular spiral coordinates and its orientation with respect to the plate's frame of reference. The trigonometric relationships Equation (4.9) and Equation (4.10) are obtained in the shaded triangles.

4.5 Appendices

4.5.1 Derivation of the modified Kaden spiral

The modified version of the Kaden spiral we propose takes into account the temporal increase in the distance between the primary vortex and the tip of the plate where the bound end of the vortex sheet is fixed. The angular coordinate along the spiral that marks the bound end of the vortex sheet is denoted by θ_{tip} . The value of θ_{tip} is determined at every time step based solely on the observation that the primary vortex moves along a path that matches the plate tip trajectory. Based on this purely geometric constraint, we also directly obtain the radial spiral coordinate where the modified Kaden spiral meets the plate tip, indicated by r_{tip} , and the angular location of the primary vortex with respect to the plate, denoted by β . Their detailed derivation is given here.

We consider the flow situation after the plate has rotated for a given α in the plates frame of reference in Figure 4.12. The plate tips trajectory is indicated by the dashed line. The primary vortex is located on that circular trajectory. Its angular position with respect to the plate's centre of rotation and tip is indicated by β .

Consider that we have shifted the modified spiral defined by Equation (4.5) such that the spiral centre ($r = 0, \theta \rightarrow \infty$) is located in the centre of the primary vortex. The radial and angular location of the plate tip in the spiral coordinates are given by $(r_{\text{tip}}, \theta_{\text{tip}})$ as indicated in Figure 4.12. For a given spiral form, there is only one solution for β that allows the spiral to go through the plate tip. This solution can be found by ensuring that

the trigonometric relationships for the two triangles outlined in Figure 4.12b are met:

$$\beta = 2 \arcsin(r_{\text{tip}} \cos \theta_{\text{tip}} / 2c) \quad (4.9)$$

$$\beta = \arcsin(r_{\text{tip}} \cos \theta_{\text{tip}} / c) \quad (4.10)$$

The distance between the primary vortex centre and the tip of the plate, r_{tip} , is determined through the modified Kaden spiral (Equation (4.5)), for $\theta = \theta_{\text{tip}}$. In this way, Equation (4.9) and Equation (4.10) are only functions of θ_{tip} , which is computed by equalising the two relationships. For $\beta > \pi/2$, we need to use

$$\beta = \pi - \arcsin(r_{\text{tip}} \cos \theta_{\text{tip}} / c) \quad (4.11)$$

instead of Equation (4.10). Once θ_{tip} is retrieved, we substitute it into Equation (4.9) to obtain the angular position β of the primary vortex. From the value of β , we compute the cartesian coordinates of the primary vortex centre, which corresponds to the centre of our predicted spiral model. The full spiral is finally obtained for every plate angular position α , using Equation (4.3) with $\theta \in [\theta_{\text{tip}}, \infty]$.

4.5.2 Sensitivity analysis of the location and size of the average tip swirling strength probing region

The local average swirling strength $\bar{\lambda}_{\text{tip}}$ reaches a local maximum value when most of the vortex fills the selected rectangular region. If the position and dimension of the rectangular region is not properly set, the identification of the separation time through local peaks loses accuracy. We perform a sensitivity analysis of the best position and dimension of the rectangular region. The first thing to set is the centre of the rectangle. We observed that when the core centre of a secondary vortex is approximately 1 cm above the plate tip, the following secondary vortex starts growing. Since the trajectory of each secondary vortex is predicted by the modified Kaden's spiral (Equation (4.5)), we decide to place the centre of the rectangle along the spiral, 1 cm above the tip. We decided to place it at this distance after we performed a sensitivity analysis on the position of the box. If the box position is above a height of $0.35c$, the first two secondary vortices are not clearly detected in the box (Figure 4.13a). Above $0.35c$ the peak that corresponds to the presence of the primary vortex can not be distinguished from the smaller peaks that correspond to the presence of the first two secondary vortices (Figure 4.13a). On the other side, if the box is too close to the tip of the plate, with the base at a distance lower than $0.12c$ from the tip, the signal is too noisy due to the presence of the constant cloud of vorticity at the tip (Figure 4.13b). We gradually move the box in the range $0.15c < h < 0.35c$ and compute α_0 and χ at each box location, with the aim of evaluating the best location of the box. The influence of the box location on the coefficient of the power law are not significant and the value of α_0 varies from 29.9° to 32.8° when moving the box from $0.15c$ to $0.35c$ (Figure 4.13). The dashed line

marks the location corresponding to $h/c = 0.24$, where we decide to place the box because it is where the computed averaged swirling strength gives the clearest peaks for most of the tested cases. The area of the rectangle has to be large enough to fully include the vortex but it should not include the swirling strength associated with the plate and the other secondary vortices. For the plate chord $c = 4$ cm, a rectangle with a base of $0.25c$ is sufficiently large to include the radial dimension of the secondary vortex and exclude the swirling strength of the plate. A height of $0.15c$ allows to have one secondary vortex at a time in the selected rectangle.

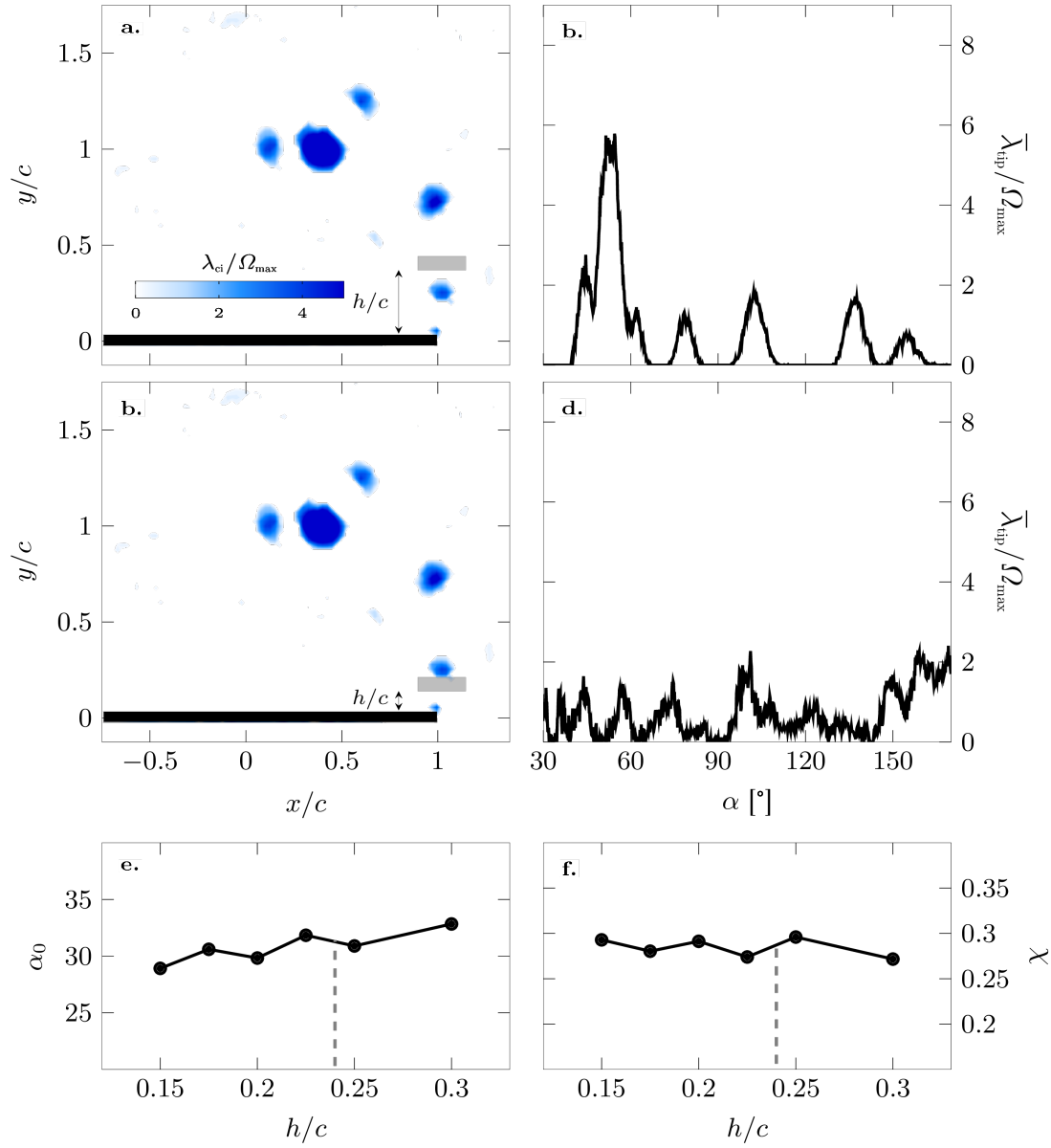


Figure 4.13: Computation of the average swirling strength $\bar{\lambda}_{\text{tip}}$ inside a box placed at (a-b) $h/c = 0.35$ and (c-d) $h/c = 0.15$ from the plate. Coefficients (e) α_0 and (f) χ of Equation (4.6) as a function of the dimensionless vertical distance h/c of the box from the tip of the plate.

Chapter 5

Formation and scaling of primary and secondary vortices

In the previous chapter, we mainly focused on the timing and the trajectory of primary and secondary vortices. This chapter deals with the strength of all vortices shed from the rotating plate. We follow the same structure used to present results in [chapter 4](#). First, we recall the most important studies found in literature about this topic and we clarify the unanswered questions we are going to address. Afterwards, a brief summary of the experimental set-up is given. Look at [chapter 3](#) for further details. The third section is where we describe and discuss the results, trying to give a physical explanation to all of them. Finally, we summarize the take home messages in the conclusion sections.

5.1 Literature studies about the topic

The presence of vortices is ubiquitous and widespread in nature and engineering applications. The formation, growth and shedding of coherent vortical structures becomes predominant when the Reynolds number Re is higher than 10^2 . The vortical structures that form as a result of the interaction between an object and a flow are not all the same. In a wide spectrum of vortex dominated flows, the formation of bigger coherent vortical structures are followed by smaller vortices. We can observe smaller vortices in the trace left by a main vortex when an object, such as a cone or a flat plate, is accelerated from rest ([Figure 5.1a](#)). In this scenario, the smaller vortices roll up into the previously formed bigger vortex, as observed by Grift et al. [57], Rosi and Rival [120]. Bigger and smaller vortices can be also observed in more complex flow configurations. When an airfoil pitches and heaves in a flow stream, a vortex is formed each cycle of the motion. After the vortex is fully formed, we can observe the formation of smaller vortices in the flow region between the primary vortex and the leading edge of the airfoil ([Figure 5.1b](#))

Ayrton [5] first refers to bigger or primary vortices as those structures that attain their full strength during a single period of the motion. Smaller secondary vortices require more than a single period of the motion to form and they can be called residual vortices. The definition of primary vortex is univocal in vortex dominated flow and it refers to the main and first generated coherent vortical structure (see chapter 2). A leading edge vortex that arises from unsteady and revolving motions of an airfoil [33, 99] is a primary vortex. The vortex ring that is generated from the ejection of fluid through a piston-cylinder apparatus [79, 132] or through an orifice [87, 78] is a primary vortex. An object that is accelerated from rest induces a vortex behind it. This vortex, often called a start-up vortex [90, 146, 126, 112], is a primary vortex. The definition of secondary vortices is more ambiguous. Wei and Smith [139] observed a shear layer instability in the near-wake of circular cylinder that rolls up into secondary vortices. These secondary vortices are oriented in the stream-wise direction, perpendicular to the primary Karman vortex that is oriented in the span-wise direction [13]. This phenomenon was previously called transition waves by Bloor [11]. Dabiri [20], Gharib et al. [49] identified secondary vortices in the trailing jet of a primary vortex ring ejected by a piston-cylinder apparatus, like the sketch reported in Figure 5.1c. These secondary vortices are observed after the vortex ring has stopped growing. The additional vorticity rejected by the primary vortex ring forms these secondary vortical structures that are similar to a Kelvin-Helmholtz instability (Figure 2.10e). In the aforementioned cases, secondary vortices do not play any role in the primary vortex separation. Kissing et al. [72] defines secondary vortices as opposite sign vortices that appear between the primary vortex and the airfoil. The primary vortex induces an opposite sign vorticity on the surface of the airfoil. This opposite sign vorticity grows ahead of the main vortex and becomes a secondary vortex. The growth of the secondary vortex interrupts the shear layer to feed the primary vortex. A third vortex is formed between the leading edge shear layer and the secondary vortex. These two structures are called secondary vortices and they are responsible for the primary vortex separation. A similar outline is also observed by Wojcik and Buchholz [143], where secondary vorticity is generated at the surface of the pitching blade. When a primary vortex descends towards an horizontal ground plane, the flow underneath the vortex induces opposite sign vorticity on the ground plane. This bounded vorticity can separate to form one or more discrete secondary vortices that orbit the primary vortex [62, 86]. These secondary vortices have a weaker strength than the primary vortex and induce the primary vortex to rebound from the surface. Here, we refer to secondary vortices as the coherent structures that are shed after the primary vortex but still during the same period of motion and they have the same vorticity sign of the primary vortex. They are discretely shed from the tip of the plate and they do not form as a result of an unsteady shear layer [43]. In our study, secondary vortices are not responsible for the separation of the primary vortex from the shear layer.

Our attention and focus is caught by the difference between primary and secondary vortices, which is unclear yet. The limit strength that the primary vortex can reach is



Figure 5.1: Sketch of primary and secondary vortices detected in the wake of (a) an accelerating flat plate, (b) pitching airfoil and (c) piston-cylinder apparatus.

strongly correlated with the formation number, which is the limiting formation time above which a vortex does not grow anymore. Onoue and Breuer [102] found that the circulation of the leading edge vortex formed from a pitching plate reaches its maximum at a formation number of 3.7 ± 0.3 . A similar value is also found by Ringuette et al. [116] who observed the vortex pinch-off from an accelerating flat plate to occur at a formation number of approximately 4. These values of the formation number are the same order of magnitude as the values found by Gharib et al. [49], Milano and Gharib [93], Ringuette et al. [116], Dabiri [20] for a vortex ring ejected by a piston-cylinder apparatus. However, there is also a consistent amount of works in literature where the formation number is not 4. Dabiri and Gharib [23] delayed the formation number of the vortex ring by varying in time the exit diameter of the piston-cylinder apparatus. Krueger et al. [80] reduced the formation number by putting the piston-cylinder apparatus in a uniform co-flow. Shusser et al. [133] delayed the formation number by constantly accelerating the piston instead of impulsively starting it. These results suggest that depending on the kinematics or the geometry of the vortex generator, the primary vortex needs less or more time to reach its limiting strength, leading the formation time to be different from a hypothetical unique one.

Many works in literature focus only on the shedding frequency of secondary vortices, which depends on the specific flow configuration. Bloor [11] observed that the ratio between the characteristic frequencies of primary and secondary vortices shed in the near-wake of cylinders varies with Reynolds number according to $f_K/f_{SL} = Re^{1/2}$, where f_K and f_{SL} are the shedding frequencies of the primary and secondary vortices. However, there is no consensus about the exponent value of the proposed relationship. Prasad and Williamson [110] indicated that an exponent value of 0.67 works for Re up to 10^5 and Wei and Smith [139] found 0.87 in the range from $Re = 1200$ to 11 000. No clear relationships are established in the situation of an isolated primary vortex. Based on the flow visualisation around a submerged flat plate, Grift et al. [57] determined the shedding frequency of secondary vortices to lie in the range from 13 Hz to 20 Hz, for different values of acceleration, velocity, and immersion depth. This range corresponds

to a Strouhal number around 0.2, according to the plate geometry and kinematics used by the authors. The secondary vortex shedding frequency behind a vertical flat plate increases with increasing acceleration of the flat plate according to Rosi and Rival [120]. Francescangeli and Mulleners [43] found that the shedding timing of secondary vortices behind a rotating plate is not constant during the rotation but increases the more secondary vortices have been released. The onset of secondary vortices is a sign of the primary vortex separation [72, 43] and a more detailed investigation of the size and strength of all secondary vortices is crucial to compare them with the primary vortex features. Harris and Williamson [62] found that the strength of secondary vortices generated as a result of a ground effect with the approaching primary vortex linearly increases with the Reynolds number. They compare the strength of primary and secondary vortices and they showed that for $Re > 3000$ the ratio between the two strengths is Re independent.

A better understanding of the different nature between primary and secondary vortices leads us to study the limiting process of the formation of both primary and secondary vortices. We experimentally study vortices generated from a rectangular flat plate that is rotated around its centre location. We choose to study this configuration because the rotation, together with the translation, is a simple but basic motion. Any two-dimensional motion can be decomposed into a combination of these two. The translation is a widely explored kinematics [26, 38, 120, 105], while there is less information about vortex formation from pure rotating objects. The objective of this paper is to first define the limit formation process of the primary vortex. This implies the detection of the formation time and limit strength of the primary vortex at the moment of pinch-off. Secondly, the same methodology is applied to retrieve the limit strength of secondary vortices. The final goal is to compare the limit values of primary and secondary vortices and explain the differences between them.

5.2 Experimental methods

Here we give a brief description of the experimental set-up used to perform particle image velocimetry (PIV). We also discuss the parameters we change among different experiments and how we processed PIV images. For further details refer to [chapter 3](#).

We rotate a rectangular flat plate about 180° around its centre span-wise axis span-wise axis in an octagonal tank with an outer diameter of 0.75 m filled with water ([Figure 4.1a](#)). The first series of measurements is conducted with a rectangular flat glass plate, with length $l = 8$ cm, width or span $s = 16$ cm and thickness $h = 2$ mm. The distance between the centre of rotation and the tip of the plate is referred to as the chord length c . The thickness of the plate is increased to $h = 4$ mm for the second set of measurements. This allows us to study the influence of the thickness on the formation of vortices. A

third set of measurements with a longer plate with length $l = 12$ cm, yielding a chord length of $c = 6$ cm, was conducted to provide insight into the influence of the chord length on the vortex formation.

The rotation mechanism is fastened to an outer aluminium frame such that the mid span of the plate is in the centre of the tank to limit wall interference effects. The kinematic input is given by a servo motor (Maxon RE 35) connected to a stainless steel shaft and transferred to the flat plate through a 1 : 1 conical coupling. A 1 : 19 gearbox is mounted on the motor to ensure high torque, speed, and acceleration. The rotational angle, speed, and acceleration are controlled via a Galil DMC-40 motion controller, which allows for accurate control of arbitrary motion profiles. The rotation programme is a trapezoidal rotational velocity profile with a fixed rotational amplitude of 180° (Figure 4.1b).

To ensure a continuous acceleration profile, the corners of the velocity trapezoid are smoothed. The maximum rotational speed Ω_{\max} is varied from 30°s^{-1} to 400°s^{-1} . This leads to a Reynolds number $Re = (\Omega_{\max} c^2) / \nu$ ranging from 840 to 11 150. ν is the kinematic viscosity of the water and the chord c is defined as the distance between the rotation point and the tip of the plate. The rotational acceleration $\dot{\Omega}$ is fixed at 6000°s^{-2} .

The PIV images are recorded in the cross-sectional plane at the model mid span. A high-power pulsed light-emitting diode (LED Pulsed System, ILA 5150 GmbH) is used to create a light sheet in the measurement plane. The applicability of high-power LED for PIV has been demonstrated previously by Willert et al. [140], Krishna et al. [76]. Time-resolved PIV images are recorded with a Photron FASTCAM SA-X2 high speed camera. The camera is equipped with a 35 mm Canon lens and the camera is aligned carefully such that the optical axis of the lens is aligned with the rotational axis of the plate and is perpendicular to the light sheet (Figure 4.1a). The frame rate and the exposure time are varied, depending on the dynamics of the motion. A frame rate and exposure time of 250 Hz and 1 ms are selected for a rotational speed of 30°s^{-1} . These values are 2000 Hz and 0.5 ms for the highest tested speeds. The frame rate is high enough to capture the dynamics of the motion and the LED is set to continuous mode. The camera resolution is $1024 \text{ px} \times 1024 \text{ px}$, which corresponds to a field of view of $20 \text{ cm} \times 20 \text{ cm}$. The raw data are processed by the commercial software PIVview (PIVTEC GmbH, ILA 5150 GmbH) using a correlation model based on minimum squared differences and a multi-pass interrogation algorithm with three iterations. The final interrogation window size is $32 \text{ px} \times 32 \text{ px}$ with an overlap of 68 %. A third order B-spline interpolation method for sub-pixel image shifting is performed on all passes. The resulting physical resolution is 1 mm, or $0.025c$ with $c = 4$ cm.

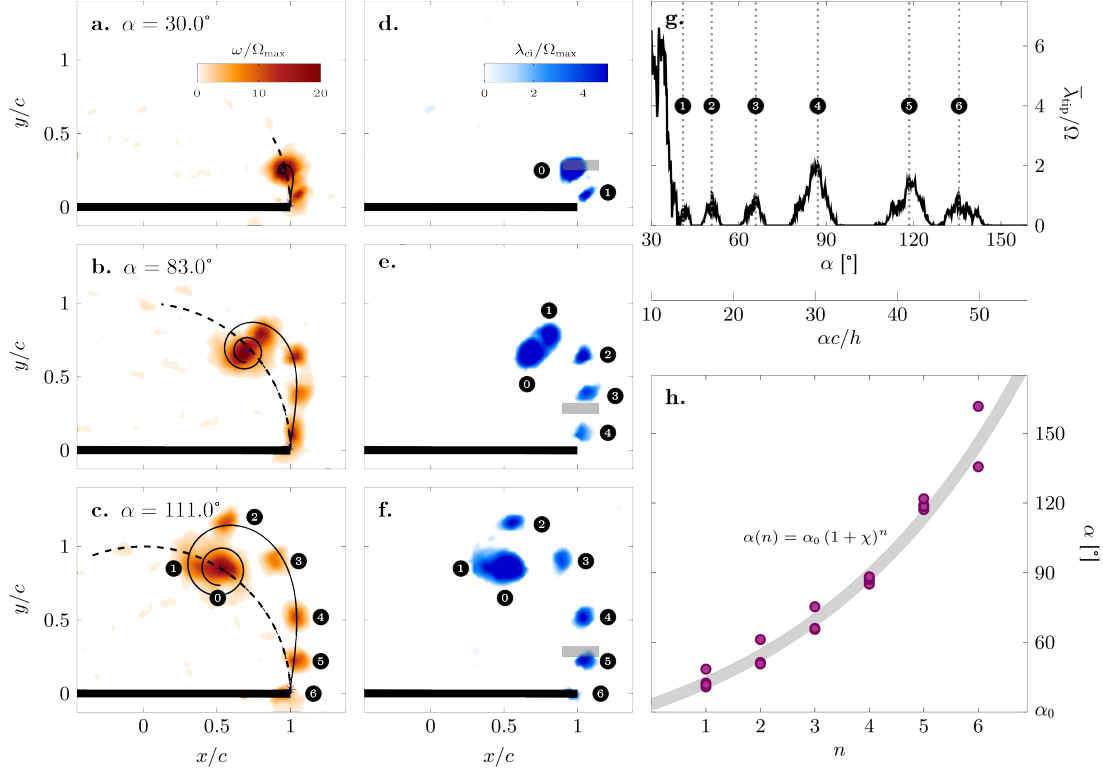


Figure 5.2: Temporal evolution of vorticity and swirling strength λ_{ci} at different angular positions (a,d) $\alpha = 30.0^\circ$, (b,e) $\alpha = 83.0^\circ$ and (c,f) $\alpha = 115.0^\circ$. The black curve is the modified Kaden's spiral defined in Franciscangeli and Mulleners [43]. The dashed line represents the plate tip trajectory. (g) Evolution of $\bar{\lambda}_{tip}$ as a function of the angular position of the plate. The dotted lines mark the separation angle of subsequent secondary vortices. (h) Delay between the successive shedding of secondary vortices as a function of the shedding order n for $Re = 8380$. The solid line is the power law fit.

5.3 Results

What emerged from the previous chapter is that the plate rotation in a range of Reynolds number from 2790 to 11 170 results in the flow topology shown in Figure 5.2a-c. The formation of a bigger primary vortex is followed by the occurrence of smaller secondary vortices that move along a spiralling trajectory. Secondary vortices are discretely released from the plate tip and we refer to this tested range of Reynolds number as the discrete shedding regime [43]. The shedding of the individual secondary vortices is estimated with the swirling strength criterion by Zhou et al. [147]. A vortex is considered a connected region where the value of the swirling strength λ_{ci} is positive (Figure 5.2d-f). The evolution of the local average swirling strength, denoted by $\bar{\lambda}_{tip}$, in a small rectangular region close to the tip of the plate for $Re = 8380$ is presented in Figure 5.2g. The temporal evolution of $\bar{\lambda}_{tip}$ has a global maximum and first peak, followed by six clearly distinguishable smaller peaks. The initial peak corresponds to the primary vortex, and the subsequent smaller peaks mark the shedding of individual secondary vortices. The local maxima of the six smaller peaks identifies the shedding timing of the secondary

vortices expressed in terms of α .

As observed in the previous chapter, secondary vortices are not released with a constant frequency during the rotation but with a timing that follows Equation (4.7). This power law is suitable to represent the timing dynamics for all Reynolds numbers in the discrete regime. The fitting parameter χ is proportional to the ratio α_{n+1}/α_n . The higher the value of χ the longer the plate has to rotate before a new secondary vortex sheds. This parameter depends on the Reynolds number, as shown in Figure 4.10 of the previous chapter. The fitting parameter α_0 corresponds to the angular position at which $n = 0$ (Figure 5.2h). The coefficient α_0 may represent the separation of the primary vortex.

5.3.1 Primary vortex growth and separation

The focus of this section is the growth and subsequent separation of the primary vortex from the rotating plate. The first step of our analysis is to identify the plate's angular position at which the primary vortex is no longer connected with the feeding shear layer. To do so, we investigate how the flow topology evolves when the plate approaches the angular position $\alpha = \alpha_0$. If we consider a Reynolds number of 8380, the fitting constant α_0 is found to be $32^\circ \pm 2^\circ$ (Figure 5.2h). The analysis of the flow topology is performed by computing both positive (pFTLE) and negative finite-time Lyapunov exponent (nFTLE) fields [58, 60] before and after the plate reaches α_0 (Figure 5.3). The ridges in the FTLE fields help identify the boundaries of coherent flow structures and the intersection between the ridges of the positive and negative FTLE fields marks a saddle point. The emergence of saddle points indicates vortex detachment from the plate tip (Mulleners and Raffel [100], Huang and Green [65], Rockwood et al. [119], Krishna et al. [76]). The saddle point closest to the wing tip is marked by circles in Figure 5.3. When the plate is at an angular position $\alpha < \alpha_0$, the negative ridges are barely observable in the flow field (Figure 5.3a). At this stage, no meaningful intersections between positive and negative FTLE ridges are detected. This indicates that the feeding process of the primary vortex is still in progress. At $\alpha = 33^\circ$, the negative ridges are now clearly visible in the flow field (Figure 5.3b). The overlap between positive and negative FTLE fields shows an intersection that defines a saddle point very close to the tip plate. The position of the saddle point (black circle in Figure 5.3b) is exactly along the shear layer that is feeding the primary vortex. This observation shows that at α_0 , the primary vortex pinches-off from the plate tip and is advected downstream. When the plate has surpassed α_0 , the saddle point is still visible in the flow field and it has moved downstream together with the primary vortex (Figure 5.3c).

When the saddle point appears, the vortex separates from the plate tip. This implies that the feeding process from the shear layer to the primary vortex is finished. The growth rate of the primary vortex is quantified through the measure of its circulation in time. To measure the primary vortex circulation, we first need to identify the boundaries. We

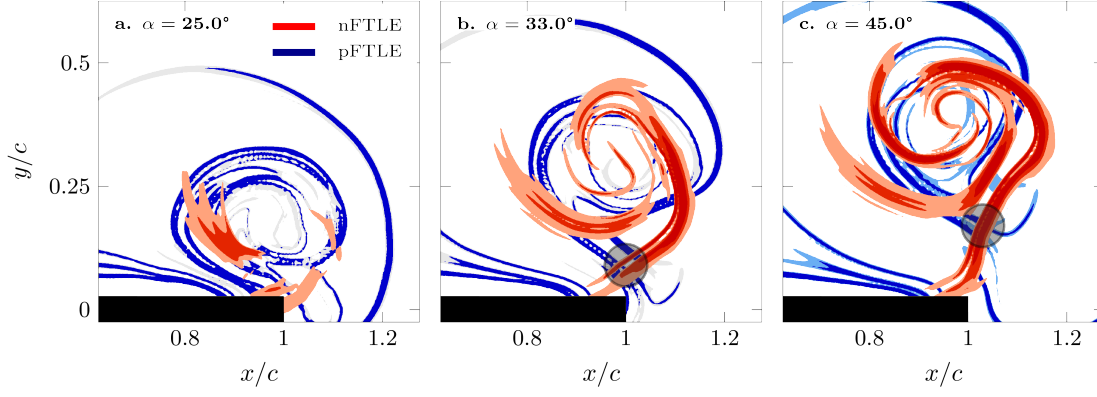


Figure 5.3: Positive and negative FTLE ridges at (a) $\alpha < \alpha_0$, (b) $\alpha = \alpha_0$ and (c) $\alpha > \alpha_0$ for $Re = 8380$. The black circle mark the position of the saddle point.

use both the swirling strength λ_{ci} criterion and the dimensionless Galilean invariant scalar function Γ_2 [51] to identify the boundaries of the primary vortex. The vorticity is integrated inside the vortex contour and we obtain a measure of the primary vortex circulation. In chapter 3 we discuss in details how the circulation is computed and we show the match between the circulation estimated with λ_{ci} and Γ_2 .

We compare the evolution of the primary vortex circulation as a function of α with the total circulation generated by the right side of the plate rotation, for $Re = 4190$ and $Re = 8380$ (Figure 5.4a). For our analysis, the convective time is the angular position of the plate α that corresponds to the ratio between the travelled arc length $l = \Omega t c$ and the chord length c . The chord of the plate is the distance between the rotation point and the tip. The total circulation associated with the positive vorticity released in the flow constantly increases with increasing α . The rate of increase changes during the rotation and is higher at the beginning of the motion. When the plate starts rotating, the primary vortex circulation Γ_0 and the total circulation Γ_{tot} match. When the plate has travelled approximately 32° , the primary vortex circulation does not increase anymore with α while the total circulation keeps increasing. During the feeding process, all the generated circulation is enrolled into the primary vortex. When the vortex pinches-off, the circulation is not entrained in the primary vortex anymore and additional circulation is released in the form of secondary vortices. The primary vortex circulation deviates from the total circulation and reaches the final value of circulation. We measure final values of $0.0032(1) \text{ m}^2 \text{ s}^{-1}$ and $0.0062(2) \text{ m}^2 \text{ s}^{-1}$ for $Re = 4190$ and $Re = 8380$. These values represent the dimensional limit strength of the primary vortex for the two presented Reynolds numbers.

The amount of circulation in the flow field depends on the Reynolds number. The higher the Reynolds number, the higher the total circulation produced. The Reynolds

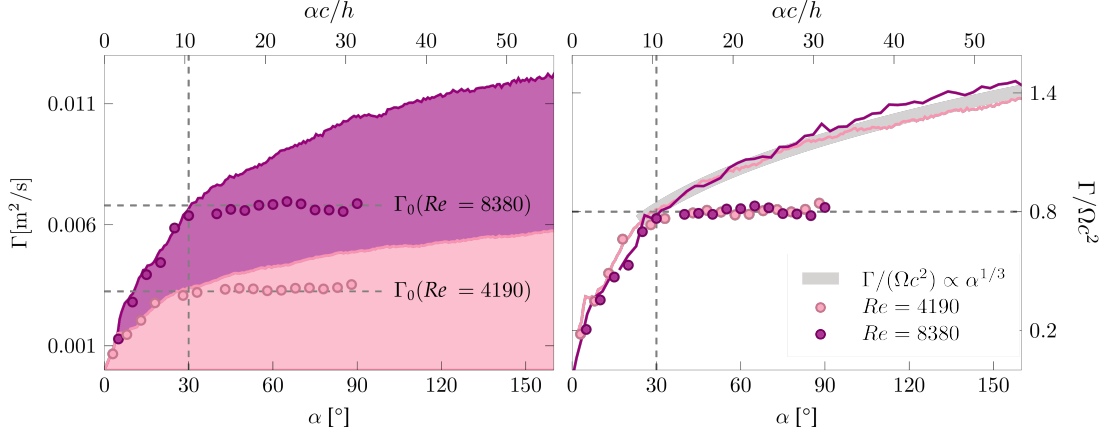


Figure 5.4: (a) Dimensional and (b) dimensionless primary vortex and total circulation for $Re = 4190$ and $Re = 8380$. The solid grey line is the evolution of Γ^* predicted by the inviscid theory.

number is based on the plate rotational velocity and we scale the circulation as follows:

$$\Gamma^*(t) = \frac{\Gamma(t)}{c^2 \Omega(t)} \quad (5.1)$$

where Ω is the value of the rotational speed at each angular position. The acceleration time among all the tested cases is not fixed because the rotational acceleration is kept constant to $6000 \text{ }^\circ \text{s}^{-2}$ and the maximum speed is varied. The choice of the instantaneous value of the speed instead of the maximum rotational speed, allows for a better scaling of the circulation during the acceleration period. For all the tested rotational speeds, the acceleration phase ends when the plate has travelled 24° , a value lower than α_0 . From this angular position, Ω is equal to the maximum rotational speed Ω_{max} . The evolution of the dimensionless total and primary vortex circulation, Γ_{tot}^* and Γ_0^* , as a function of α is not affected by the increase in the Reynolds number from 4190 to 8380 (Figure 5.4b). The match between Γ_{tot}^* and Γ_0^* lasts until 32° , after which Γ_0^* remains constant to 0.79 ± 0.03 for both Re . The angular position at which the primary vortex circulation reaches its maximum value corresponds to the moment at which we observe the occurrence of a saddle point in the field (Figure 5.3b). Both events happen at the same time and within the computed range of $\alpha_0 = 31^\circ \pm 2^\circ$. These observations confirm that α_0 represents the angular position at which the feeding process of the primary vortex ends.

The evolution of α_0 as a function of Re is shown in the box plot of Figure 5.5a. In the tested range, the Reynolds number does not influence much the coefficient α_0 that seems to remain constant around 30° . The only influence of the Reynolds number is a slightly higher uncertainty associated to the measure for $Re > 8000$. If we compute the average $\overline{\alpha_0}$ of the mean values retrieved at each Re , we obtain an angle of 31.4° . We take this angular position as the moment at which the feeding process of the primary vortex ends, for Re ranging from 2500 to 12 000. We experimentally measured the dimensionless

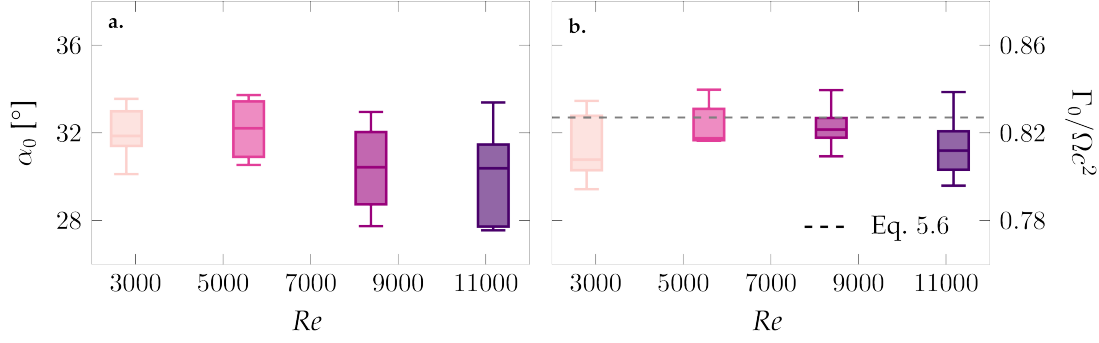


Figure 5.5: (a) Fitting parameter α_0 as a function of the Reynolds number. (b) Dimensionless circulation Γ_0^* of the primary vortex measured at $\bar{\alpha}_0$, as a function of the Reynolds number. The dashed line is the prediction of the primary vortex limit circulation with Equation (5.6).

circulation Γ_0^* of the primary vortex at $\bar{\alpha}_0$ for each Re . The value of Γ_0^* that is enrolled in the primary vortex when the plate approaches $\bar{\alpha}_0$ does not change with Re and stays in a range of 0.81 ± 0.02 (Figure 5.5b). This value represents the limit dimensionless strength Γ_{lim}^* enrolled in the primary vortex.

The next step is to predict the primary vortex growth and limit strength with the inviscid theory by following the analysis made by Pullin [111]. When the plate rotates at a constant speed, we experimentally observe that:

$$\Gamma^* = K\alpha^{\frac{1}{3}} \quad (5.2)$$

where the fitting constant K is experimentally determined to be 1.02 with α expressed in radians. The dimensionless total circulation is proportional to $\alpha^{1/3}$, (solid grey curve in Figure 5.4b), the same dependency shown by Pullin and Sader [113] for a two-dimensional plate moving at a constant speed. This result is also experimentally and numerically confirmed by Xu and Nitsche [146], Rival et al. [118]. We want now to check if the value of the fitting constant K is in agreement with results from inviscid theory. When a flow encounters a wedge of angle β_a , the total circulation released in the flow is given by [111]:

$$\Gamma^* = JC^{\mu} t^{\frac{2(1+\nu_p)}{2-\mu}-1}, \quad C = \left[\frac{(2-\mu)(1-\mu)}{1+\nu_p} \right]^{\frac{1}{2-\mu}} \quad (5.3)$$

where $\mu = \pi/(2\pi - \beta_a)$ and ν_p is a constant that is related to the time exponent m of Equation (2.21) and depends on the flow kinematics (see section 2.2.4). An impulsively started flow corresponds to $\nu_p = 0$. The motion of a flat plate can be modelled as a flow past a wedge of angle $\beta_a = 0^\circ$, which leads to $\mu = 1/2$. The constant J depends weakly on ν_p and is numerically determined by Pullin [111] for a zero wedge angle and several values of ν_p . For the specific case of an impulsively started flat plate, the constant J is

numerically determined to be 2.64 and Equation (5.3) reduces to:

$$\Gamma^* = JC^\mu t^{\frac{1}{3}} \quad C = [(2 - \mu)(1 - \mu)]^{\frac{1}{2-\mu}} \quad (5.4)$$

with $\mu = 1/2$. Then, the dimensionless circulation is $\Gamma^* = 2.3t^{1/3}$ and the proportional constant is approximately double the value of K we determined above. If we consider a constant $k_i = 2.3$, we can relate our experimental constant K with Pullin's constant J computed from inviscid theory:

$$K = \frac{J}{k_i} [(2 - \mu)(1 - \mu)]^{\frac{1}{2-\mu}}, \quad \mu = \frac{1}{2} \quad (5.5)$$

When the plate is at $\alpha < \alpha_0$, the growth of the primary vortex is described by Equations (5.2) and (5.5). At $\alpha = \overline{\alpha}_0$, the vortex does not grow anymore and the limit strength value can be determined as:

$$\Gamma_{lim}^* = \frac{J}{k_i} \overline{\alpha}_0^{\frac{1}{3}} [(2 - \mu)(1 - \mu)]^{\frac{1}{2-\mu}} = 0.83 \quad (5.6)$$

This value is within the uncertainty of the measured dimensionless circulation of the primary vortex at $\overline{\alpha}_0$ in the discrete shedding regime ($2500 < Re < 12000$), as shown in Figure 5.5b.

For Reynolds numbers lower than 2500, we observe a continuous ($Re = 840$) and an unstable ($Re = 1955$) shear layer that connects the tip of the plate to the primary vortex (see Figures 3.6 and 4.3). One may think that the shear layer keeps feeding the primary vortex for a longer convective time than $\overline{\alpha}_0$ at lower Re . This could be a solid hypothesis especially at $Re = 840$, in which the shear layer is continuous and has no sign of instability. We know from experiments that the dimensionless total circulation released in the flow follows Equation (5.2) for all the tested Reynolds ($800 < Re < 12000$). If the shear layer feeds the primary vortex for a longer convective time than $\overline{\alpha}_0$, the primary vortex may reach a higher limit strength at lower Reynolds number. The objective is to evaluate the limit strength of the primary vortex at lower Re . In the discrete shedding regime, the primary vortex reaches its limit strength immediately before the formation of the first secondary vortex. This helped us to reduce the angular range around which we expect the primary vortex separation. At lower Reynolds number, we do not observe any secondary vortices and the identification of the primary vortex separation is trickier. We compute the strength of the primary vortex at $Re = 840$ and $Re = 1955$ for angular positions $\alpha > \overline{\alpha}_0$ (Figure 5.6). The circulation stays constant around a value of 0.82 for both Re . This value is close to Γ_{lim}^* computed in Equation (5.6) and is reached at $\alpha = \overline{\alpha}_0$, because the total shed circulation is still predicted by Equation (5.2) in the range of Re that goes from 800 to 12000. We conclude that the primary vortex reaches the same limit strength at the same angular position in all the three different regimes. This result shows that the limit strength of the primary vortex is not related with the topology of the shear layer. The shear layer

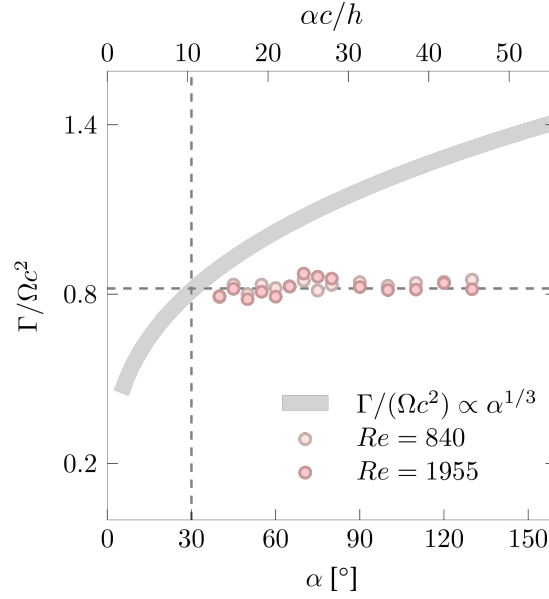


Figure 5.6: Dimensionless primary vortex circulation outside the discrete shedding regime, for $Re = 840$ and $Re = 1955$. The solid grey line is the evolution of Γ^* predicted by the inviscid theory.

does not feed the primary vortex when $\alpha > \bar{\alpha}_0$, even if the shear layer topology appears as a continuous layer of fluid that rolls-up into the primary vortex (Figures 3.6 and 4.3). The main difference is that the circulation released in the flow after the primary vortex separation is entrained into individual coherent secondary structures in the discrete shedding regime. For $800 < Re < 2500$, the circulation is shed from the plate as a shear flow.

5.3.2 Analogy with the piston-cylinder apparatus

We now try to make an interpretation about the vortex separation, based on a kinematic argument. When a vortex ring is ejected from a piston-cylinder apparatus, Mohseni and Gharib [94] proved that the vortex pinches-off from the trailing jet when its velocity ranges from $0.5U$ to $0.6U$, with U being the piston velocity. In this range of speed the vortex ring moves faster than the feeding shear layer. In analogy with the vortex ring, we make the hypothesis that the primary vortex at α_0 is faster than the feeding shear layer.

We estimate the velocity of the primary vortex U_0 based on the results of the previous chapter. The angular position β of the primary vortex with respect to the plate is completely independent of the Reynolds number and increases with the convective time α (Figure 4.6). The relationship between β and α is close to, but not entirely linear

and is well approximated by the following second order polynomial equation:

$$\beta = p_1\alpha^2 + p_2\alpha + p_3 \quad (5.7)$$

where the polynomial coefficients are $p_1 = 0.037$, $p_2 = 0.512$, $p_3 = 0.029$ with α and β expressed in radians. From Equation (5.7), the primary vortex velocity relative to the plate is computed as follows:

$$U_0 = \dot{\beta}c = \Omega c \frac{d\beta}{d\alpha} \quad (5.8)$$

The velocity U_0 is normalized with respect to the maximum velocity $U_p = \Omega_{max}c$ and results are shown in Figure 5.7 for various Re . At the beginning of the motion, the primary vortex speed is between $0.1U_p$ and $0.3U_p$ and the vortex remains close to the plate. During this phase the primary vortex is fed by the shear layer and its speed relative to the plate progressively increases, depending on the acceleration time of the plate. The higher the acceleration time of the plate, the slower the primary vortex moves away from the plate. When the acceleration phase ends, U_0/U_p linearly increases as a function of α with the same slope for all the tested Re . When the plate is at $\overline{\alpha_0}$, the velocity of the primary vortex centre is $0.55U_p$, for all the tested cases. This value is exactly in the middle of the velocity range observed by [94] in which vortex separation occurs. The velocity of the primary vortex centre does not depend on the kinematics of the plate (see chapter 4) and the primary vortex reaches its limit speed at the same angular position, regardless of the Reynolds number. As a consequence, the primary vortex reaches the same final dimensionless strength for all the tested Re . Above the limit speed, the separation from the feeding shear layer is triggered and the primary vortex stops growing.

5.3.3 Primary vortex formation number

The analogy between the primary vortex and the vortex ring ejected from a piston-cylinder apparatus suggests to define a formation number for the primary vortex. Dabiri [20] referred to the vortex formation number \hat{T} as the dimensionless convective time at which the total circulation fed by the vortex generator is equal to the vortex circulation (see section 2.4.2 for further details).

Here, the dimensionless convective time can be defined as l/c or l/h , where $l = \alpha c$ is the arc length travelled by the tip of the plate. To determine which scaling is more appropriate to characterize the age of the primary vortex generated by the rotating plate, we tested two additional plates in the same range of Reynolds number to check how the chord and thickness of the plate influence the primary vortex separation. One plate has the same thickness of the first tested plate, but we increase the chord length from 4 cm to 6 cm. The other plate keeps the same chord length but has a thickness of 4 mm, the double of the first tested plate. For a $Re = 8380$, we compare in Figure 5.8a

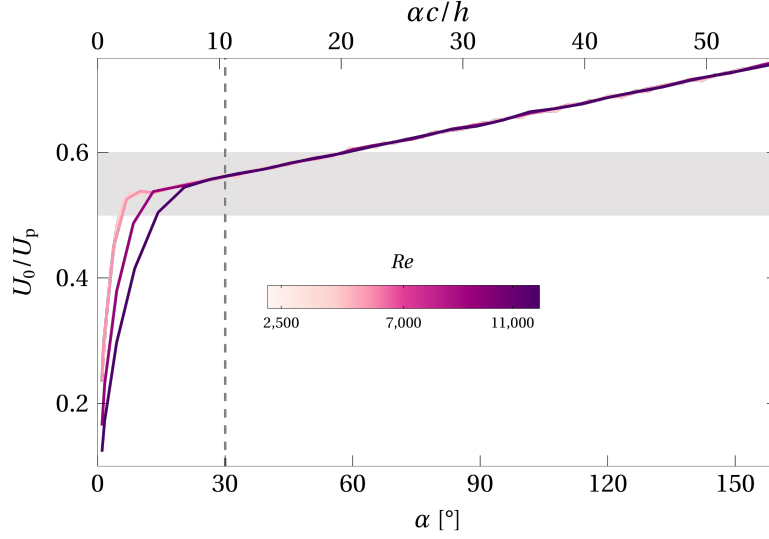


Figure 5.7: Dimensionless velocity of the primary vortex centre as a function of the plate's angular rotation, for various Re . The dashed line identifies the angular position $\bar{\alpha}_0$ and the grey region refers to the velocity range in which Mohseni and Gharib [94] observed the vortex separation.

the dimensionless circulation growth of the primary vortex as a function of α for the three different plates. When the chord of the plate is increased from 4 cm to 6 cm, the primary vortex stops growing at $\alpha = 20^\circ$, which is lower than $\bar{\alpha}_0$. As a consequence, the limit strength of the primary vortex issuing from a 6 cm plate is around 0.7. This value is approximately 13% smaller than the value of the strength measured when the plate has a smaller chord. If we increase the thickness of the plate from 2 mm to 4 mm, the primary vortex growth lasts for a longer time. The circulation stops increasing when the plate reaches an angular position $\alpha = 58^\circ$. The normalized strength reached by the primary vortex is higher compared to the two other plates and is around 1. This result suggests that the dimensions of the plate, in particular the chord and the thickness, influence the growth of the primary vortex. Increasing the chord results in an earlier separation of the primary vortex that entrains a smaller amount of circulation. A bigger thickness delays the separation and the primary vortex entrains a larger amount of circulation.

The scaling of the primary vortex separation requires the definition of a new dimensionless time that takes both thickness and chord into account. We define the following dimensionless time to reach this goal and identify the vortex formation number:

$$T^* = \frac{\alpha c}{h} \quad (5.9)$$

where $l = \alpha c$ is the arc length travelled by the plate and h is the plate thickness. We can describe this dimensionless time as the number of thicknesses h that the plate has to travel along the arc length l before the primary vortex separates. The comparison

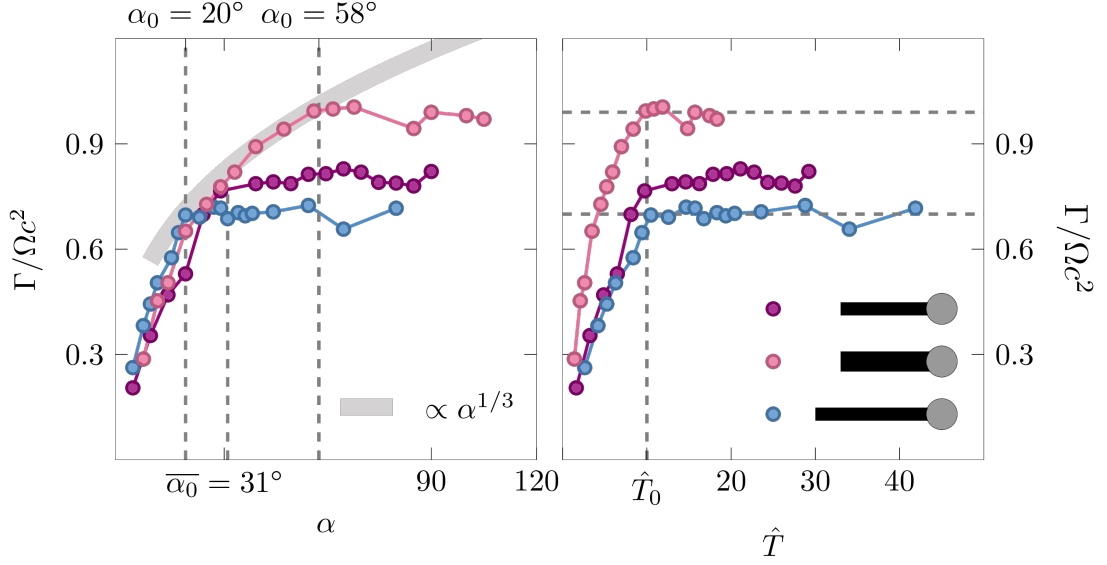


Figure 5.8: Primary vortex circulation for 3 different plate geometries as a function of (a) the plate's angle of rotation and (b) the dimensionless time \hat{T} .

between the dimensionless circulation of the primary vortex generated from the three different plates as a function of the new dimensionless time T^* is shown in Figure 5.8b. Regardless of the dimensions of the plate, the primary vortex stops growing when $T^* \approx 10$. We consider this value the vortex formation number \hat{T} of the primary vortex generated from a rectangular flat plate that rotates with a speed resulting in a Reynolds number range from 840 to 12 000. This result proves that the angular position at which the primary vortex separates is not unique, but given by:

$$\overline{\alpha_0} = \hat{T} \frac{h}{c} \quad (5.10)$$

Increasing the thickness and decreasing the chord lead to a longer growth of the primary vortex. As a consequence, the primary vortex reaches a higher dimensionless limit strength. The considerations about the plate dimensions are valid with an increase of the thickness small enough to still consider the plate thin. If we exceed this range, the thin flat plate becomes a three-dimensional object and the out-of-plane velocity component together with three-dimensional effects cannot be neglected. In the hypothesis of a very long chord length, the primary vortex has no time to grow according to Equation (5.10). On the contrary, the primary vortex does not stop growing if the chord length is really short. This observations are not physically consistent and we cannot prove the validity of Equation (5.10) outside of the range of tested aspect ratios.

The total circulation released in the flow by the thicker and longer plates follows Equation (5.2) (Figure 5.9) and we can still use inviscid theory to predict the limit strength of the primary vortex generated from different plate dimensions. This means that the chord length c is the right characteristic length to scale the total circulation

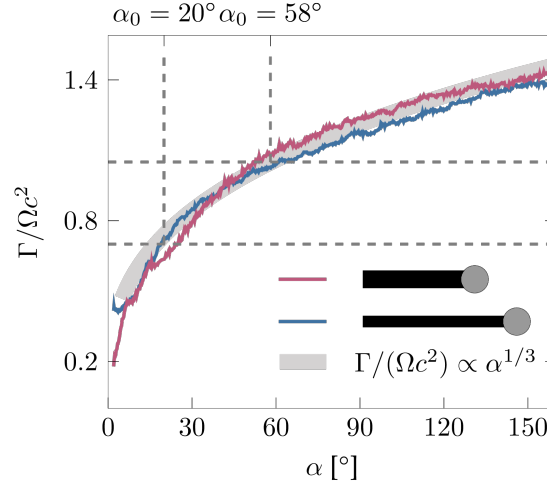


Figure 5.9: Total dimensionless circulation released in the flow from the longer and thicker plates. The solid grey line is the evolution of Γ^* predicted by the inviscid theory and the dashed lines mark the limit strength of the two plates computed from Equation (5.11).

because the fluid particles are first advected along the chord and then entrained into the primary vortex (see Figure 3.4). As a consequence, the dimensionless convective time $\alpha = l/c$ is the right parameter to scale the primary vortex growth (Figure 5.8a). On the contrary, results show that the dimensionless convective time $T^* = l/h$ is the right parameter to scale the age of the primary vortex (Figure 5.8b). The primary vortex pinches-off when the plate has travelled an arc length of approximately 10 times the plate thickness. The thickness of the plate has the same order of magnitude of the width of the feeding shear layer and may explain why the plate thickness is the correct parameter to scale the primary vortex pinch-off. A confirmation of this statement requires a further investigation on the relationship between the plate thickness and the shear layer width.

If we substitute Equation (5.10) into Equation (5.2), we get:

$$\Gamma_{lim}^* = \frac{J}{k_i} \left(\hat{T} \frac{h}{c} \right)^{\frac{1}{3}} [(2 - \mu)(1 - \mu)]^{\frac{1}{2-\mu}} \quad (5.11)$$

This equation gives the limit strength of the primary vortex as a function of the thickness-to-chord ratio. For the thicker plate of 4 cm chord and 4 mm thickness, the limit value is 1.01. For the other plate of 6 cm chord and 2 mm, the maximum strength of the primary vortex is 0.71. The values computed with Equation (5.11) are in agreement with the measured values.

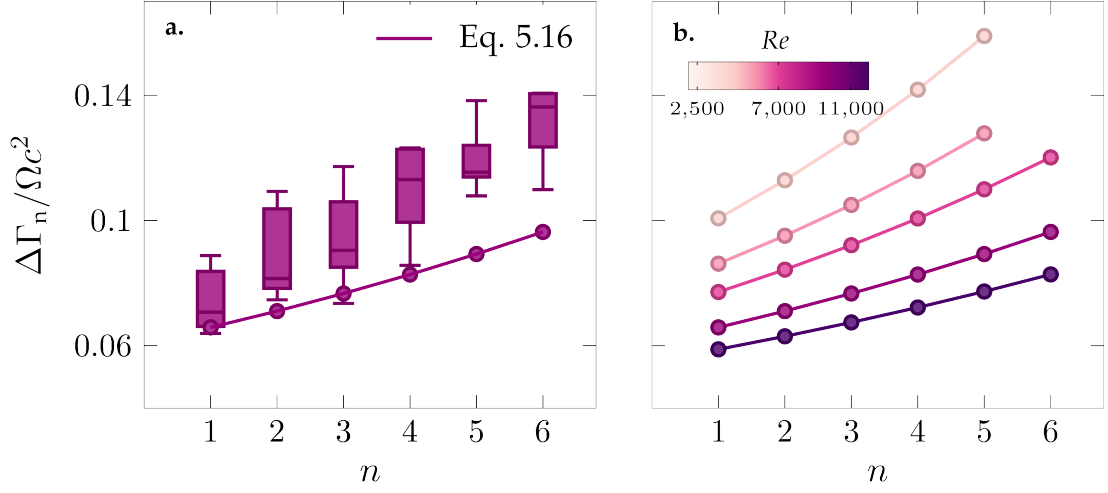


Figure 5.10: (a) Comparison between circulation of all secondary vortices measured with the swirling strength criterion and predicted with the inviscid theory, for $Re = 8380$. (b) Values of circulation computed with Equation (5.16) for all the tested Reynolds number.

5.3.4 Strength of secondary vortices

The last section of the results is dedicated to determine the circulation of secondary vortices. As for the primary vortex, the circulation of each secondary vortex $\Delta\Gamma_n^*$ is measured with the swirling strength criterion when the vortex separates from the plate. See section 4.3.3 and chapter 3 for further details. Figure 5.10a shows $\Delta\Gamma_n^*$ as a function of the shedding order n of secondary vortices for $Re = 8380$ and the plate of 4 cm chord and 2 mm thickness. All secondary vortices have a circulation much smaller than to the primary vortex, within a range that approximately goes from 0.06 to 0.14. The strength of secondary vortices seems to be slightly influenced by the increase of the number n of previously shed vortices. The later the secondary vortex is shed, the higher the circulation we measure.

We use our previous results and inviscid theory to interpret our experimental data and explain how circulation for successive secondary vortices evolves and how the Reynolds number affects secondary vortices strength. We start the analysis from the power law that describes the shedding of secondary vortices:

$$\alpha_n(n) = \overline{\alpha_0}(1 + \chi)^n \quad (5.12)$$

where $\overline{\alpha_0}$ depends on the dimension of the plate through the vortex formation number (Equation (5.10)). We observed from the previous chapter that the parameter χ depends on the Reynolds number (Figure 4.10). The value of χ decreases when the plate rotates faster and we fit the experimental data with the following law:

$$\chi = aRe^{-b} \quad (5.13)$$

where Re varies from 2500 to 12 000 in the discrete shedding regime, and the fitting constants are experimentally determined to be $a = 11.7$ and $b = 0.4229$. The second step we make is to consider the total circulation released in the flow from the plate. When secondary vortices shed, the plate rotates at a constant speed and the circulation increase is proportional to $\alpha^{1/3}$. The limit strength of the primary vortex is given by Equation (5.11) and the total circulation generated from the plate during the shedding of secondary vortices is:

$$\Gamma^* = K \left[\alpha^{\frac{1}{3}} + \left(\hat{T} \frac{h}{c} \right)^{\frac{1}{3}} \right] \quad (5.14)$$

where $\hat{T} = 10.6$ is the primary vortex formation number and the constant K is related with the constant J numerically determined by Pullin [111] through Equation (5.5) and does not change with the plate dimensions. If we substitute Equation (5.12) into Equation (5.14) we get:

$$\Gamma_n^*(n) = K \left(\hat{T} \frac{h}{c} \right)^{\frac{1}{3}} \left[1 + (1 + \chi)^{\frac{n}{3}} \right] \quad (5.15)$$

that represents the total circulation released in the flow at each shedding of a secondary vortex. Let us now consider a generic secondary vortex n shed from the plate at the angular position α_n . We can reasonably assume that the total circulation released in the flow when the plate travels from α_{n-1} , which is the separation angle of the $(n-1)$ _{th} secondary vortex, to α_n is fully entrained into the n _{th} secondary vortex. This observation leads us to calculate the circulation of each secondary vortex as $\Delta\Gamma_n^* = \Gamma_n^* - \Gamma_{n-1}^*$ and if we use Equation (5.15) we obtain:

$$\Delta\Gamma_n^*(n) = K \left(\hat{T} \frac{h}{c} \right)^{\frac{1}{3}} (1 + \chi)^{\frac{n-1}{3}} [(1 + \chi)^{\frac{1}{3}} - 1] \quad (5.16)$$

This equation represents the circulation of each n _{th} secondary vortex in which the dependence on the Reynolds number is inside the parameter χ . We compare circulation values computed from the above equation with measured values in Figure 5.10a, for $Re = 8380$. There are two noteworthy aspects. First, the circulation of all secondary vortices computed with Equation (5.15) is within the uncertainty range of the measured values. This makes our prediction of the secondary vortices strength reasonable. Second, the secondary vortices do not have the same strength. The vortex is stronger the later it is released. This behaviour is even more pronounced at lower Reynolds number, in which the strength difference between two successive secondary vortices is larger than at higher Re (Figure 5.10b). The strength increase of successively released secondary vortices is surprising because the plate rotates at constant speed and the feeding rate decreases as:

$$\frac{d\Gamma}{dt}(\alpha) = \Omega_{max} \frac{d\Gamma}{d\alpha} = \frac{1}{3} K \Omega_{max}^2 c^2 \alpha^{-2/3} \quad (5.17)$$

when these secondary vortices are released. In chapter 4 we made the hypothesis that the strength of secondary vortices is constant and the timing increases to compensate the

decrease of the feeding shear layer. However, these latest results show that the timing also increases to make the strength of successively shed secondary vortices increase. We do not have a convincing physical explanation for such behaviour yet. It seems that focusing solely on the strength of secondary vortices is not enough to have a global picture and an in-depth investigation inside the core of secondary vortices is required. As a future perspective, we would suggest to increase the flow field spatial resolution to values higher than 0.5 mm per grid point. In this way we could capture small-scale phenomena inside the core of secondary vortices that are not observable with our data.

5.4 Summary and conclusions

The growth of primary and secondary vortices, generated from the rotation of a rectangular flat plate in the range of Reynolds number from 840 to 11 170, is experimentally investigated. Particular focus was directed towards the limit process of vortex formation and the identification of the limit strength and formation number of both primary and secondary vortices.

The identification of the limit properties of the primary vortex requires first to determine the pinch-off moment, which is given by the coefficient α_0 of Equation (4.7). Before the separation, the circulation of the primary vortex increases as the plate rotates and matches the total circulation released in the flow. At $\alpha = \alpha_0$ the primary vortex pinches-off and the circulation reaches the maximum value, regardless of the Reynolds number. The Reynolds number does not influence the limit dimensionless strength of the primary vortex and we can use inviscid theory to predict the limit strength, which is in agreement with experimental observations. We also test thicker and longer plates and results show that increasing the thickness and decreasing the chord lead to a longer growth of the primary vortex. As a consequence, the primary vortex reaches a higher dimensionless limit strength. We define a new dimensionless time T^* based on the thickness of the plate to scale the age of the primary vortex. Regardless of the dimensions of the plate, the primary vortex stops growing when $T^* = 10.5$. We consider this value to be the vortex formation number \hat{T} of the primary vortex generated from a rectangular thin flat plate that rotates with a speed resulting in a Reynolds number range from 840 to 12 000. The validity of the defined vortex formation number is limited in the range of the tested plate aspect ratios and further measurements should be performed to extend the range.

When $\alpha > \alpha_0$, the first secondary vortex starts forming. For the rest of the plate rotation, several secondary vortices are shed in the wake. The circulation of all secondary vortices is approximately 4–5 times smaller than the primary vortex one. If we combine with this the timing of secondary vortices defined in Equation (4.7), we can predict the strength of all secondary vortices. The prediction agrees with experimental observations and shows that the strength of successively shed secondary vortices increases. This behaviour is

even more pronounced at lower Reynolds number, in which the strength difference between two successive secondary vortices is larger than at higher Re . This behaviour is interesting because the feeding rate decreases when secondary vortices are released. A possible explanation may be found by looking at the vorticity distribution inside the core of secondary vortices. This requires additional measurements at higher spatial resolution.

Chapter 6

Summary and conclusions

The work presented in this thesis is an experimental characterization of vortices generated in the wake of a rotating plate. Particular focus is directed towards the growth, timing and trajectory of the vortices. We build a rotation mechanism that allows us to rotate a rectangular flat plate in quiescent water. We systematically vary the rotational speed of the plate to check the influence of the plate velocity into the vortex formation. The Reynolds number based on the speed and the chord of the plate varies from 800 to 12 000. We illuminate the mid-section of the plate and we record PIV images. The velocity and vorticity fields of the flow around the plate is computed by processing PIV images. The vorticity field gives a preliminary view of the flow topology as a function of the Reynolds number. For $Re < 1500$, a stable shear layer in the form of a continuous band of vorticity is identified. The continuous shear layer rolls up into a single coherent primary vortex. For $1500 < Re < 2500$, the shear layer still appears as a continuous band of vorticity rolling-up into the primary vortex but its shape is wavier and localised concentrations of higher vorticity emerge. For $Re > 2500$, we observe the occurrence of secondary vortices that are discretely released from the plate's tip during the rotation. The critical Reynolds number for the occurrence of secondary vortices is around 2500.

The velocity field obtained from processing PIV images allows us to compute relevant scalar quantities such as the circulation. The circulation defines the strength of a vortex and requires the identification of the vortex contour to be properly computed. We used Lagrangian and Eulerian techniques to provide an in-depth analysis of how vortex contours evolve in time. The computation of the vortex strength is crucial to quantify the vortex growth. The primary vortex starts forming immediately after the plate is impulsively started. The circulation of the primary vortex increases with the dimensionless convective time, which is the angular position α of the plate, and matches with the total circulation released in the flow. We observe a limit process of the primary vortex growth when a plate of chord $c = 4$ cm and thickness $h = 2$ mm reaches the angular position $\alpha_0 = 30^\circ$, regardless the tested Re . At this angular position the primary vortex has its maximum strength. We also test thicker and longer plates and results show

that increasing the thickness and decreasing the chord lead to a longer growth of the primary vortex. As a consequence, the primary vortex reaches a higher dimensionless limit strength. We define a new dimensionless time T^* based on the thickness of the plate to scale the age of the primary vortex. Regardless of the dimensions of the plate, the primary vortex stops growing when $T^* \approx 10$. We consider this value to be the vortex formation number \hat{T} of the primary vortex generated from a rectangular flat plate that rotates with a speed resulting in a Reynolds number range from 840 to 12 000.

During the entire rotation of the plate, the primary vortex follows the arc travelled by the tip of the plate. The trajectory of the primary vortex remains the same for all Re and tested plates. When $\alpha > \alpha_0$, the circulation released in the flow is entrained into the first secondary vortex for $Re > 2500$. For the rest of the plate rotation, several secondary vortices are shed. The circulation of all secondary vortices is approximately 4–5 times smaller than the primary vortex one. We use the swirling strength criterion to compute the timing of secondary vortices. The separation time of each secondary vortex is identified as a local maximum in the temporal evolution of the average swirling strength close to the plate tip. The time interval between the release of successive vortices is not constant during the rotation but increases the more secondary vortices have been released. The shedding time interval also increases with decreasing Reynolds number, yielding a lower total number of secondary vortices at the end of the 180° plate rotation for lower Re . The increased time interval results in an increase of the strength of successively released secondary vortices. This behaviour is even more pronounced at lower Reynolds number, in which the strength difference between two successive secondary vortices is larger than at higher Re .

Finally, we combined all of these results to predict the growth, the timing and the trajectory of vortices generated behind a rotating plate. We proposed a modified version of the Kaden spiral that accurately describes the spatio-temporal evolution of the shear layer and accurately predicts the trajectory of the centre of the primary vortex for all Reynolds numbers and different plate dimensions. The spiral also represents the path followed by the secondary vortices. Our modified version of the spiral accurately predicts the shear layer evolution and the trajectory of primary and secondary vortices during the entire rotation of the plate. Based on experimental results, the timing dynamics of secondary vortices is well modelled by a power law equation. This equation depends on two distinct parameters: χ and α_0 . The parameter χ indicates the relative increase in α between the convective timing of successive secondary vortices and decreases with increasing Re . A higher value of χ indicates a larger delay between successive vortices and a lower total number of vortices shed at the end of the motion. The parameter α_0 indicates the angular position at which the primary vortex stops growing and pinches-off from the plate. It does not depend on Re . We also observe that the total circulation released in the flow is proportional to $\alpha^{1/3}$, as predicted by the inviscid theory. We combine the power law equation that describes the timing dynamic of primary and secondary vortices with the total circulation computed from

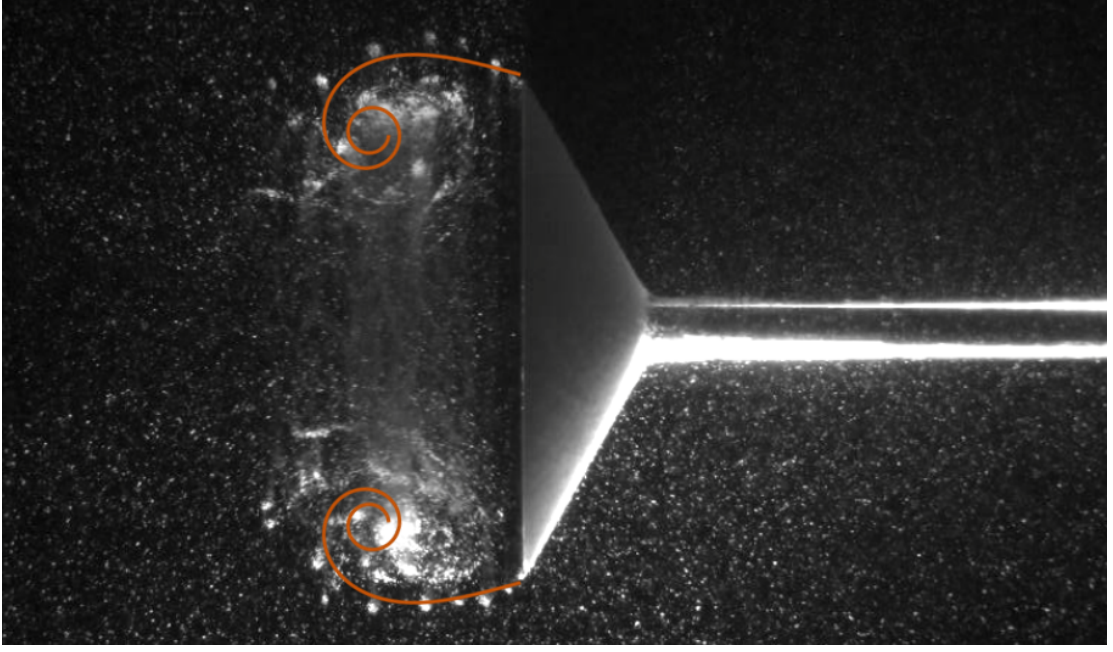


Figure 6.1: Overlap of the modified Kaden's spiral computed from Equation (4.5) in the wake of a translating cone from the experiments of de Guyon and Mulleners [26].

inviscid theory to predict the strength of primary and secondary vortices. The strength prediction is confirmed by experimental measurements.

6.1 Future work and potential applications

The work we presented in this thesis covered the main aspects about the formation of primary and secondary vortices generated behind a rotating plate. This research is only a piece of the puzzle and more work has to be done to extend and improve these results. We investigated the motion of an impulsively started plate with a trapezoidal motion profile. Future work has to be addressed towards the influence of the acceleration into the growth, timing and trajectory of vortices. This is fundamental to further extend the results to more complex kinematics. We determined the timing of secondary vortices as a function of the Reynolds for a single plate dimension. The validity of the power law equation has to be checked for different chord lengths and thicknesses of the plate. This requires to check how χ varies with the thickness of the plate and extend the validity of the formation number \hat{T} for a wider spectrum of plate aspect ratios. Higher spatial resolution PIV images are desirable to provide a more resolved insight in the core of secondary vortices, with the objective to point out small scale phenomena that could explain the increase in strength of successively released secondary vortices. Finally, our model based on the modified Kaden's spiral can be extended and generalized to predict the flow from different object geometries and kinematics (see example in Figure 6.1). This has the potential to describe the shear layer roll-up, trajectory and timing of vortices

generated from several vortex generators by using a relatively simple equation.

We performed a fundamental research about vortex dynamics, which can be used as the basis for several applications. Here, we report a bio-inspired example in which the present investigation can be directly applied. Kashi et al. [70] observed that the emulation of the sea lion propulsion can improve the manoeuvrability of underwater vehicles. A sea lion relies predominantly on its fore-flippers for thrust production. The large flippers move through the water in a clapping motion that ends with each flipper adducted against the animal's torso [44]. This movement generates a downstream jet due to the squeezing of the fluid. Rotating the flipper more quickly produces larger downstream jet velocities that contribute to enhance the produced thrust for high speed manoeuvrers such as escaping or prey capturing [70]. During the clapping phase, the fore-flipper bends due to its flexibility. The clapping motion is similar to an impulsively started rotating plate in a quiescent fluid [29] that experiences a ground effect due to the presence of a nearby solid surface. To mimic the fin clapping motion of a sea lion, we suggest to rotate a flexible flat plate about 90° that ends the rotation in the proximity of a nearby surface. Particle image velocimetry and load measurements of this set-up have the potential to directly correlate the vortex formation with the forces generated on the plate and extend the results presented here to the case of a flexible object in ground effect.

Bibliography

- [1] Y. D. Afanasyev. Formation of vortex dipoles. *Physics of Fluids*, 18(3):037103, Mar. 2006. ISSN 1070-6631, 1089-7666. doi: 10.1063/1.2182006. [Cited on page 33]
- [2] R. C. Alexander. Family of Similarity Flows with Vortex Sheets. *The Physics of Fluids*, 14(2):231–239, Feb. 1971. ISSN 0031-9171. doi: 10.1063/1.1693419. [Cited on pages 13 and 14]
- [3] L. Anton. Ausbildung eines Wirbels an der Kante einer Platte. *Ing. Arch*, 10(6): 411–427, Dec. 1939. ISSN 1432-0681. doi: 10.1007/BF02084978. [Cited on page 20]
- [4] D. Auerbach. Experiments on the trajectory and circulation of the starting vortex. *Journal of Fluid Mechanics*, 183:185–198, Oct. 1987. ISSN 1469-7645, 0022-1120. doi: 10.1017/S0022112087002593. [Cited on pages 40 and 72]
- [5] H. Ayrton. Primary and Secondary Vortices in Oscillating Fluids: Their Connection with Skin Friction. *Proceedings of the Royal Society of London. Series A, Containing Papers of a Mathematical and Physical Character*, 113(763):44–45, 1926. ISSN 0950-1207. [Cited on page 96]
- [6] G. K. Batchelor. Axial flow in trailing line vortices. *Journal of Fluid Mechanics*, 20(4): 645–658, Dec. 1964. ISSN 0022-1120, 1469-7645. doi: 10.1017/S0022112064001446. [Cited on page 65]
- [7] T. B. Benjamin. The alliance of practical and analytical insights into the nonlinear problems of fluid mechanics. In P. Germain and B. Nayroles, editors, *Applications of Methods of Functional Analysis to Problems in Mechanics*, volume 503, pages 8–29. Springer Berlin Heidelberg, Berlin, Heidelberg, 1976. ISBN 978-3-540-07629-2 978-3-540-38165-5. doi: 10.1007/BFb0088744. [Cited on page 30]
- [8] A. Betz. Verhalten von Wirbelsystemen. *Z. angew. Math. Mech.*, 12(3):164–174, 1932. ISSN 00442267, 15214001. doi: 10.1002/zamm.19320120307. [Cited on page 17]
- [9] D. Birch, T. Lee, F. Mokhtarian, and F. Kafyeke. Rollup and Near-Field Behavior of a Tip Vortex. *Journal of Aircraft*, 40(3):603–607, May 2003. ISSN 0021-8669, 1533-3868. doi: 10.2514/2.3137. [Cited on page 77]

- [10] G. Birkhoff. Helmholtz and Taylor instability. In *Proc. Symp. Appl. Math*, volume 13, pages 55–76, 1962. [Cited on page 10]
- [11] M. S. Bloor. The transition to turbulence in the wake of a circular cylinder. *Journal of Fluid Mechanics*, 19(02):290, June 1964. ISSN 0022-1120, 1469-7645. doi: 10.1017/S0022112064000726. [Cited on pages 40, 77, 96, and 97]
- [12] R. J. Bomphrey, G. K. Taylor, and A. L. R. Thomas. Smoke visualization of free-flying bumblebees indicates independent leading-edge vortices on each wing pair. *Exp Fluids*, 46(5):811–821, May 2009. ISSN 1432-1114. doi: 10.1007/s00348-009-0631-8. [Cited on pages 1, 4, and 27]
- [13] M. Brede, H. Eckelmann, and D. Rockwell. On secondary vortices in the cylinder wake. *Physics of Fluids*, 8(8):2117–2124, Aug. 1996. ISSN 1070-6631. doi: 10.1063/1.868986. [Cited on pages 40 and 96]
- [14] J. H. J. Buchholz and A. J. Smits. On the evolution of the wake structure produced by a low-aspect-ratio pitching panel. *Journal of Fluid Mechanics*, 546:433–443, Jan. 2006. ISSN 1469-7645, 0022-1120. doi: 10.1017/S0022112005006865. [Cited on page 4]
- [15] N. A. Buchmann, C. E. Willert, and J. Soria. Pulsed, high-power LED illumination for tomographic particle image velocimetry. *Experiments in Fluids*, 53(5):1545–1560, Nov. 2012. ISSN 0723-4864, 1432-1114. doi: 10.1007/s00348-012-1374-5. [Cited on page 51]
- [16] Z. R. Carr, A. C. DeVoria, and M. J. Ringuette. Aspect-ratio effects on rotating wings: Circulation and forces. *Journal of Fluid Mechanics*, 767:497–525, Mar. 2015. ISSN 0022-1120, 1469-7645. doi: 10.1017/jfm.2015.44. [Cited on page 78]
- [17] M. S. Chong, A. E. Perry, and B. J. Cantwell. A general classification of three-dimensional flow fields. *Physics of Fluids A: Fluid Dynamics*, 2(5):765–777, May 1990. ISSN 0899-8213. doi: 10.1063/1.857730. [Cited on page 57]
- [18] I. Cohen, S. C. Whitehead, and T. Beatus. Fluid dynamics and control of insect flight. *Nat Rev Phys*, 1(11):638–639, Nov. 2019. ISSN 2522-5820. doi: 10.1038/s42254-019-0114-7. [Cited on page 2]
- [19] S. J. Corkery, H. Babinsky, and W. R. Graham. Quantification of added-mass effects using particle image velocimetry data for a translating and rotating flat plate. *Journal of Fluid Mechanics*, 870:492–518, July 2019. ISSN 0022-1120, 1469-7645. doi: 10.1017/jfm.2019.231. [Cited on pages 7, 39, 75, and 78]
- [20] J. O. Dabiri. Optimal Vortex Formation as a Unifying Principle in Biological Propulsion. *Annual Review of Fluid Mechanics*, 41(1):17–33, Jan. 2009. ISSN 0066-4189, 1545-4479. doi: 10.1146/annurev.fluid.010908.165232. [Cited on pages 30, 31, 32, 35, 42, 76, 96, 97, and 107]

- [21] J. O. Dabiri and M. Gharib. Delay of vortex ring pinchoff by an imposed bulk counterflow. *Physics of Fluids*, 16(4):L28–L30, Mar. 2004. ISSN 1070-6631. doi: 10.1063/1.1669353. [Cited on page 33]
- [22] J. O. Dabiri and M. Gharib. The role of optimal vortex formation in biological fluid transport. *Proceedings of the Royal Society B: Biological Sciences*, 272(1572): 1557–1560, Aug. 2005. ISSN 0962-8452, 1471-2954. doi: 10.1098/rspb.2005.3109. [Cited on page 32]
- [23] J. O. Dabiri and M. Gharib. Starting flow through nozzles with temporally variable exit diameter. *Journal of Fluid Mechanics*, 538:111–136, Sept. 2005. ISSN 1469-7645, 0022-1120. doi: 10.1017/S002211200500515X. [Cited on pages 33 and 97]
- [24] J. O. Dabiri, S. P. Colin, K. Katija, and J. H. Costello. A wake-based correlate of swimming performance and foraging behavior in seven co-occurring jellyfish species. *Journal of Experimental Biology*, 213(8):1217–1225, Apr. 2010. ISSN 0022-0949, 1477-9145. doi: 10.1242/jeb.034660. [Cited on page 4]
- [25] M. J. David, M. Mathur, R. N. Govardhan, and J. H. Arakeri. The kinematic genesis of vortex formation due to finite rotation of a plate in still fluid. *Journal of Fluid Mechanics*, 839:489–524, Mar. 2018. ISSN 0022-1120, 1469-7645. doi: 10.1017/jfm.2017.908. [Cited on page 78]
- [26] G. de Guyon and K. Mulleners. Scaling of the translational velocity of vortex rings behind conical objects. *Phys. Rev. Fluids*, 6(2):024701, Feb. 2021. doi: 10.1103/PhysRevFluids.6.024701. [Cited on pages 4, 39, 76, 98, and 117]
- [27] A. C. DeVoria and K. Mohseni. Vortex sheet roll-up revisited. *Journal of Fluid Mechanics*, 855:299–321, Nov. 2018. ISSN 0022-1120, 1469-7645. doi: 10.1017/jfm.2018.663. [Cited on page 76]
- [28] A. C. DeVoria and K. Mohseni. The vortex-entrainment sheet in an inviscid fluid: Theory and separation at a sharp edge. *J. Fluid Mech.*, 866:660–688, May 2019. ISSN 0022-1120, 1469-7645. doi: 10.1017/jfm.2019.134. [Cited on page 11]
- [29] A. C. DeVoria and M. J. Ringuette. Vortex formation and saturation for low-aspect-ratio rotating flat-plate fins. *Exp Fluids*, 52(2):441–462, Feb. 2012. ISSN 1432-1114. doi: 10.1007/s00348-011-1230-z. [Cited on page 118]
- [30] N. Didden. On the formation of vortex rings: Rolling-up and production of circulation. *Journal of Applied Mathematics and Physics (ZAMP)*, 30(1):101–116, Jan. 1979. ISSN 0044-2275, 1420-9039. doi: 10.1007/BF01597484. [Cited on pages 26 and 32]
- [31] J. Eldredge, C. Wang, and M. Ol. A Computational Study of a Canonical Pitch-Up, Pitch-Down Wing Maneuver. In *39th AIAA Fluid Dynamics Conference*, San Antonio, Texas, June 2009. American Institute of Aeronautics and Astronautics. ISBN 978-1-60086-971-6. doi: 10.2514/6.2009-3687. [Cited on page 47]

- [32] J. D. Eldredge. A Reconciliation of Viscous and Inviscid Approaches to Computing Locomotion of Deforming Bodies. *Exp Mech*, 50(9):1349–1353, Nov. 2010. ISSN 1741-2765. doi: 10.1007/s11340-009-9275-0. [Cited on page 7]
- [33] J. D. Eldredge and A. R. Jones. Leading-Edge Vortices: Mechanics and Modeling. page 30, 2018. [Cited on pages 27 and 96]
- [34] V. Elling. Algebraic spiral solutions of 2d incompressible Euler. *arXiv:1308.0881 [math]*, Aug. 2013. [Cited on page 13]
- [35] V. Elling and M. V. Gnann. Variety of unsymmetric multibranched logarithmic vortex spirals. *Eur. J. Appl. Math*, 30(1):23–38, Feb. 2019. ISSN 0956-7925, 1469-4425. doi: 10.1017/S0956792517000365. [Cited on page 14]
- [36] C. P. Ellington, C. van den Berg, A. P. Willmott, and A. L. R. Thomas. Leading-edge vortices in insect flight. *Nature*, 384(6610):626–630, Dec. 1996. ISSN 1476-4687. doi: 10.1038/384626a0. [Cited on pages 3 and 27]
- [37] A. Fage. Laminar Boundary Layers. Edited by L. Rosenhead. Clarendon Press, Oxford. 1963. 687 pp. Illustrated. 90s. *The Aeronautical Journal*, 67(633):604–605, Sept. 1963. ISSN 0368-3931, 2398-4600. doi: 10.1017/S0001924000062485. [Cited on page 6]
- [38] J. N. Fernando and D. E. Rival. On vortex evolution in the wake of axisymmetric and non-axisymmetric low-aspect-ratio accelerating plates. *Physics of Fluids*, 28(1):017102, Jan. 2016. ISSN 1070-6631, 1089-7666. doi: 10.1063/1.4938744. [Cited on pages 4, 75, and 98]
- [39] J. N. Fernando, M. Marzanek, C. Bond, and D. E. Rival. On the separation mechanics of accelerating spheres. *Physics of Fluids*, 29(3):037102, Mar. 2017. ISSN 1070-6631, 1089-7666. doi: 10.1063/1.4977730. [Cited on pages 6 and 75]
- [40] R. Fitzpatrick. *Maxwells Equations and the Principles of Electromagnetism*. Laxmi Publications, Ltd., 2010. [Cited on page 9]
- [41] J. F. Foss. Surface selections and topological constraint evaluations for flow field analyses. *Exp Fluids*, 37(6):883–898, Dec. 2004. ISSN 1432-1114. doi: 10.1007/s00348-004-0877-0. [Cited on page 28]
- [42] L. E. Fraenkel. Examples of steady vortex rings of small cross-section in an ideal fluid. *Journal of Fluid Mechanics*, 51(1):119–135, Jan. 1972. ISSN 1469-7645, 0022-1120. doi: 10.1017/S0022112072001107. [Cited on page 26]
- [43] D. Francescangeli and K. Mulleners. Discrete shedding of secondary vortices along a modified Kaden spiral. *Journal of Fluid Mechanics*, 917, June 2021. ISSN 0022-1120, 1469-7645. doi: 10.1017/jfm.2021.259. [Cited on pages 39, 75, 96, 98, and 100]

-
- [44] C. Friedman and M. C. Leftwich. The kinematics of the California sea lion foreflipper during forward swimming. *Bioinspir. Biomim.*, 9(4):046010, Nov. 2014. ISSN 1748-3190. doi: 10.1088/1748-3182/9/4/046010. [Cited on page 118]
 - [45] M. Gad-el-Hak and R. F. Blackwelder. The discrete vortices from a delta wing. *AIAA Journal*, 23(6):961–962, June 1985. ISSN 0001-1452, 1533-385X. doi: 10.2514/3.9016. [Cited on page 77]
 - [46] L. Gao and S. C. M. Yu. A model for the pinch-off process of the leading vortex ring in a starting jet. *Journal of Fluid Mechanics*, 656:205–222, Aug. 2010. ISSN 0022-1120, 1469-7645. doi: 10.1017/S0022112010001138. [Cited on pages 24, 25, and 76]
 - [47] P. Gehlert. Unsteady Flow and Force Development in the case of a Circular Cylinder. page 164. [Cited on page 8]
 - [48] A. Gehrke and K. Mulleners. Phenomenology and scaling of optimal flapping wing kinematics. *Bioinspir. Biomim.*, 16(2):026016, Mar. 2021. ISSN 1748-3182, 1748-3190. doi: 10.1088/1748-3190/abd012. [Cited on pages 4 and 46]
 - [49] M. Gharib, E. Rambod, and K. Shariff. A universal time scale for vortex ring formation. *Journal of Fluid Mechanics*, 360:121–140, Apr. 1998. ISSN 00221120. doi: 10.1017/S0022112097008410. [Cited on pages 30, 32, 35, 36, 76, 96, and 97]
 - [50] M. Gharib, E. Rambod, A. Kheradvar, D. J. Sahn, and J. O. Dabiri. Optimal vortex formation as an index of cardiac health. *Proc Natl Acad Sci U S A*, 103(16): 6305–6308, Apr. 2006. ISSN 0027-8424. doi: 10.1073/pnas.0600520103. [Cited on page 32]
 - [51] L. Graftieaux, M. Michard, and N. Grosjean. Combining PIV, POD and vortex identification algorithms for the study of unsteady turbulent swirling flows. *Measurement Science and Technology*, 12(9):1422–1429, Sept. 2001. ISSN 0957-0233, 1361-6501. doi: 10.1088/0957-0233/12/9/307. [Cited on pages 27, 58, 59, 80, and 102]
 - [52] W. R. Graham, C. W. P. Ford, and H. Babinsky. An impulse-based approach to estimating forces in unsteady flow. *Journal of Fluid Mechanics*, 815:60–76, Mar. 2017. ISSN 0022-1120, 1469-7645. doi: 10.1017/jfm.2017.45. [Cited on page 7]
 - [53] K. Granlund, B. Monnier, M. Ol, and D. Williams. Airfoil longitudinal gust response in separated vs. attached flows. *Physics of Fluids*, 26(2):027103, Feb. 2014. ISSN 1070-6631, 1089-7666. doi: 10.1063/1.4864338. [Cited on page 33]
 - [54] M. Green. Eulerian and Lagrangian methods for coherent structure analysis in both computational and experimental data. In *51st AIAA Aerospace Sciences Meeting Including the New Horizons Forum and Aerospace Exposition*, Grapevine (Dallas/Ft. Worth Region), Texas, Jan. 2013. American Institute of Aeronautics

- p and Astronautics. ISBN 978-1-62410-181-6. doi: 10.2514/6.2013-629. [Cited on page 57]
- [55] M. Green and A. J. Smits. Effects of three-dimensionality on thrust production by a pitching panel. *J Fluid Mech*, 615:211–220, Nov. 2008. ISSN 0022-1120. doi: 10.1017/S0022112008003583. [Cited on page 4]
- [56] M. A. Green, C. W. Rowley, and G. Haller. Detection of Lagrangian coherent structures in three-dimensional turbulence. *Journal of Fluid Mechanics*, 572:111–120, Feb. 2007. ISSN 1469-7645, 0022-1120. doi: 10.1017/S0022112006003648. [Cited on page 83]
- [57] E. J. Grift, N. B. Vijayaragavan, M. J. Tummers, and J. Westerweel. Drag force on an accelerating submerged plate. *Journal of Fluid Mechanics*, 866:369–398, May 2019. ISSN 0022-1120, 1469-7645. doi: 10.1017/jfm.2019.102. [Cited on pages 40, 77, 95, and 97]
- [58] G. Haller. Distinguished material surfaces and coherent structures in three-dimensional fluid flows. *Physica D: Nonlinear Phenomena*, 149(4):248–277, Mar. 2001. ISSN 0167-2789. doi: 10.1016/S0167-2789(00)00199-8. [Cited on pages 27, 83, and 101]
- [59] G. Haller. An objective definition of a vortex. *Journal of Fluid Mechanics*, 525:1–26, Feb. 2005. ISSN 1469-7645, 0022-1120. doi: 10.1017/S0022112004002526. [Cited on page 59]
- [60] G. Haller. Lagrangian Coherent Structures. *Annual Review of Fluid Mechanics*, 47(1):137–162, Jan. 2015. ISSN 0066-4189, 1545-4479. doi: 10.1146/annurev-fluid-010313-141322. [Cited on pages 60, 83, and 101]
- [61] G. Haller, A. Hadjighasem, M. Farazmand, and F. Huhn. Defining coherent vortices objectively from the vorticity. *Journal of Fluid Mechanics*, 795:136–173, May 2016. ISSN 0022-1120, 1469-7645. doi: 10.1017/jfm.2016.151. [Cited on page 6]
- [62] D. M. Harris and C. H. K. Williamson. Instability of secondary vortices generated by a vortex pair in ground effect. *J. Fluid Mech.*, 700:148–186, June 2012. ISSN 0022-1120, 1469-7645. doi: 10.1017/jfm.2012.108. [Cited on pages 39, 96, and 98]
- [63] L. F. Helmholtz. über integral der hydrodynamischen Gleichungen welche den Wirbelbewegungen entsprechen, journal für reine und angewandte Mathematik. 55. 1858. [Cited on pages 3 and 34]
- [64] E. A. Hendricks, B. D. McNoldy, and W. H. Schubert. Observed Inner-Core Structural Variability in Hurricane Dolly (2008). *Monthly Weather Review*, 140(12): 4066–4077, Dec. 2012. ISSN 0027-0644, 1520-0493. doi: 10.1175/MWR-D-12-00018.1. [Cited on page 1]

- [65] Y. Huang and M. A. Green. Detection and tracking of vortex phenomena using Lagrangian coherent structures. *Experiments in Fluids*, 56(7), July 2015. ISSN 0723-4864, 1432-1114. doi: 10.1007/s00348-015-2001-z. [Cited on pages 60 and 101]
- [66] J. C. R. Hunt. Eddies, streams, and convergence zones in turbulent flows. Dec. 1988. Document ID: 19890015184; Accession Number: 89N24555; Subject Category: FLUID MECHANICS AND HEAT TRANSFER; Publisher Information: United States; Financial Sponsor: NASA; United States; Organization Source: Stanford Univ.; CA, United States; Description: 16p; In English; Original contains color illustrations; Imprint And Other Notes: In its Studying Turbulence Using Numerical Simulation Databases, 2. Proceedings of the 1988 Summer Program p 193-208 [Cited on page 57]
Publication Information: Studying Turbulence Using Numerical Simulation Databases, 2. Proceedings of the 1988 Summer Program; p. p 193-208.
- [67] D. Jeon and M. Gharib. On the relationship between the vortex formation process and cylinder wake vortex patterns. *Journal of Fluid Mechanics*, 519:161–181, Nov. 2004. ISSN 0022-1120, 1469-7645. doi: 10.1017/S0022112004001181. [Cited on pages 6 and 75]
- [68] J. Jeong and F. Hussain. On the identification of a vortex. *Journal of Fluid Mechanics*, 285:69–94, Feb. 1995. ISSN 1469-7645, 0022-1120. doi: 10.1017/S0022112095000462. [Cited on pages 6, 57, and 58]
- [69] H. Kaden. Aufwicklung einer unstabilen Unstetigkeitsfläche. *Ing. Arch*, 2(2): 140–168, May 1931. ISSN 1432-0681. doi: 10.1007/BF02079924. [Cited on pages 14, 75, 76, and 82]
- [70] E. Kashi, A. A. Kulkarni, G. Perrotta, and M. C. Leftwich. Flowfields produced by a robotic sea lion foreflipper starting from rest. *Bioinspir. Biomim.*, 15(3):035002, Mar. 2020. ISSN 1748-3190. doi: 10.1088/1748-3190/ab6a62. [Cited on page 118]
- [71] W. T. B. Kelvin. *Vortex Statics*. Neill, 1878. [Cited on pages 30 and 34]
- [72] J. Kissing, J. Kriegseis, Z. Li, L. Feng, J. Hussong, and C. Tropea. Insights into leading edge vortex formation and detachment on a pitching and plunging flat plate. *Exp Fluids*, 61(9):208, Sept. 2020. ISSN 1432-1114. doi: 10.1007/s00348-020-03034-1. [Cited on pages 39, 96, and 98]
- [73] B. F. Klose, G. B. Jacobs, and M. Serra. Kinematics of Lagrangian Flow Separation in External Aerodynamics. *AIAA Journal*, 58(5):1926–1938, 2020. ISSN 0001-1452. doi: 10.2514/1.J059026. [Cited on page 60]
- [74] P. Koumoutsakos and D. Shiels. Simulations of the viscous flow normal to an impulsively started and uniformly accelerated flat plate. *Journal of Fluid Mechanics*, 328:177–227, Dec. 1996. ISSN 0022-1120, 1469-7645. doi: 10.1017/S0022112096008695. [Cited on pages 24 and 76]

- [75] R. Krasny. Computation of vortex sheet roll-up in the Trefftz plane. *J. Fluid Mech.*, 184:123–155, Nov. 1987. ISSN 0022-1120, 1469-7645. doi: 10.1017/S0022112087002830. [Cited on page 76]
- [76] S. Krishna, M. A. Green, and K. Mulleners. Flowfield and Force Evolution for a Symmetric Hovering Flat-Plate Wing. *AIAA Journal*, 56(4):1360–1371, Jan. 2018. ISSN 0001-1452. doi: 10.2514/1.J056468. [Cited on pages 4, 51, 60, 79, 99, and 101]
- [77] P. S. Krueger. *The Significance of Vortex Ring Formation and Nozzle Exit Over-Pressure to Pulsatile Jet Propulsion*. PhD thesis, California Institute of Technology, 2001. [Cited on page 4]
- [78] P. S. Krueger. Circulation and trajectories of vortex rings formed from tube and orifice openings. *Physica D: Nonlinear Phenomena*, 237(14-17):2218–2222, Aug. 2008. ISSN 01672789. doi: 10.1016/j.physd.2008.01.004. [Cited on page 96]
- [79] P. S. Krueger and M. Gharib. The significance of vortex ring formation to the impulse and thrust of a starting jet. *Physics of Fluids*, 15(5):1271–1281, Apr. 2003. ISSN 1070-6631. doi: 10.1063/1.1564600. [Cited on pages 4 and 96]
- [80] P. S. Krueger, J. O. Dabiri, and M. Gharib. The formation number of vortex rings formed in uniform background co-flow. *Journal of Fluid Mechanics*, 556:147, June 2006. ISSN 0022-1120, 1469-7645. doi: 10.1017/S0022112006009347. [Cited on pages 33 and 97]
- [81] D. Küchemann and J. Weber. Vortex Motions. *Z. angew. Math. Mech.*, 45(7-8): 457–474, 1965. ISSN 00442267, 15214001. doi: 10.1002/zamm.19650450702. [Cited on pages 34 and 36]
- [82] H. Lamb. *Hydrodynamics*. Cambridge University Press, 1932. [Cited on pages 3 and 64]
- [83] J. M. Lawson and J. R. Dawson. The formation of turbulent vortex rings by synthetic jets. *Physics of Fluids*, 25(10):105113, Oct. 2013. ISSN 1070-6631, 1089-7666. doi: 10.1063/1.4825283. [Cited on page 76]
- [84] C. Lepage, T. Leweke, and A. Verga. Spiral shear layers: Roll-up and incipient instability. *Physics of Fluids*, 17(3):031705, Mar. 2005. ISSN 1070-6631. doi: 10.1063/1.1863249. [Cited on pages 21 and 22]
- [85] T. Leweke. FAR-Wake: Fundamental Research on Aircraft Wake Phenomena. In *1st WakeNet3-Europe Workshop on "Wake Turbulence Safety in Future Aircraft Operations"*, Paris-Versailles, France, Jan. 2009. [Cited on pages 42, 72, and 73]
- [86] T. Leweke, S. Le Dizès, and C. H. Williamson. Dynamics and Instabilities of Vortex Pairs. *Annual Review of Fluid Mechanics*, 48(1):507–541, Jan. 2016. ISSN 0066-4189, 1545-4479. doi: 10.1146/annurev-fluid-122414-034558. [Cited on pages 38, 39, 41, 69, and 96]

- [87] R. Limbourg and J. Nedić. An extension to the universal time scale for vortex ring formation. *Journal of Fluid Mechanics*, 915, May 2021. ISSN 0022-1120, 1469-7645. doi: 10.1017/jfm.2021.141. [Cited on pages 32 and 96]
- [88] R. Limbourg and J. Nedić. Formation of an orifice-generated vortex ring. *Journal of Fluid Mechanics*, 913, Apr. 2021. ISSN 0022-1120, 1469-7645. doi: 10.1017/jfm.2021.36. [Cited on page 33]
- [89] P. F. Linden and J. S. Turner. The formation of ‘optimal’ vortex rings, and the efficiency of propulsion devices. *Journal of Fluid Mechanics*, 427:61–72, Jan. 2001. ISSN 00221120. doi: 10.1017/S0022112000002263. [Cited on page 4]
- [90] P. Luchini and R. Tognaccini. The start-up vortex issuing from a semi-infinite flat plate. *Journal of Fluid Mechanics*, 455:175–193, Mar. 2002. ISSN 1469-7645, 0022-1120. doi: 10.1017/S0022112001007340. [Cited on pages 23, 29, 34, 36, 77, and 96]
- [91] E. E. Meshkov. Instability of the interface of two gases accelerated by a shock wave. *Fluid Dyn*, 4(5):101–104, 1972. ISSN 0015-4628, 1573-8507. doi: 10.1007/BF01015969. [Cited on page 37]
- [92] P. Meunier, S. Le Dizès, and T. Leweke. Physics of vortex merging. *Comptes Rendus Physique*, 6(4-5):431–450, May 2005. ISSN 16310705. doi: 10.1016/j.crhy.2005.06.003. [Cited on page 69]
- [93] M. Milano and M. Gharib. Uncovering the physics of flapping flat plates with artificial evolution. *Journal of Fluid Mechanics*, 534:403–409, July 2005. ISSN 1469-7645, 0022-1120. doi: 10.1017/S0022112005004842. [Cited on pages 3, 32, and 97]
- [94] K. Mohseni and M. Gharib. A model for universal time scale of vortex ring formation. *Physics of Fluids*, 10(10):2436–2438, Sept. 1998. ISSN 1070-6631. doi: 10.1063/1.869785. [Cited on pages 30, 33, 76, 106, 107, and 108]
- [95] D. W. Moore. A numerical study of the roll-up of a finite vortex sheet. *Journal of Fluid Mechanics*, 63(2):225–235, Apr. 1974. ISSN 1469-7645, 0022-1120. doi: 10.1017/S002211207400111X. [Cited on pages 15, 16, and 76]
- [96] D. W. Moore and R. Griffith-Jones. The stability of an expanding circular vortex sheet. *Mathematika*, 21(1):128–133, June 1974. ISSN 0025-5793, 2041-7942. doi: 10.1112/S002557930000588X. [Cited on pages 35 and 37]
- [97] D. W. Moore, P. G. Saffman, and K. Stewartson. Axial flow in laminar trailing vortices. *Proceedings of the Royal Society of London. A. Mathematical and Physical Sciences*, 333(1595):491–508, June 1973. doi: 10.1098/rspa.1973.0075. [Cited on pages 16, 18, and 76]

- [98] B. R. Morton. The generation and decay of vorticity. *Geophysical & Astrophysical Fluid Dynamics*, 28(3-4):277–308, Apr. 1984. ISSN 0309-1929, 1029-0419. doi: 10.1080/03091928408230368. [Cited on page 6]
- [99] F. T. Muijres, L. C. Johansson, R. Barfield, M. Wolf, G. R. Spedding, and A. Hedenström. Leading-Edge Vortex Improves Lift in Slow-Flying Bats. *Science*, 319(5867): 1250–1253, Feb. 2008. doi: 10.1126/science.1153019. [Cited on pages 1 and 96]
- [100] K. Mulleners and M. Raffel. The onset of dynamic stall revisited. *Experiments in Fluids*, 52(3):779–793, Mar. 2012. ISSN 0723-4864, 1432-1114. doi: 10.1007/s00348-011-1118-y. [Cited on pages 3, 27, 31, 60, and 101]
- [101] J. Norbury. A family of steady vortex rings. *Journal of Fluid Mechanics*, 57(3): 417–431, Feb. 1973. ISSN 1469-7645, 0022-1120. doi: 10.1017/S0022112073001266. [Cited on page 26]
- [102] K. Onoue and K. S. Breuer. Vortex formation and shedding from a cyber-physical pitching plate. *Journal of Fluid Mechanics*, 793:229–247, Apr. 2016. ISSN 0022-1120, 1469-7645. doi: 10.1017/jfm.2016.134. [Cited on pages 4 and 97]
- [103] K. Onoue and K. S. Breuer. A scaling for vortex formation on swept and unswept pitching wings. *Journal of Fluid Mechanics*, 832:697–720, Dec. 2017. ISSN 0022-1120, 1469-7645. doi: 10.1017/jfm.2017.710. [Cited on pages 27, 32, and 33]
- [104] C. Oseen. Hydromechanik. *Leipzig: Akademische*, 1912. [Cited on page 64]
- [105] F. Paraz, L. Schouveiler, and C. Eloy. Thrust generation by a heaving flexible foil: Resonance, nonlinearities, and optimality. *Physics of Fluids*, 28(1):011903, Jan. 2016. ISSN 1070-6631. doi: 10.1063/1.4939499. [Cited on pages 4 and 98]
- [106] G. Pedrizzetti. Vortex formation out of two-dimensional orifices. *Journal of Fluid Mechanics*, 655:198–216, July 2010. ISSN 1469-7645, 0022-1120. doi: 10.1017/S0022112010000844. [Cited on pages 33 and 35]
- [107] V. J. Peridier, F. T. Smith, and J. D. A. Walker. Vortex-induced boundary-layer separation. Part 1. The unsteady limit problem $Re \rightarrow \infty$. *Journal of Fluid Mechanics*, 232: 99–131, Nov. 1991. ISSN 1469-7645, 0022-1120. doi: 10.1017/S0022112091003646. [Cited on page 31]
- [108] L. Prandtl. über Flüssigkeitsbewegung bei sehr kleiner Reibung. *Verhandl. III, Internat. Math.-Kong., Heidelberg, Teubner, Leipzig, 1904*, pages 484–491, 1904. [Cited on pages 3, 12, and 34]
- [109] L. Prandtl. Über die Entstehung von Wirbeln in der idealen Flüssigkeit, mit Anwendung auf die Tragflügeltheorie und andere Aufgaben. In T. v. Kármán and T. Levi-Civita, editors, *Vorträge aus dem Gebiete der Hydro- und Aerodynamik (Innsbruck 1922)*, pages 18–33. Springer, Berlin, Heidelberg, 1922. ISBN 978-3-662-00280-3. doi: 10.1007/978-3-662-00280-3_2. [Cited on pages 12, 13, and 42]

- [110] A. Prasad and C. H. K. Williamson. The instability of the shear layer separating from a bluff body. *Journal of Fluid Mechanics*, 333:375–402, Feb. 1997. ISSN 0022-1120, 1469-7645. doi: 10.1017/S0022112096004326. [Cited on pages 40, 77, and 97]
- [111] D. I. Pullin. The large-scale structure of unsteady self-similar rolled-up vortex sheets. *Journal of Fluid Mechanics*, 88(3):401–430, Oct. 1978. ISSN 0022-1120, 1469-7645. doi: 10.1017/S0022112078002189. [Cited on pages 17, 18, 20, 21, 24, 42, 76, 104, and 112]
- [112] D. I. Pullin and A. E. Perry. Some flow visualization experiments on the starting vortex. *Journal of Fluid Mechanics*, 97(2):239–255, Mar. 1980. ISSN 1469-7645, 0022-1120. doi: 10.1017/S0022112080002546. [Cited on pages 20, 21, 22, 35, 77, and 96]
- [113] D. I. Pullin and J. E. Sader. On the starting vortex generated by a translating and rotating flat plate. *Journal of Fluid Mechanics*, 906, Jan. 2021. ISSN 0022-1120, 1469-7645. doi: 10.1017/jfm.2020.762. [Cited on pages 21, 22, 23, and 104]
- [114] M. Raffel, editor. *Particle Image Velocimetry: A Practical Guide*. Springer, Heidelberg ; New York, 2nd ed edition, 2007. ISBN 978-3-540-72307-3. [Cited on pages 3 and 51]
- [115] R. D. Richtmyer. Taylor instability in shock acceleration of compressible fluids. *Comm. Pure Appl. Math.*, 13(2):297–319, May 1960. ISSN 00103640, 10970312. doi: 10.1002/cpa.3160130207. [Cited on page 37]
- [116] M. J. Ringuette, M. Milano, and M. Gharib. Role of the tip vortex in the force generation of low-aspect-ratio normal flat plates. *Journal of Fluid Mechanics*, 581: 453–468, June 2007. ISSN 1469-7645, 0022-1120. doi: 10.1017/S0022112007005976. [Cited on pages 32 and 97]
- [117] D. Rival, T. Prangemeier, and C. Tropea. The influence of airfoil kinematics on the formation of leading-edge vortices in bio-inspired flight. In G. K. Taylor, M. S. Triantafyllou, and C. Tropea, editors, *Animal Locomotion*, pages 261–271. Springer, Berlin, Heidelberg, 2010. ISBN 978-3-642-11633-9. doi: 10.1007/978-3-642-11633-9_21. [Cited on page 32]
- [118] D. E. Rival, J. Kriegseis, P. Schaub, A. Widmann, and C. Tropea. Characteristic length scales for vortex detachment on plunging profiles with varying leading-edge geometry. *Experiments in Fluids*, 55(1), Jan. 2014. ISSN 0723-4864, 1432-1114. doi: 10.1007/s00348-013-1660-x. [Cited on pages 28, 31, and 104]
- [119] M. P. Rockwood, K. Taira, and M. A. Green. Detecting Vortex Formation and Shedding in Cylinder Wakes Using Lagrangian Coherent Structures. *AIAA Journal*, 55(1):15–23, 2017. ISSN 0001-1452. doi: 10.2514/1.J055051. [Cited on pages 60, 83, and 101]

- [120] G. A. Rosi and D. E. Rival. Entrainment and topology of accelerating shear layers. *Journal of Fluid Mechanics*, 811:37–50, Jan. 2017. ISSN 0022-1120, 1469-7645. doi: 10.1017/jfm.2016.716. [Cited on pages 4, 24, 40, 75, 77, 95, and 98]
- [121] N. Rott. Diffraction of a weak shock with vortex generation. *Journal of Fluid Mechanics*, 1(1):111–128, May 1956. ISSN 1469-7645, 0022-1120. doi: 10.1017/S0022112056000081. [Cited on pages 10 and 20]
- [122] S. C. Crow. Stability theory for a pair of trailing vortices. *AIAA Journal*, 8(12): 2172–2179, 1970. ISSN 0001-1452. doi: 10.2514/3.6083. [Cited on page 38]
- [123] P. G. Saffman. The structure and decay of trailing vortices. page 17. [Cited on page 35]
- [124] P. G. Saffman. The Velocity of Viscous Vortex Rings. *Studies in Applied Mathematics*, 49(4):371–380, 1970. ISSN 1467-9590. doi: 10.1002/sapm1970494371. [Cited on page 31]
- [125] P. G. Saffman. *Vortex Dynamics*, volume 1 of *Cambridge Monographs on Mechanics and Applied Mathematics*. Cambridge University Press, Cambridge ; New York, 1st pbk. ed. with corrections edition, 1995. ISBN 978-0-521-47739-0. [Cited on pages 10, 12, 14, 15, 17, 20, 23, 35, 38, and 76]
- [126] P. Sattari, D. E. Rival, R. J. Martinuzzi, and C. Tropea. Growth and separation of a start-up vortex from a two-dimensional shear layer. *Physics of Fluids*, 24(10): 107102, Oct. 2012. ISSN 1070-6631, 1089-7666. doi: 10.1063/1.4758793. [Cited on pages 30, 76, and 96]
- [127] S. B. Savage, B. G. Newman, and D. T.-M. Wong. The Role of Vortices and Unsteady Effects During the Hovering Flight of Dragonflies. *Journal of Experimental Biology*, 83(1):59–77, Dec. 1979. ISSN 0022-0949, 1477-9145. [Cited on page 1]
- [128] K. Schlueter-Kuck and J. O. Dabiri. Pressure evolution in the shear layer of forming vortex rings. *Phys. Rev. Fluids*, 1(1):012501, May 2016. doi: 10.1103/PhysRevFluids.1.012501. [Cited on page 76]
- [129] D. H. Sharp. AN OVERVIEW OF RAYLEIGH-TAYLOR INSTABILITY. page 16. [Cited on page 37]
- [130] N. Shiraishi and M. Matsumoto. On classification of vortex-induced oscillation and its application for bridge structures. *Journal of Wind Engineering and Industrial Aerodynamics*, 14(1):419–430, Dec. 1983. ISSN 0167-6105. doi: 10.1016/0167-6105(83)90043-0. [Cited on page 77]
- [131] M. Shusser and M. Gharib. Energy and velocity of a forming vortex ring. *Physics of Fluids*, 12(3):618–621, Mar. 2000. ISSN 1070-6631, 1089-7666. doi: 10.1063/1.870268. [Cited on page 30]

- [132] M. Shusser, M. Gharib, M. Rosenfeld, and K. Mohseni. On the Effect of Pipe Boundary Layer Growth on the Formation of a Laminar Vortex Ring Generated by a Piston/Cylinder Arrangement. *Theoretical and Computational Fluid Dynamics*, 15(5):303–316, May 2002. ISSN 0935-4964, 1432-2250. doi: 10.1007/s001620100051. [Cited on page 96]
- [133] M. Shusser, M. Rosenfeld, J. O. Dabiri, and M. Gharib. Effect of time-dependent piston velocity program on vortex ring formation in a piston/cylinder arrangement. *Physics of Fluids*, 18(3):033601, Mar. 2006. ISSN 1070-6631, 1089-7666. doi: 10.1063/1.2188918. [Cited on pages 26, 33, and 97]
- [134] P. R. R. J. Stevens and H. Babinsky. Experiments to investigate lift production mechanisms on pitching flat plates. *Experiments in Fluids*, 58(1), Jan. 2017. ISSN 0723-4864, 1432-1114. doi: 10.1007/s00348-016-2290-x. [Cited on page 65]
- [135] G. K. Taylor, R. L. Nudds, and A. L. R. Thomas. Flying and swimming animals cruise at a Strouhal number tuned for high power efficiency. *Nature*, 425(6959): 707–711, Oct. 2003. ISSN 1476-4687. doi: 10.1038/nature02000. [Cited on page 32]
- [136] M. C. Thompson, T. Leweke, and K. Hourigan. Bluff Bodies and Wake–Wall Interactions. *Annual Review of Fluid Mechanics*, 53(1):347–376, 2021. doi: 10.1146/annurev-fluid-072220-123637. [Cited on page 41]
- [137] G. S. Triantafyllou, M. S. Triantafyllou, and M. A. Groenbaugh. Optimal Thrust Development in Oscillating Foils with Application to Fish Propulsion. *Journal of Fluids and Structures*, 7(2):205–224, Feb. 1993. ISSN 0889-9746. doi: 10.1006/jfls.1993.1012. [Cited on page 32]
- [138] Z. J. Wang, J. G. Liu, and S. Childress. Connection between corner vortices and shear layer instability in flow past an ellipse. *Physics of Fluids*, 11(9):2446–2448, Sept. 1999. ISSN 1070-6631, 1089-7666. doi: 10.1063/1.870108. [Cited on pages 34 and 36]
- [139] T. Wei and C. R. Smith. Secondary vortices in the wake of circular cylinders. *Journal of Fluid Mechanics*, 169(-1):513, Aug. 1986. ISSN 0022-1120, 1469-7645. doi: 10.1017/S0022112086000733. [Cited on pages 40, 77, 96, and 97]
- [140] C. Willert, B. Stasicki, J. Klinner, and S. Moessner. Pulsed operation of high-power light emitting diodes for imaging flow velocimetry. *Measurement Science and Technology*, 21(7):075402, July 2010. ISSN 0957-0233, 1361-6501. doi: 10.1088/0957-0233/21/7/075402. [Cited on pages 51, 79, and 99]
- [141] C. H. K. Williamson. Vortex Dynamics in the Cylinder Wake. *Annual Review of Fluid Mechanics*, 28(1):477–539, 1996. doi: 10.1146/annurev.fl.28.010196.002401. [Cited on page 77]

- [142] C. H. K. Williamson, T. Leweke, D. J. Asselin, and D. M. Harris. Phenomena, dynamics and instabilities of vortex pairs. *Fluid Dyn. Res.*, 46(6):061425, Nov. 2014. ISSN 1873-7005. doi: 10.1088/0169-5983/46/6/061425. [Cited on page 41]
- [143] C. J. Wojcik and J. H. J. Buchholz. Vorticity transport in the leading-edge vortex on a rotating blade. *Journal of Fluid Mechanics*, 743:249–261, Mar. 2014. ISSN 0022-1120, 1469-7645. doi: 10.1017/jfm.2014.18. [Cited on pages 39 and 96]
- [144] J. Wu, J. Sheridan, K. Hourigan, and J. Soria. Shear layer vortices and longitudinal vortices in the near wake of a circular cylinder. *Experimental Thermal and Fluid Science*, 12(2):169–174, Feb. 1996. ISSN 08941777. doi: 10.1016/0894-1777(95)00087-9. [Cited on page 77]
- [145] X. Xia and K. Mohseni. Lift evaluation of a two-dimensional pitching flat plate. *Physics of Fluids*, 25(9):091901, Sept. 2013. ISSN 1070-6631, 1089-7666. doi: 10.1063/1.4819878. [Cited on page 4]
- [146] L. Xu and M. Nitsche. Start-up vortex flow past an accelerated flat plate. *Physics of Fluids*, 27(3):033602, Mar. 2015. ISSN 1070-6631, 1089-7666. doi: 10.1063/1.4913981. [Cited on pages 24, 96, and 104]
- [147] J. Zhou, R. J. Adrian, S. Balachandar, and T. M. Kendall. Mechanisms for generating coherent packets of hairpin vortices in channel flow. *Journal of Fluid Mechanics*, 387:353–396, May 1999. ISSN 1469-7645, 0022-1120. doi: 10.1017/S002211209900467X. [Cited on pages 27, 58, 86, and 100]
- [148] Y. Zhou, R. J. R. Williams, P. Ramaprabhu, M. Groom, B. Thornber, A. Hillier, W. Mostert, B. Rollin, S. Balachandar, P. D. Powell, A. Mahalov, and N. Attal. Rayleigh–Taylor and Richtmyer–Meshkov instabilities: A journey through scales. *Physica D: Nonlinear Phenomena*, 423:132838, Sept. 2021. ISSN 0167-2789. doi: 10.1016/j.physd.2020.132838. [Cited on page 37]



Diego Franciscangeli

Ph.D student

Brief summary

I was born on the 6th of December 1992, in Jesi (Italy) and I fell in love with science quite early. This passion brought me to graduate in mechanical engineering and subsequently to start a Ph.D. in fluid dynamics. Now, my time as a Ph.D student is about to end and my will to apply what I've learnt leads me to look for a job position outside the academic world.



Languages

Italian

English

French

Advanced - C1

Intermediate - B1/B2



Soft skills

Communication

Teamwork

Project management

Research oriented

Adaptability

Willingness to learn

Ambition

Time management



Hard skills

Fluid and aerodynamics

Expert

Mechanical design

Advanced

Image processing

Advanced

Data analysis

Advanced



2018 - 2022

Work experiences

Ph.D CANDIDATE

École Polytechnique Fédérale de Lausanne



Experimental and theoretical study of vortices generated from the interaction of a solid body with an incoming flow. Thesis title: Growth, timing & trajectory of vortices behind a rotating plate.

2016

INTERNSHIP

Von Karman Institute for Fluid Dynamics



VON KARMAN INSTITUTE
FOR FLUID DYNAMICS

High speed photography and pressure measurements of a cavitating water flow downstream to an orifice. Internship duration: 6 months.

2014

INTERNSHIP

Department of Material sciences, UNIVPM



Development of a contactless optical technique that exploits laser light diffraction to measure the flow rate inside a microchannel. Internship duration: 4 months.



2014 - 2017

Past studies

UNIVERSITÀ POLITECNICA DELLE MARCHE - UNIVPM



Master science degree

Degree with honours in MECHANICAL ENGINEERING.

2011 - 2014

UNIVERSITÀ POLITECNICA DELLE MARCHE - UNIVPM



Batchelor science degree

Degree with honours in MECHANICAL ENGINEERING.

2006 - 2011

LICEO SCIENTIFICO LEONARDO DA VINCI, JESI (AN), ITALY



Diploma

Science oriented diploma with a final evaluation of 93/100.



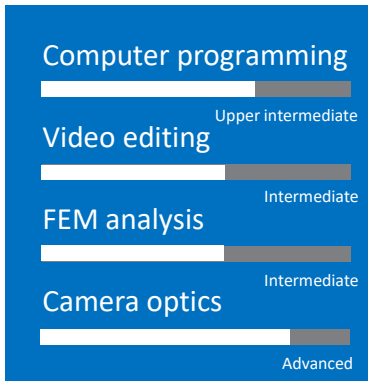
2021

Publications

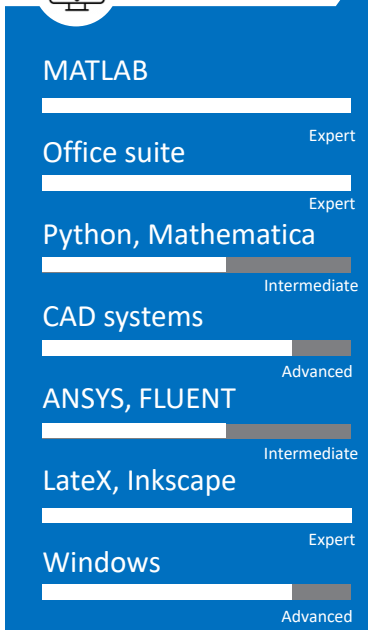
DISCRETE SHEDDING OF SECONDARY VORTICES ALONG A MODIFIED KADEN'S SPIRAL

D. Franciscangeli and K. Mulleners

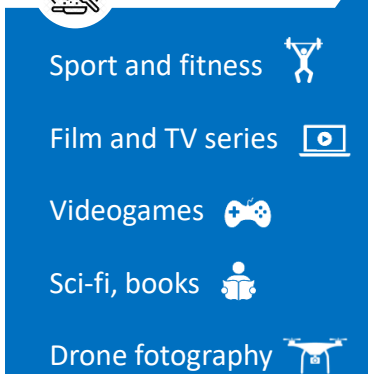
Journal of Fluid Mechanics, 917, ISSN 0022-1120, 1469-7645. doi: [10.1017/jfm.2021.259](https://doi.org/10.1017/jfm.2021.259).



Software skills



Hobbies



Contacts



+41 77 96 35 118
+39 393 63 20 985

diego.francescangeli@gmail.com
diego.francescangeli@epfl.ch

Grand-rue 8
Pully, CH-1009

2018

LAGRANGIAN ANALYSIS OF THE FORMATION OF VORTICES ON A ROTATING PLATE

D. Francescangeli, E. Reynaud, G. de Guyon-Crozier, K. Mulleners
[19th international symposium on the applications of laser and imaging techniques to fluid mechanics](#), Lisbon, Portugal, July 16-19

2016

OPTICAL MEASUREMENTS OF FLOW RATE IN A MICROFLUIDIC CHANNEL

D.E. Lucchetta, F. Vita, D. Francescangeli, O. Francescangeli, F. Simoni
Microfluidics and Nanofluidics, doi: [10.1007/s10404-015-1690-1](https://doi.org/10.1007/s10404-015-1690-1)



Conferences and summer schools

2021

APS DFD Phoenix

The 74th Annual Meeting of the Division of Fluid Dynamics, November 21-23rd.

2020

APS DFD Chicago

The 73rd Annual Meeting of the Division of Fluid Dynamics (virtual), November 22-24th.

2020

MODEL ORDER REDUCTION SUMMER SCHOOL École Polytechnique Fédérale de Lausanne

The focus of MORSS 2020 (virtual) was to give lectures, talks and informal discussions about model reduction methods, such as POD or reduced basis, that could be applied in a broad variety of nonlinear problems.

2019

APS DFD Seattle

The 72nd Annual Meeting of the Division of Fluid Dynamics (virtual), November 23-26th.

2019

COHERENT STRUCTURES IN UNSTEADY FLOWS: MATHEMATICAL AND COMPUTATIONAL METHODS

International centre for mechanical sciences, Udine

The scope of the summer school was to provide detection techniques and computational algorithms that help to identify Lagrangian and Eulerian coherent structures and coherent diffusion barriers in turbulent flows.

2018

LXLASER2018 Lisbon

The 19th International Symposium on Applications of Laser and Imaging Techniques to Fluid Mechanics, July 16-19th.



Additional information

2018

GRADUATION TO PROFESSIONAL ENGINEER Italian legislation

License as a mechanical and industrial engineer.

2011

DRIVING LICENSE: CATEGORY B